

THE INVESTIGATION OF ACCUMULATIVE ROLL BONDING
FOR PROCESSING TI/AL MULTILAYERED COMPOSITE
TARGETS FOR PERFORATION TESTING

by

DERRICK D. STOKES

VIOLA L. ACOFF, COMMITTEE CHAIR
PAUL G. ALLISON
MARK E. BARKEY
J. BRIAN JORDON
CHARLES A. MONROE
MARK L. WEAVER

A DISSERTATION

Submitted in partial fulfillment of the requirements
for the degree of Doctor of Philosophy
in the Department of Metallurgical and Materials Engineering
in the Graduate School of
The University of Alabama

TUSCALOOSA, ALABAMA

2015

Copyright Derrick Deshawn Stokes 2015
ALL RIGHTS RESERVED

ABSTRACT

Multilayered composites (MLCs) processed using accumulative roll bonding (ARB) have great potential as candidates for perforation testing. In the current study, multilayered composites comprised of alternating layers of titanium and aluminum have been investigated. Since the ARB process has been shown to induce anisotropy, the Ti/Al MLCs were first subjected to quasi-static loading to determine the effects of anisotropy. The MLCs were then subjected to perforation testing using projectiles with various apex angles. The effects of perforation testing were studied in terms of varying ballistic parameters and characterization of the fracture surfaces of the MLCs. The results of this study show that ARB-processed Ti/Al MLCs are promising for use in ballistic and impact applications.

DEDICATION

This dissertation is dedicated to three of the most influential people in my life: Derrick Stokes (Father), Sarah Stokes (Mother), and Mrs. JoAnne MaKinster (Dearest Friend). It's because of you that I am the person I am today. I truly appreciate the sacrifices you made for me, the wisdom you have given me, and the love you have shown me. I would not have made it this far without you. I will never forget the precious lessons that you have taught me over the years. I promise to continue to put forth my best effort in life and strive to be the best person that I can become. Thank you again for all you have done for me. I love you all dearly.

LIST OF ABBREVIATIONS AND SYMBOLS

<i>MLC</i>	Multilayered Composite
<i>PVD</i>	Physical Vapor Deposition
<i>ARB</i>	Accumulative Roll Bonding
<i>SPD</i>	Severe Plastic Deformation
<i>HCP</i>	Hexagonal Close Packed
<i>FCC</i>	Face Centered Cubic
<i>BCC</i>	Body Centered Cubic
<i>CVN</i>	Charpy V-notch
<i>DW</i>	Drop-Weight
<i>NDT</i>	Nil Ductility Transition
<i>SEM</i>	Scanning Electron Microscopy
<i>LOM</i>	Light Optical Microscopy
<i>EDM</i>	Electrical Discharge Machine
<i>HV</i>	Vickers Hardness
<i>HVN</i>	Vickers Hardness Number
<i>UTS</i>	Ultimate Tensile Strength
<i>HRC</i>	Rockwell C Hardness
<i>EDS</i>	Energy Dispersive Spectrometer
<i>BSE</i>	Back-scattered Electrons

SE	Secondary Electrons
RD	Rolling Direction
TD	Transverse Direction
BLE	Ballistic Limit Equations
Ti	Titanium
Al	Aluminum
δ_a	Original Stacking Thickness of Ti/Al MLC
δ_b	Final Stacking Thickness of Ti/Al MLC
σ_o	Flow Stress
σ_i	Intrinsic Strength
α	Crystal Structure-Based Constant
b	Burger's Vector
G	Modulus
ρ_G	Grain Density
E_K	Kinetic Energy
W_P	Work of Projectile
m_P	Mass of Projectile
V	Projectile Velocity
V_{oP}	Projectile Impact Velocity
V_{RP}	Projectile Residual Velocity
V_o	Impact Velocity
V_R	Residual Velocity
V_{50}	Ballistic Limit

$* V_{50}$	Estimated Ballistic Limit
R_t	Total Reduction
A	Semi-empirical Coefficient
m	Adjustment Factor
V_L	Velocity Limit
ρ_t	Target Density
ρ_P	Projectile Density
D_q	Projectile Diameter
D_P	Plug Diameter
h_o	Target Thickness
L_o	Original Length of Projectile

ACKNOWLEDGMENTS

First and foremost, I must give an acknowledgement to God for providing me with the strength that was needed to endure to the end of this doctoral journey (Philippians 4:13; Matthew 19:26). I must also recognize my strongest support systems and mentors: Dr. Jerrilyn D. Dixon, Dr. Gregory E. Williams, Dr. Greg Dillon, Dr. Wilbur L. Walters, Dr. Quinton L. Williams, Dr. Hilliard Lackey, Dr. Stacy Jones, and Mr. Bill Giles. It is because of your guidance, encouragement, and prayers that I was able to stay the course. I would also like to take this opportunity to thank a few of my close friends: Broderick K. Daniels, Lorenzo Gooch, Billy Richardson, Erin M. Jostes, Kerri L. Minter and Michael Grady. I truly appreciate the fun memories. The laughs we shared helped me maintain the balance I needed to finish this program. I would like to thank my family for their love, support, and prayers. Those gifts kept me uplifted.

I would like to extend a special thanks to my very good friend Todd M. Butler and Johnny Goodwin. You both have provided invaluable assistance and I am eternally grateful for all you have done for me. I must thank Dr. Stan Jones, Haley Scanlan, Sarah Chamberlain, Justin Burpo, and Chavis Cook for your assistance during my studies. Thank you Rich Martens and Rob Holler for your valued assistance with the Central Analytical Facility. I would like to thank my committee members for their thought provoking discussion and guidance. I must take this opportunity to acknowledge my lab mates: Dr. Peng Qu, Dr. Liming Zhou, Dr. Kai Tan, and Mr. Rashadd L. Coleman.

Lastly, I would like to thank my adviser Dr. Viola L. Acoff. Thank you for giving me an opportunity to pursue my dream. I truly appreciate all of your assistance throughout this process.

CONTENTS

ABSTRACT	ii
DEDICATION	iii
LIST OF ABBREVIATIONS AND SYMBOLS	iv
ACKNOWLEDGMENTS	vii
LIST OF TABLES	xii
LIST OF FIGURES	xiii
CHAPTER 1: INTRODUCTION	1
1.1 Multilayered Composites	1
1.2 MLC Processing Techniques	3
1.3 Accumulative Roll Bonding (ARB).....	3
1.4 Mechanical Testing Methods	5
1.4.1 Impact Tests	5
1.4.2 Quasi-static and Ballistic Tests	7
1.4.3 Shock Waves	9
1.5 References	10
CHAPTER 2: RESEARCH OBJECTIVES AND ORGANIZATION.....	15
2.1 Objectives	15
2.2 Dissertation Organization	15
2.3 References	17

CHAPTER 3: ARB-PROCESSED TI/AL MULTILAYERED COMPOSITES SUBJECTED TO QUASI-STATIC LOADING18

Abstract.....18

3.1 Introduction.....19

3.2 Experimental Procedure.....20

 3.2.1 Materials and Accumulative Roll Bonding (ARB).....20

 3.2.2 Microstructural Characterization22

 3.2.3 Mechanical Testing.....22

 3.2.4 ImageJ Analysis.....22

3.3 Results and Discussion24

 3.3.1 As-Roll Bonded Condition24

 3.3.2 Post-ARB Process.....24

 3.3.3 Quasi-Static Testing.....27

 3.3.4 Scanning Election Microscopy (SEM)31

 3.3.5 Structure-Property Relationship.....40

3.4 Conclusions.....42

3.5 References.....45

CHAPTER 4: THE EFFECTS OF VARYING BALLISTIC PARAMETERS ON THE OBSERVED FAILURE BEHAVIOR MODE IN ARB-PROCESSED TI/AL MULTILAYERED COMPOSITES.....47

Abstract.....47

4.1 Introduction.....48

4.2 Experimental Procedure.....50

 4.2.1 Sample Preparation50

 4.2.2 Accumulative Roll Bonding (ARB).....51

4.2.3 Impact Testing	51
4.2.4 Scanning Electron Microscopy (SEM)	54
4.3 Results and Discussion	56
4.3.1 Projectile Impact Velocity	56
4.3.2 Effect of Projectile Apex Angle.....	59
4.3.3 Dissipated Kinetic Energy Calculations	63
4.3.4 Composition Analysis of Fracture Surfaces	68
4.4 Conclusions.....	76
4.5 References.....	77
CHAPTER 5: THE EFFECTS OF VARYING BALLISTIC PARAMETERS ON THE BALLISTIC LIMIT OF TI/AL MULTILAYERED COMPOSITES	80
Abstract.....	80
5.1 Introduction.....	81
5.2 Experimental Procedure.....	84
5.2.1 Sample Preparation and Accumulative Roll Bonding	84
5.2.2 Impact Testing	85
5.3 Results and Discussion	85
5.3.1 Ballistic Limit Data.....	85
5.3.2 Ballistic Limit Comparison.....	95
5.4 Conclusions.....	97
5.5 References.....	98
CHAPTER 6: CONCLUSIONS AND FUTURE WORK.....	100
6.1 Major Conclusions	100

6.2 Recommendations for Future Work.....	101
6.3 References.....	103
APPENDIX A: Tensile Test Diagram	104
APPENDIX B: As-Rolled MLC Measurement	105
APPENDIX C: Measurement of Titanium Layers in ARB-Processed MLC	106
APPENDIX D: Measurement of Aluminum Layers in ARB-Processed MLC	107

LIST OF TABLES

3.1 Ultimate Tensile Strength of ARB-Processed Ti/Al MLCs Determined Using Quasi-Static Loading	28
4.1 Projectile Apex Angle vs. Dimple Rupture Deformation for Ti/Al MLC Targets	66
4.2 Measured Layer Thickness, Total Reduction and Plastic Strain for Ti/Al MLC Specimens Subjected to 4 ARB Cycles. This Table was Adapted from Work From Zhang [38].....	75
5.1 Data Used to Calculate the Estimated Ballistic Limits for the 2.54cm x 2.54cm Targets.....	89
5.2 Data Used to Calculate the Estimated Ballistic Limits for the 3.20cm x 3.20cm Targets.....	90
5.3 Estimated Ballistic Limits vs. Apex Angle data for 2.54cm x 2.54cm ARB-processed Ti/Al MLCs Targets	92
5.4 Estimated Ballistic Limits vs. Apex Angle data for 3.20cm x 3.20cm ARB-processed Ti/Al MLCs Targets	92

LIST OF FIGURES

1.1 Schematic a General MLC.....	2
1.2 Schematic of the ARB Process	6
3.1 Schematic of the Stacking Process	21
3.2 Schematic of the ARB Process	21
3.3 Schematic Depicting Tensile Specimen Orientation During Machining Process	23
3.4 Schematic of Tensile Specimen Dimensions.....	23
3.5 Light Micrograph of a Ti/Al MLC in As Roll Bonded Condition.....	25
3.6 Micrographs of Ti/Al MLC after 4 ARB Cycles (A) SEM Secondary Electron Image (B) Light Micrograph Image	26
3.7 Average Engineering Stress vs. Average Engineering Strain Plot of Specimens Tested in the Transverse Direction (TD)	29
3.8 Average Engineering Stress vs. Average Engineering Strain Plot of Specimens Tested in the Rolling Direction (RD)	29
3.9 Average Engineering Stress vs. Average Engineering Strain Plot That Compares Strength as a Function of Processing Direction.....	30
3.10 SEM Micrograph of Fractured Specimen Made From ARB-Processed Ti/Al MLC. Specimen was Loaded Parallel to the Rolling Direction (Sample ID: Q-RD-2)	32
3.11 (A) Higher Magnification of Boxed Region “a” in Fig. 3.10. (B) Higher Magnification of Boxed Area in (A)	33
3.12 (A) Higher Magnification of Boxed Region “b” in Fig. 3.10. (B) Higher Magnification of Boxed Area in (A)	34

3.13 (A) Higher Magnification of Boxed Region “c” in Fig. 3.10. (B) Higher Magnification of Boxed Area in (A)	35
3.14 SEM Micrograph of Fractured Specimen Made From ARB-Processed Ti/Al MLC. Specimen was Loaded Perpendicular to the Rolling Direction (Sample ID: T-TD-2).....	36
3.15 (A) Higher Magnification of Boxed Region “a” in Fig. 3.14. (B) Higher Magnification of Boxed Area in (A)	37
3.16 (A) Higher Magnification of Boxed Region “b” in Fig. 3.14. (B) Higher Magnification of Boxed Area in (A)	38
3.17 (A) Higher Magnification of Boxed Region “c” in Fig. 3.14. (B) Higher Magnification of Boxed Area in (A)	39
3.18 Light Micrograph Images of Ti/Al MLC Tensile Specimens Subjected to Quasi-Static Loading: Sample Q-3. (A) Rolling Direction (B) Transverse Direction.....	41
3.19 Compositional Map of Fractured Tensile Specimen: Sample R-1. Green Depicts Ti whereas the Red Depicts Al (A) Rolling Direction (B) Transverse Direction.....	43
4.1 A Schematic of the ARB Stacking Sequence and Processing Technique.....	52
4.2 Test Projectiles with Varying Nose Geometries: (A) 30° (B) 60° (C) 90° (D) 180°	53
4.3 Ballistic Apparatus.....	55
4.4 Representative of ARB-Processed Ti/Al MLC Targets Subjected to Perforation Testing. (A) Sample E2: Perforated at 95m/s by a 30° Projectile (B) Sample I3: Perforated at 213m/s by a 90° Projectile.....	57
4.5 2.54cm x 2.54cm MLC (Sample L3) Subjected to Perforation by a 60° Projectile at 121m/s.....	58
4.6 2.54cm x 2.54cm MLC (Sample L2) Subjected to Perforation by a 60° Projectile at 231m/s.....	58
4.7 3.20cm x 3.20cm MLC (Sample F1) Subjected to Perforation by a 30° Projectile at 129m/s.....	61

4.8 2.54cm x 2.54cm MLC (Sample L3) Subjected to Perforation by a 60° Projectile at 121m/s.....	61
4.9 3.20cm x 3.20cm MLC (Sample E1) Subjected to Perforation by a 90° Projectile at 121m/s.....	62
4.10 2.54cm x 2.54cm MLC (Sample M1) Subjected to Perforation by a 180° Projectile at 125m/s.....	62
4.11 ImageJ Analysis of 3.20cm x 3.20cm MLC (Sample F1) Subjected to Perforation by a 30° Projectile at 129m/s.....	64
4.12 ImageJ Analysis of 2.54cm x 2.54cm MLC (Sample L3) Subjected to Perforation by a 60° Projectile at 121m/s.....	64
4.13 ImageJ Analysis of 3.20cm x 3.20cm MLC (Sample E1) Subjected to Perforation by a 90° Projectile at 121m/s.....	65
4.14 ImageJ Analysis of 2.54cm x 2.54cm MLC (Sample M1) Subjected to Perforation by a 180° Projectile at 125m/s.....	65
4.15 Dimple Rupture vs. Apex Angle Graph of Table 4.1	66
4.16 3.20cm x 3.20cm MLC (Sample F1) Subjected to Perforation by a 30° Projectile at 129m/s.....	67
4.17 Higher Magnification of Region Denoted by Boxed Region in Fig. 4.16	67
4.18 SEM Secondary Electron Image of 2.54cm x 2.54cm Target Perforated by a 30° Projectile at an Impact Velocity of 227m/s.....	69
4.19 SEM EDS Profile for Region Shown in Fig. 4.18	69
4.20 Higher Magnification of Image Shown in Fig. 4.18 (A) Secondary Electron Image; (B) Back-scattered Electron Image.....	70
4.21 Region Showing Where Compositional Mapping was Performed....	71
4.22 Compositional Map of Region Shown in Fig. 4.21. The Green Depicts Titanium whereas the Red Depicts Aluminum.....	71
4.23 SEM Micrograph of the Spall Surface in a Ti6Al4V Specimen that was Exposed to Perforation Testing. This image was Taken From Grebe et al.	72

4.24 SEM Micrograph of AA6016-T4 Aluminum Specimen that was Exposed to Tensile Testing. This image was Taken From Thuillier et al.....	73
5.1 2.54cm x 2.54cm MLC (Sample M1) Subjected to Perforation by a 180° Projectile at 125m/s.....	86
5.2 3.20cm x 3.20cm MLC (Sample G1) Subjected to Perforation by a 180° Projectile at 185m/s.....	86
5.3 2.54cm x 2.54cm MLC (Sample M2) Subjected to Perforation by a 30° Projectile at 227m/s.....	87
5.4 3.20cm x 3.20cm MLC (Sample J1) Subjected to Perforation by a 30° Projectile at 181m/s.....	87
5.5 Velocity vs. Projectile Apex Angle Chart for 2.54cm x 2.54cm Ti/Al ARB-Processed Targets	89
5.6 Velocity vs. Projectile Apex Angle Chart for 3.20cm x 3.20cm Ti/Al ARB-Processed Targets	90

CHAPTER 1

INTRODUCTION

1.1 Multilayered Composites

Multilayered Composites (MLCs) are structures that are made up of several alternating materials as shown in Figure 1.1. MLCs offer many structural benefits because they are often made of lightweight materials which have low densities and high strengths [1]. The lightweight design of MLCs are extremely beneficial in a number of engineering applications because weight is often a critical topic to consider in composite materials [2]. Due to the weight/strength benefits, MLCs have shown particular promise in military applications, especially within the areas of armor development and ballistics [3,4]. Various military branches have shown interest in the potential usages of MLCs. In fact, the US Army has expressed a desire to test the ballistic limit of MLCs on a laboratory based scale [5].

In the current study, perforation testing is used to investigate the ballistic limit tendencies of MLCs composed of Titanium (Ti) and Aluminum (Al) that were processed using Accumulative Roll Bonding (ARB). According to literature, Ti and Al are prime candidates for MLC development because composites that contain alternating layers of hard and soft materials possess the ability to hinder projectile perforation [6,7]. This is because the soft materials tend to deform plastically to absorb projectile driven shock waves while the hard materials impede crack propagation [8,9].

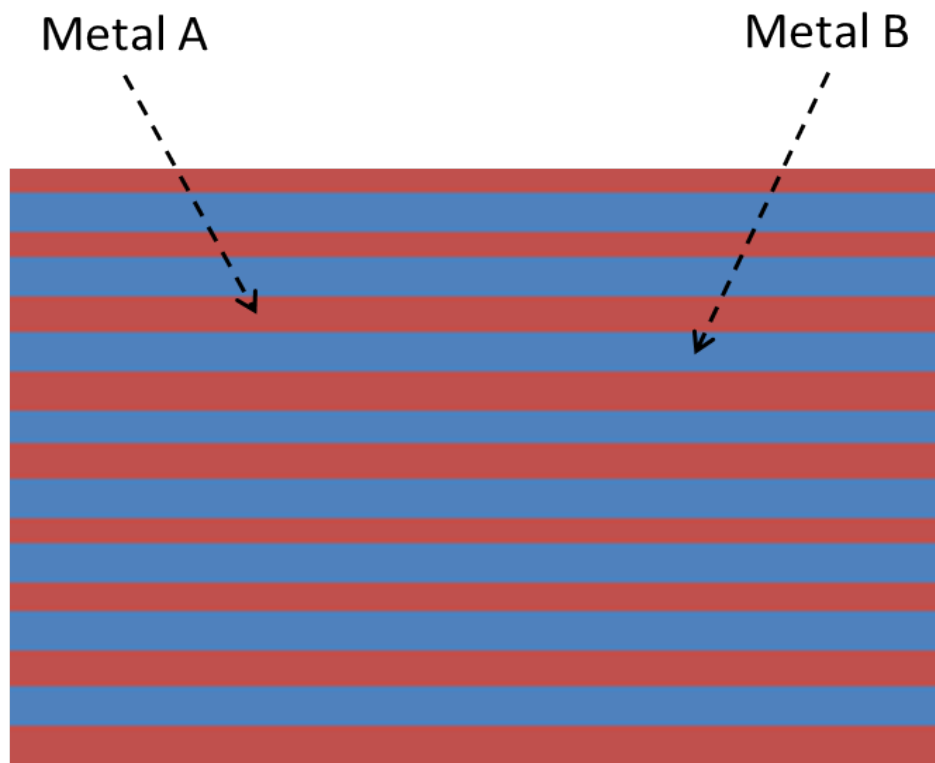


Fig 1.1: Schematic of a General MLC

In an attempt to observe any ballistic parameter/ballistic limit correlations, a tailored perforation regimen has been designed by The University of Alabama researchers [5]. This testing method was used to investigate the ballistic resistance of specialized MLCs. The Ti/Al MLCs, in this study were manufactured via ARB. This manufacturing method was chosen based on prior work by Acoff et al. who have successfully manufactured Ti/Al MLCs using ARB [10-15].

1.2 MLC Processing Techniques

There are a variety of processing methods that can be used to produce MLCs. This includes: hot rolling, explosive forming, and physical vapor deposition (PVD) [16-22]. The aforementioned processing techniques usually involve high temperatures, sophisticated furnaces, and intricate processing steps which can be costly. The ARB process provides a more simplistic approach to produce MLCs. Lou and Acoff have successfully produced Titanium-based MLCs via the ARB processing technique [15].

1.3 Accumulative Roll Bonding (ARB)

Accumulative Roll Bonding is a severe plastic deformation (SPD) processing technique that was developed by Saito et al. in 1998. This process employs the use of a rolling mill to induce ultra-high plastic strains into a material [23]. As strain is added, the dislocation density increases within the metal resulting in significant strain hardening [24]. As a result, SPD techniques, such as ARB, are useful ultra-high straining techniques for producing composites such as MLCs [24-26].

Strain hardening is a mechanism/ method which is used for hardening metals and alloys. Strain hardening is often used as a hardening technique for metals that do not respond well to heat

treatment [27]. Most crystalline materials, e.g. metals, become more resistant to deformation as added stress is applied [28]. This process of increasing strength with increasing deformation is called strain hardening. Strain hardening is a very important variable in cold working (i.e. deforming a material below the recrystallization temperature) [29]. The impact of strain hardening is described by the following flow stress equation:

$$\sigma_o = \sigma_i + \alpha G_B b \rho_G^{\frac{1}{2}} \quad (1.1)$$

where σ_o is the flow stress, σ_i is the intrinsic strength, α is a crystal structure-based constant, G_B is the bulk modulus, b is the Burger's Vector, ρ_G is the dislocation density of a given crystal.

In metals, the degree or rate of strain hardening is influenced by crystalline structure. For example, the rate of strain hardening is lower for a hexagonal close packed (HCP) metal than in the case of face centered cubic (FCC) and body centered cubic (BCC) metals. Therefore, Aluminum (a FCC metal) is expected to have a higher strain hardening rate than Titanium (an HCP metal). This is partially due to the difference in active slip systems. As strain hardening rates increase, intersecting dislocations can cause an obstruction and result in an increase in metal strength. This dislocation obstruction can be due to either: 1) an intersection of dislocation stress fields, 2) dislocation interactions which can produce sessile locks, as well as 3) the intermingling of multiple slip systems (which can produce dislocation jogs) [27].

In ARB, the percentage of deformation is directly related to the thickness of the sample as well as the spacing of the rolling pins. As the specimen thickness is reduced, there is a subsequent increase in grain elongation. According to Saito et al., the ARB technique was designed to be easily transferable into industry [23]. Since the transference into industry, the ARB process has become an effective technique for processing bulk materials [23].

A schematic of the ARB process is shown in Figure 1.2. In the ARB process multiple sheets of metal are stacked on top of one another. Once they are properly arranged, the metals are then fed through a rolling mill to form a single continuous component. After rolling, the sample is sectioned into halves, prepped with a retreated surface, restacked, and fed through the rolling mill again. This procedure is repeated until the desired number of ARB cycles is reached. With each cycle, both hardness and strength increase while ductility decreases. Furthermore, if reduction is kept at 50%, after each ARB cycle the final thickness of the manufactured component will be the same as the starting thickness before the first ARB cycle [23].

1.4 Mechanical Testing Methods

A variety of testing methods are often used to determine the mechanical properties of MLCs. This includes variations of Charpy impact tests, drop-weight impact tests, quasi-static tension and compression tests, and ballistic (or high velocity impact) tests [28]. An overview of the major testing methods are summarized in this section.

1.4.1 Impact Tests

Charpy impact testing, commonly referred to as Charpy V-notch (CVN) testing, was invented by S. B. Russell and G. Charpy in 1901 [30]. This impact testing technique utilizes a pendulum to apply impact force. The pendulum, released from a known height, strikes the specimen and propagates a crack. The combination of pendulum height and crack propagation can be used to describe material durability [30]. CVN testing can be an essential testing method in the areas of failure analysis and fractology because it provides insight into the fracture resistance of a given material. In comparison to other impact testing methods, CVN testing is a beneficial method because it is fairly easy to implement and relatively inexpensive [31].

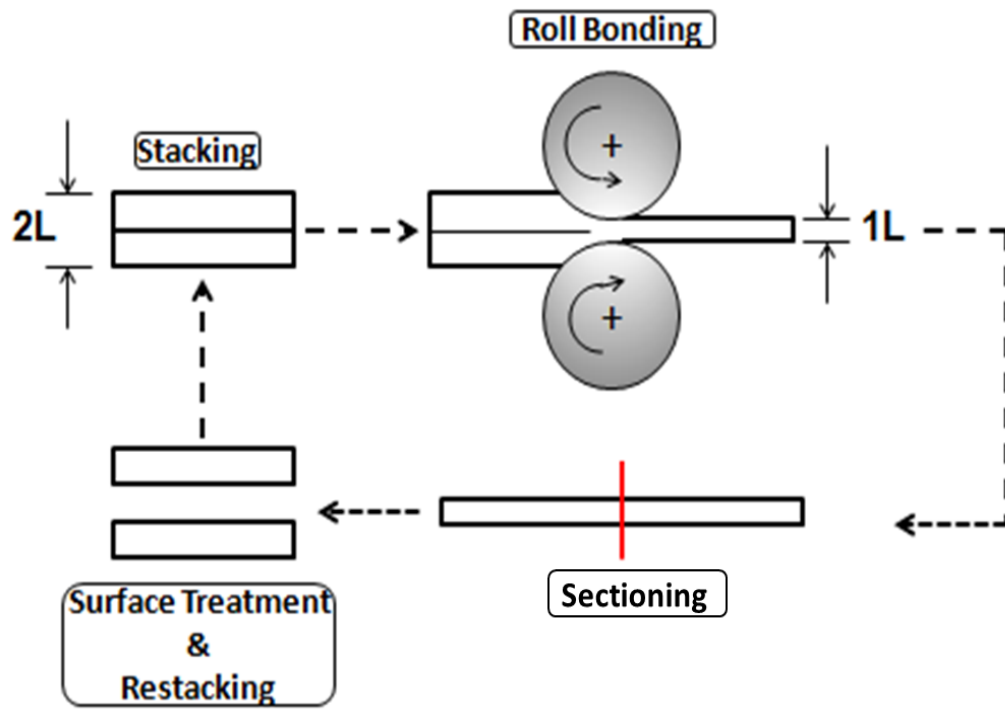


Fig. 1.2: Schematic of the ARB Process

Another valuable impact testing method is called the Drop-Weight (DW) test. In this test, a free falling weight (of known height and mass) is dropped and the associated data is used to determine the reducibility of a material (commonly steels). The DW test is similar to the CVN test because it can be used to determine the amount of energy absorbed within a material. This is done by using the corresponding height/weight data to calculate impact energy. The response of a given material to impact energy determines the durability or fracture toughness of the material. An issue with DW tests is that they are often judged on a pass/fail scale. This is because the weight either fails to cause deformation (pass) or destroys the sample (fail) [32]. This method, albeit convenient, may not be as sophisticated as certain applications may require. Both the CVN and DW tests are conducted at varying temperatures to determine the ductile-to-brittle transition temperature of a material. The difference between the two testing methods is the corresponding transition temperature sensitivities. The DW tests the nil ductility transition (NDT) temperature, which is more precise than the CVN transition temperature. The added sensitivity of the DW NDT temperature makes the drop-weight test more reliable than the CVN test [28].

1.4.2 Quasi-static and Ballistic Tests

In recent years, a combination of quasi-static and ballistic testing methods have been developed. This was done as an attempt to advance the knowledge regarding the mechanical behavior of impact resistant materials [2,33-57]. These tests involve varying strain rates and high impact velocities. Quasi-static loading is held within a low range of strain rates to avoid the influences of shock waves [58]. In high rate tests, such as ballistic testing, shock waves propagate through the material and can have a significant influence on the failure behavior of the test specimen [59].

Quasi-Static tension and compression testing can be used for establishing baseline information regarding the intrinsic mechanical properties of a material. The testing range for this specific loading method is typically within 10^{-5}s^{-1} and 10^{-1}s^{-1} . For ideal conditions, metallic-based materials are traditionally performed at a strain rate of 10^{-3}s^{-1} . This strain rate is critical because it eliminates the presence of influential inertia and wave propagation effects within the test specimen [58]. Due to the limited strain range, this test is insufficient for determining how a material will react under high rate conditions.

Ballistics describes the science of projectiles in flight. Ballistics is generally broken down into four categories: 1) internal ballistics, 2) intermediate ballistics, 3) exterior ballistics, and 4) terminal ballistics. Internal ballistics is the study of projectiles that still are housed within a firearm. Intermediate ballistics describe projectiles as they exit the gun muzzle. Exterior ballistics is a study that analyzes projectiles in flight. Lastly, terminal ballistics is focused on the penetration behavior of ballistics into a dense object [60]. In the current study, the ballistic category of focus will be terminal ballistics.

Mechanically strengthened MLCs have been a topic of interest within the defense industry. So far, MLCs have become incorporated into armored vehicles and even military grade helmets [8,48,61]. To help ensure safety and survivability rates, the requirements for military grade MLCs are very high [62]. The complexities associated with military grade protective gear often calls for an advanced, often complex, ballistics testing regimen. Typical ballistic testing systems may use pressurized chambers or gunpowder to propel projectiles. Once the projectile is in flight, it typically travels through velocity detectors to measure impact and residual velocities. It is then possible to determine the amount of energy lost during perforation by measuring the

differences in impact and residual velocities [8]. By utilizing the impact and residual velocity data, an estimated ballistic limit ($*V_{50}$) can be determined.

Ballistic limit is a statistical value that is determined through striking, or impact, velocities. By definition, ballistic limit (V_{50}) is the impact velocity (V_o) at which there exists a 50% probability of failure to a given target material [63]. Due to military requirements, strict military specification (MIL-A-46100) must be used to accurately determine a material's ballistic limit. According to the military specification MIL-A-46100, there are specific target thickness requirements as projectile caliber is varied [64]. When operating outside of the strict military guideline, it is important to note that an estimated ballistic limit ($*V_{50}$) is obtained and not the government issued ballistic limit (V_{50}).

1.4.3 Shock Waves

Shock waves are unique phenomena that play a vital role in high velocity (e.g. ballistic) testing. Waves are generated as objects, e.g. projectiles, are propelled through a given medium (such as air). As those waves travel faster than the speed of sound, shock waves are formed. Upon impact, shock waves rapidly travel to the boundary of a target (or until impact energy is absorbed). According to Diedrich and Stepka, if the traveling shock (or stress) wave is able to rebound from a boundary, the wave will often rebound with amplified tensile forces. Therefore, it can be conceptually understood that the strength of shockwaves is strongly dependent upon distance from impact [35].

1.5 References

- [1] A. Patselov, B. Greenberg, S. Gladkovskii, R. Lavrikov and E. Borodin, "Layered Metal-intermetallic Composites in Ti-Al System: Strength Under Static and Dynamic Load," *AASRI Procedia* 3 (2012) 107-112.
- [2] P. K. Jena, K. Ramanjeneyulu, K. Siva Kumar and T. Balakrishna Bhat, "Ballistic studies on layered structures," *Materials & Design* 30 (2009) 1922-1929.
- [3] E. S. C. Chin, "Army focused research team on functionally graded armor composites," *Materials Science and Engineering: A* 259 (1999) 155-161.
- [4] H. L. Gower, D. S. Cronin and A. Plumtree, "Ballistic impact response of laminated composite panels," *International Journal of Impact Engineering* 35 (2008) 1000-1008.
- [5] J. M. Conway, A. R. Ortiz, S. E. Jones, V. L. Acoff and X. Bu, Perforation Testing of a Titanium Alloy Target Using Hardened 4340 Steel Projectiles, in "Pressure Vessels & Piping Division" (ASME, Bellevue, WA, 2010) p. 1-6.
- [6] K. S. Kumar and M. S. DiPietro, "Ballistic penetration response of intermetallic matrix composites," *Scripta Metallurgica et Materialia* 32 (1995) 793-798.
- [7] A. Rohatgi, D. J. Harach, K. S. Vecchio and K. P. Harvey, "Resistance-curve and fracture behavior of Ti-Al₃Ti metallic-intermetallic laminate (MIL) composites," *Acta Materialia* 51 (2003) 2933-2957.
- [8] G. Balaganesan, R. Velmurugan, M. Srinivasan, N. K. Gupta and K. Kanny, "Energy absorption and ballistic limit of nanocomposite laminates subjected to impact loading," *International Journal of Impact Engineering* 74 (2014) 57-66.
- [9] E. K. Öberg, J. Dean and T. W. Clyne, "Effect of Inter-layer Toughness in Ballistic Protection Systems on Absorption of Projectile Energy," *International Journal of Impact Engineering* (2014).
- [10] G. P. Chaudhari and V. Acoff, "Cold roll bonding of multi-layered bi-metal laminate composites," *Composites Science and Technology* 69 (2009) 1667-1675.
- [11] J.-G. Luo and V. L. Acoff, "Processing gamma-based TiAl sheet materials by cyclic cold roll bonding and annealing of elemental titanium and aluminum foils," *Materials Science and Engineering: A* 433 (2006) 334-342.
- [12] R. Zhang and V. L. Acoff, "Processing sheet materials by accumulative roll bonding and reaction annealing from Ti/Al/Nb elemental foils," *Materials Science and Engineering: A* 463 (2007) 67-73.

- [13] G. P. Chaudhari, K. Serin and V. L. Acoff, "Processing Ultrafine Grained Composites of Elemental Titanium and Aluminium by Severe Plastic Deformation," in *Ultrafine Grained Materials III*, edited by Y. T. Zhu, T. G. Langdon, R. Z. Valiev, S. L. Semiatin, D. H. Shin and T. C. Lowe (TMS, 2004).
- [14] G. P. Chaudhari and V. L. Acoff, "Titanium aluminide sheets made using roll bonding and reaction annealing," *Intermetallics* 18 (2010) 472-478.
- [15] J.-G. Luo and V. L. Acoff, "Using cold roll bonding and annealing to process Ti/Al multi-layered composites from elemental foils," *Materials Science and Engineering: A* 379 (2004) 164-172.
- [16] P. V. Vaidyanathan and A. R. Ramanathan, "Design for quality explosive welding," *Journal of Materials Processing Technology* 32 (1992) 439-448.
- [17] F. Grignon, D. Benson, K. S. Vecchio and M. A. Meyers, "Explosive welding of aluminum to aluminum: analysis, computations and experiments," *International Journal of Impact Engineering* 30 (2004) 1333-1351.
- [18] K. S. Kumar and G. Bao, "Intermetallic-matrix composites: An overview," *Composites Science and Technology* 52 (1994) 127-150.
- [19] M. Acarer, B. Gülenç and F. Findik, "Investigation of explosive welding parameters and their effects on microhardness and shear strength," *Materials & Design* 24 (2003) 659-664.
- [20] N. Kahraman, B. Gülenç and F. Findik, "Joining of titanium/stainless steel by explosive welding and effect on interface," *Journal of Materials Processing Technology* 169 (2005) 127-133.
- [21] F. Findik, "Recent developments in explosive welding," *Materials & Design* 32 (2011) 1081-1093.
- [22] I. A. Bataev, A. A. Bataev, V. I. Mali and D. V. Pavliukova, "Structural and mechanical properties of metallic–intermetallic laminate composites produced by explosive welding and annealing," *Materials & Design* 35 (2012) 225-234.
- [23] Y. Saito, H. Utsunomiya, N. Tsuji and T. Sakai, "Novel ultra-high straining process for bulk materials—development of the accumulative roll-bonding (ARB) process," *Acta Materialia* 47 (1999) 579-583.
- [24] T. Hausöl, V. Maier, C. W. Schmidt, M. Winkler, H. W. Höppel and M. Göken, "Tailoring Materials Properties by Accumulative Roll Bonding," *Advanced Engineering Materials* 12 (2010) 740-746.

- [25] N. Tsuji, Y. Ito, Y. Saito and Y. Minamino, "Strength and ductility of ultrafine grained aluminum and iron produced by ARB and annealing," *Scripta Materialia* 47 (2002) 893-899.
- [26] N. Tsuji, Y. Saito, S. H. Lee and Y. Minamino, "ARB (Accumulative Roll-Bonding) and other new Techniques to Produce Bulk Ultrafine Grained Materials," *Advanced Engineering Materials* 5 (2003) 338-344.
- [27] G. E. Dieter, Mechanical Metallurgy, (New York : McGraw-Hill, c1986. 3rd ed., 1986).
- [28] M. Meyers and K. Chawla, Mechanical Behavior of Materials, 2nd edition (Cambridge University Press, New York, 2009).
- [29] J. F. Shackelford, Introduction to Materials Science for Engineers 5th edition (Prentice-Hall, Inc., New York, 2000).
- [30] L. Tóth, H. P. Rossmanith and T. A. Siewert, "Historical background and development of the Charpy test," in "European Structural Integrity Society", edited by D. François and A. Pineau (Elsevier, 2002) p. 3-19.
- [31] B. N. Rao and A. R. Acharya, "Charpy V-notch impact test: A partial alternate to ASTM E 399 fracture testing for routine quality control applications," *Engineering Fracture Mechanics* 32 (1989) 39-42.
- [32] P. Zoller, "Instrumentation for impact testing of plastics," *Polymer Testing* 3 (1983) 197-208.
- [33] B. Babaei, M. M. Shokrieh and K. Daneshjou, "The ballistic resistance of multi-layered targets impacted by rigid projectiles," *Materials Science and Engineering: A* 530 (2011) 208-217.
- [34] G. Ben-Dor, A. Dubinsky and T. Elperin, "On the order of plates providing the maximum ballistic limit velocity of a layered armor," *International Journal of Impact Engineering* 22 (1999) 741-755.
- [35] J. H. Diedrich and F. S. Stepka, "Investigation of Damage to Brittle Materials by Impact with High-Velocity Projectiles Into Glass and Lucite," NASA, United States (1965).
- [36] H. A. Grebe, H.-R. Pak and M. Meyers, "Adiabatic shear localization in titanium and Ti-6 pct Al-4 pct V alloy," *Metallurgical Transactions A* 16 (1985) 761-775.
- [37] J. C. Huang, Y.-S. Lo and G. T. Gray III, "The response of metal-matrix composites subjected to quasi-static and shock-wave deformation," *Materials Chemistry and Physics* 35 (1993) 71-85.

- [38] F. Jiang, R. M. Kulin and K. S. Vecchio, "Use of Brazilian Disk Test to Determine Properties of Metallic-Intermetallic Laminate Composites," *JOM* 62 (2010).
- [39] G. H. Jonas and J. A. Zukas, "Mechanics of penetration: Analysis and experiment," *International Journal of Engineering Science* 16 (1978) 879-903.
- [40] H. N. Krishna Teja Palleti, S. Gurusamy, S. Kumar, R. Soni, B. John, R. Vaidya, A. Bhoge and N. K. Naik, "Ballistic impact performance of metallic targets," *Materials & Design* 39 (2012) 253-263.
- [41] S. Leppin and R. L. Woodward, "Perforation mechanisms in thin titanium alloy targets," *International Journal of Impact Engineering* 4 (1986) 107-115.
- [42] P. Qiao, M. Yang and F. Bobaru, "Impact Mechanics and High-Energy Absorbing Materials: Review," *Journal of Aerospace Engineering* 21 (2008) 235-248.
- [43] Shaktivesh, N. S. Nair, C. V. Sessa Kumar and N. K. Naik, "Ballistic impact performance of composite targets," *Materials & Design* 51 (2013) 833-846.
- [44] A. H. Sheikh, P. H. Bull and J. A. Kepler, "Behaviour of multiple composite plates subjected to ballistic impact," *Composites Science and Technology* 69 (2009) 704-710.
- [45] M. R. Staker, "The relation between adiabatic shear instability strain and material properties," *Acta Metallurgica* 29 (1981) 683-689.
- [46] X. Teng and T. Wierzbicki, "Numerical study on crack propagation in high velocity perforation," *Computers & Structures* 83 (2005) 989-1004.
- [47] X. Teng, T. Wierzbicki and M. Huang, "Ballistic resistance of double-layered armor plates," *International Journal of Impact Engineering* 35 (2008) 870-884.
- [48] C. Y. Tham, V. B. C. Tan and H. P. Lee, "Ballistic impact of a KEVLAR® helmet: Experiment and simulations," *International Journal of Impact Engineering* 35 (2008) 304-318.
- [49] M. Übeyli, R. O. Yıldırım and B. Ögel, "On the comparison of the ballistic performance of steel and laminated composite armors," *Materials & Design* 28 (2007) 1257-1262.
- [50] T. Wierzbicki, "Petalling of plates under explosive and impact loading," *International Journal of Impact Engineering* 22 (1999) 935-954.
- [51] T. Wierzbicki and G. N. Nurick, "Large deformation of thin plates under localised impulsive loading," *International Journal of Impact Engineering* 18 (1996) 899-918.
- [52] M. L. Wilkins, "Mechanics of penetration and perforation," *International Journal of Engineering Science* 16 (1978) 793-807.

- [53] R. L. Woodward, "The penetration of metal targets which fail by adiabatic shear plugging," *International Journal of Mechanical Sciences* 20 (1978) 599-607.
- [54] R. L. Woodward, "The penetration of metal targets by conical projectiles," *International Journal of Mechanical Sciences* 20 (1978) 349-359.
- [55] R. L. Woodward, "The interrelation of failure modes observed in the penetration of metallic targets," *International Journal of Impact Engineering* 2 (1984) 121-129.
- [56] R. L. Woodward and S. J. Cimpoeru, "A study of the perforation of aluminium laminate targets," *International Journal of Impact Engineering* 21 (1998) 117-131.
- [57] R. L. Woodward and M. E. de Morton, "Penetration of targets by flat-ended projectiles," *International Journal of Mechanical Sciences* 18 (1976) 119-127.
- [58] Testing Machines and Strain Sensors, in "ASM Handbook" (ASM International, Materials Park, OH, 2000).
- [59] H. Huh, W. J. Kang and S. S. Han, "A tension split Hopkinson bar for investigating the dynamic behavior of sheet metals," *Experimental Mechanics* 42 (2002) 8-17.
- [60] N. Maiden, "Historical overview of wound ballistics research," *Forensic Science, Medicine, and Pathology* 5 (2009) 85-89.
- [61] S. G. Kulkarni, X. L. Gao, S. E. Horner, J. Q. Zheng and N. V. David, "Ballistic helmets – Their design, materials, and performance against traumatic brain injury," *Composite Structures* 101 (2013) 313-331.
- [62] J. E. Gorfain and C. T. Key, "Damage prediction of rib-stiffened composite structures subjected to ballistic impact," *International Journal of Impact Engineering* 57 (2013) 159-172.
- [63] J. Misesy, "Analysis of Ballistic Limit", (Memorandum Report ARBRL-MR-02815, Army Ballistic Research Lab Aberdeen Proving Ground, MD, 1978).
- [64] R. C. Grubinskas, A Review of the V50 Ballistic Limit Requirements of MIL-A-46100, U.S. Army Research Laboratory Watertown, MA, 1993).

CHAPTER 2

RESEARCH OBJECTIVES AND ORGANIZATION

2.1 Objectives

Accumulative roll bonding (ARB) has been shown as a promising technique for processing multilayered composites comprised of titanium and aluminum [1]. However, there is very little published work on perforation testing of MLCs processed using the ARB process [2]. Before MLC targets processed using the ARB technique can be considered as a viable method for impact testing, these targets must be investigated prior to and after subjecting to perforation testing. Therefore, the overall objectives of this study are to:

- 1) To study the anisotropic behavior of ARB-processed Ti/Al MLCs as a function of rolling direction.
- 2) To investigate the relationship between ballistic parameters and failure mode of ARB-processed Ti/Al MLCs.
- 3) To determine the relationship that exists between ballistic parameters and estimated ballistic limit.

2.2 Dissertation Organization

This document is an article-based dissertation. In Chapter 3, ARB-processed Ti/Al MLCs are subjected to quasi-static loading and material strength as a function of processing directionality is discussed.

In Chapter 4, the influence of varying ballistic parameters on the failure behavior of ARB-processed Ti/Al MLCs is investigated. In this chapter, failure mode is observed as variations in ballistic parameters (such as impact velocity, projectile apex angle, target size, etc.) occur.

Chapter 5 is devoted to understanding how the ballistic limit of ARB-processed Ti/Al MLCs is influenced by varying ballistic parameters.

2.3 References

- [1] J.-G. Luo and V. L. Acoff, "Processing gamma-based TiAl sheet materials by cyclic cold roll bonding and annealing of elemental titanium and aluminum foils," *Materials Science and Engineering: A* 433 (2006) 334-342.
- [2] J. M. Conway, A. R. Ortiz, S. E. Jones, V. L. Acoff and X. Bu, Perforation Testing of a Titanium Alloy Target Using Hardened 4340 Steel Projectiles, in "Pressure Vessels & Piping Division" (ASME, Bellevue, WA, 2010) p. 1-6.

CHAPTER 3

ARB-PROCESSED TI/AL MULTILAYERED COMPOSITES SUBJECTED TO QUASI-STATIC LOADING

Abstract

Multilayered Composites (MLCs) are highly desirable materials that have become widely incorporated within various industries, especially aerospace and defense. Due to their physical qualities, such as high specific strengths, MLCs have become highly utilized within the defense industry. Within the defense industry, product survivability is of paramount importance. To ensure survivability, material selection is vital. For example, MLCs frequently offer beneficial energy absorption due to the anisotropic nature of their layered architectures. To study the anisotropic behavior of MLCs, the strengths of ARB-processed Ti/Al MLCs were investigated as a function of loading direction and applied load. The results of this study showed a significant difference in ultimate tensile strength for ARB-processed Ti/Al MLC tensile specimens that applied quasi-static loading parallel to the rolling direction versus perpendicular to the rolling direction.

3.1 Introduction

Multilayered Composites (MLCs) are advanced components that follow a repetitive stacking pattern. MLCs are often designed to be both strong and lightweight. Due to these physical properties, MLCs have become ideal candidates for military products such as impact resistant materials [1-3]. In multilayered materials, such as MLCs, anisotropy may have an influence on the potential application. Some processing methods for MLCs inherently induce anisotropy. Accumulative Roll Bonding (ARB) has been proven to be a viable method for processing Ti/Al and Ti/Al/Nb MLCs [4-8]. However, it has been shown that ARB processing of Ti/Al/Nb MLCs introduces texture, which can lead to anisotropic properties [9].

Texture is a term which describes the grain orientations in polycrystalline materials. Texture and anisotropy are materials characteristics which are directly related to each other. Therefore, anisotropy will increase as texture increases [10]. According to Beausir et al., anisotropy increases as the number of ARB cycles increases [11]. Layered materials frequently display anisotropy which can result in variations in the strength of a material [12].

Quasi-static testing is a valuable testing method that can be used to determine baseline mechanical properties [13,14]. Usually, the required strain rate for quasi-static tests is between 10^{-5}s^{-1} and 10^{-1}s^{-1} [15]. For metallic materials, mechanical testing is typically performed at a strain rate of 10^{-3}s^{-1} . At this rate, inertia and wave propagation effects will not influence the fracture behavior of the test specimen [16,17]. The goal of this study is to determine the influence of ARB processing direction on the ultimate tensile strength of ARB-processed Ti/Al MLCs.

3.2 Experimental Procedure

3.2.1 Materials and Accumulative Roll Bonding (ARB)

The MLCs produced in this study were composed of thin sheets (75 μ m) of commercially pure Ti and Al. To construct the composite, 21 sheets of Ti (11 layers) and Al (10 layers) were wired-brushed and stacked in an alternating fashion (as shown in Figure 3.1). The 21 stacked foils were fed through a rolling mill to achieve approximately a 50% reduction in thickness during the initial pass. A digital micrometer was used to measure thickness before and after each rolling step.

According to Chaudhari et al., 50% reduction is the ideal reduction needed to form a structurally sound MLC [18]. After obtaining approximately 50% reduction, the sample was sectioned, surfaced treated, restacked, and fed through the rolling mill again. This constituted one ARB cycle, as illustrated in Figure 3.2. This procedure was repeated until the desired number of cycles was obtained. In this experiment, all MLCs were processed to 4 ARB cycles. The rolling mill employed had a rolling diameter of 100mm and a roller width of 150mm. The rolling mill was operated at a speed of 410mm/s. Eq. 3.1 shows the formula for calculating reduction percentage for the ARB-processed Ti/Al MLCs used during this study [19].

$$R = \frac{\delta_b - \delta_a}{\delta_b} \quad (3.1)$$

where R is the reduction in thickness for the Ti/Al MLC, δ_b is the original stacking thickness of Ti/Al MLC prior to rolling, δ_a is the thickness of Ti/Al MLC after rolling.

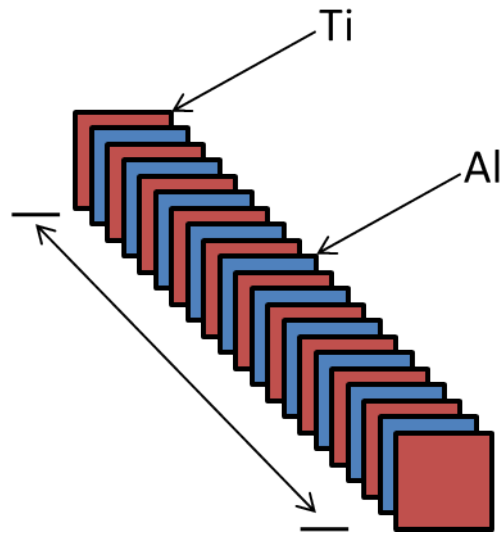


Fig. 3.1: Schematic of the Stacking Process

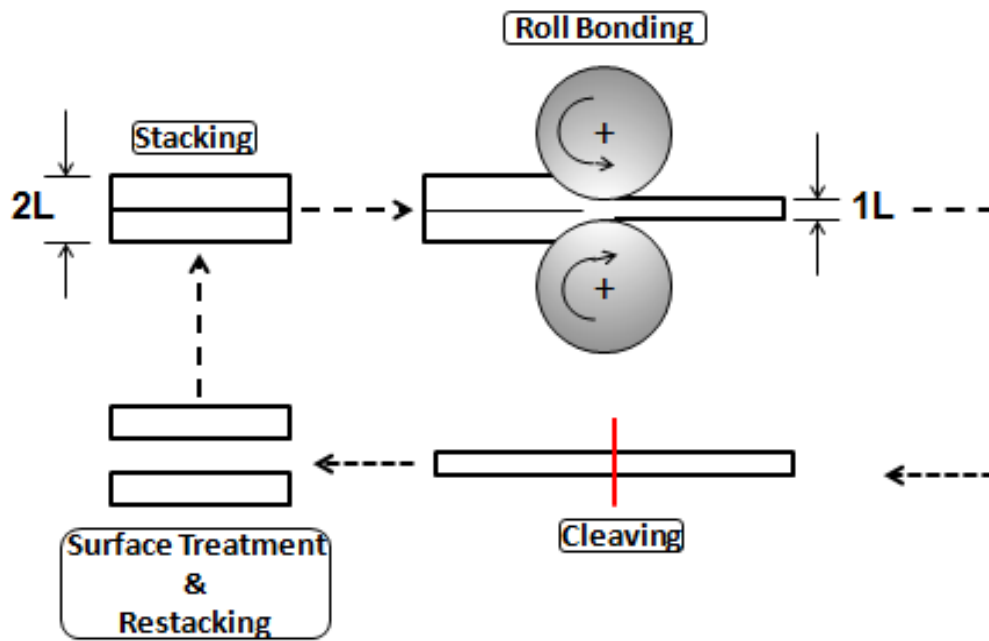


Fig. 3.2: Schematic of the ARB Process

3.2.2 Microstructural Characterization

Following the rolling process, the Ti/Al MLCs were sectioned, mounted in epoxy, and subjected to conventional metallographic procedures. The specimens were then characterized using a Scanning Electron Microscopy (SEM) equipped with an energy dispersive x-ray spectrometer (EDS). Characterization using Light Optical Microscopy (LOM) was also performed on the MLCs.

3.2.3 Mechanical Testing

Vickers microhardness data was obtained using a load of 300gf for duration of 10 seconds. A total of 10 hardness measurements were taken and the average was reported. To determine the mechanical properties under quasi-static conditions, the ARB MLCs were sectioned into tensile test specimens using a wire electrical discharge machine (EDM). The tensile specimens were cut parallel and perpendicular to the rolling direction as shown in Figure 3.3. The dimensions of the tensile test specimens are shown in Figure 3.4. The detailed dimensions are reported in Appendix A. All quasi-static data was collected on an electromechanical load frame at a strain rate of 10^{-3}s^{-1} . A clip on extensometer was used to record strain.

3.2.4 ImageJ Analysis

After quasi-static testing, ImageJ analysis was performed on the fracture surfaces of the tensile specimens. ImageJ, developed by the National Institutes of Health, is image processing analysis software that can be used to quantify images. In this study, ImageJ was used to determine the area fraction of Ti and Al in the failed tensile specimens.

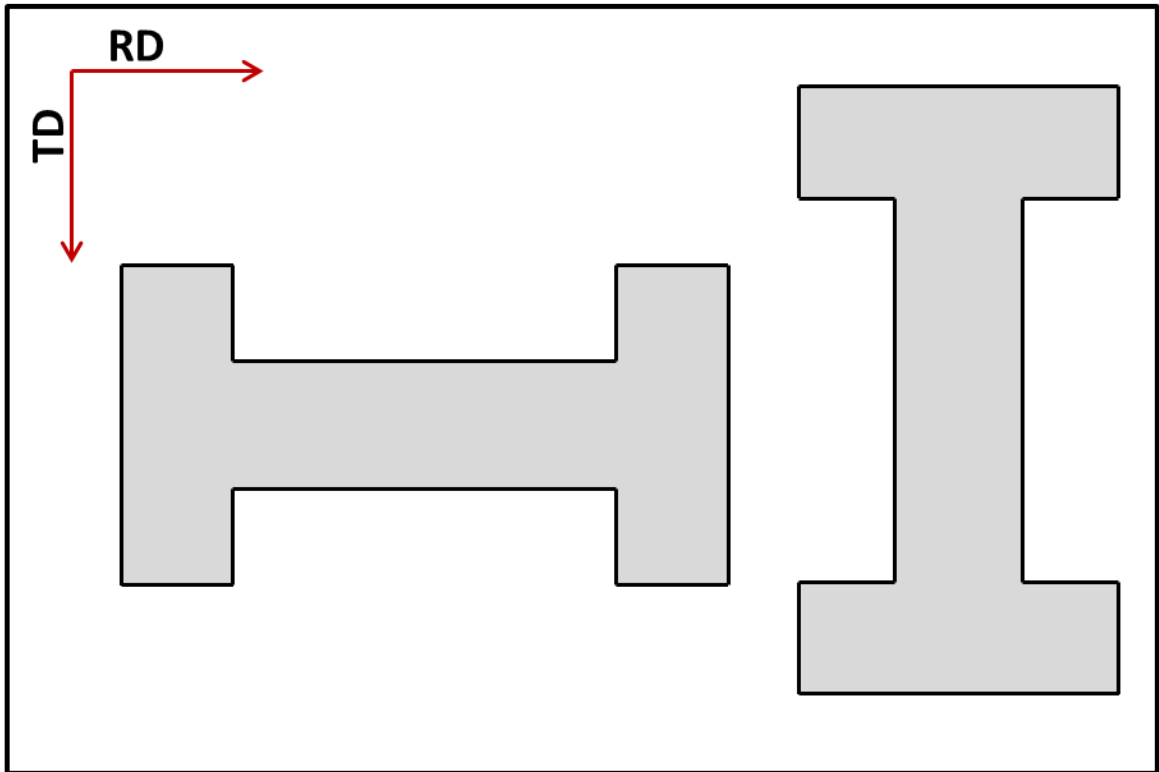


Fig. 3.3. Schematic Depicting Tensile Specimen Orientation During Machining Process

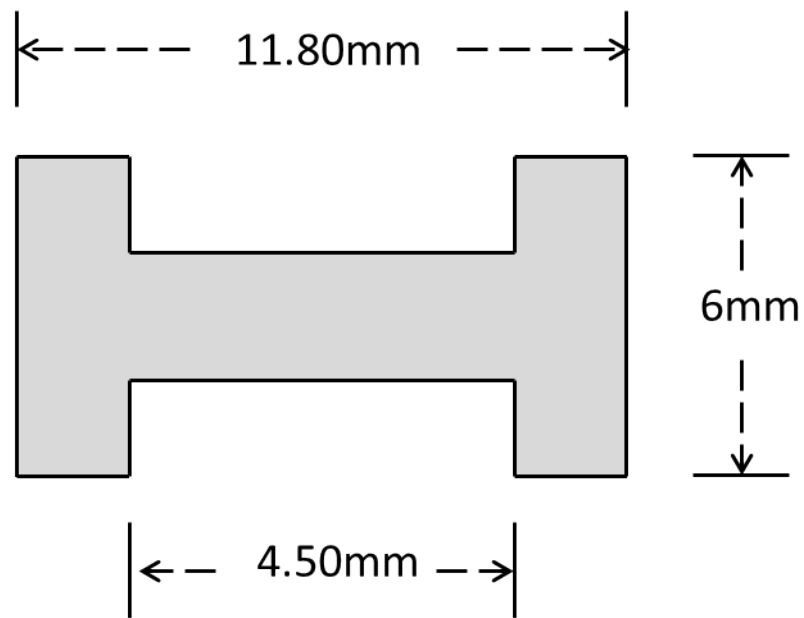


Fig. 3.4. Schematic of Tensile Specimen Dimensions

3.3 Results and Discussion

3.3.1 As-Roll Bonded Condition

Figure 3.5 is a representative LOM of the as-roll bonded condition. After the initial pass, the average layer thickness of the Ti was $55.4 \pm 9.87 \mu\text{m}$ and $53.7 \pm 7.50 \mu\text{m}$ for Al. Appendix B shows the images that were used for measurement. Vickers Hardness (HV) microhardness measurements were collected for the as-roll bonded condition. The average recorded Vickers hardness number (VHN), for this condition, was approximately 77.1 ± 24.4 with a range of 42.8 – 134.7. This range was due to Vickers indents being either completely in the Al or completely in the Ti.

3.3.2 Post-ARB Process

A representative microstructure after four ARB cycles is shown in Figures 3.6. Figure 3.6A shows the SEM secondary electron image and 3.6B shows the LOM image. To determine the effects of the ARB process as a function of hardness, Vickers microhardness measurements were collected similar to what was done for the as rolled condition. The average microhardness for the Post-ARB condition was 106 ± 8.18 (Ranged from 102.4 – 121.6 VHN). The results were an average of 10 measurements each taken from a total of four specimens. During testing, indents were often placed on both the Ti and the Al areas simultaneously.

As shown in Figure 3.6A, the Ti breaks into fragments while the Al forms a supportive matrix around the Ti fragments. This phenomenon occurs due to the difference in yield strength between both the Ti and Al. This occurrence adds difficulty to accurately determining the individual layer thickness. Therefore, to determine quantifiable Post-ARB layer thicknesses, multiple measurements must be taken of both the deformed Ti fragments as well as the Al

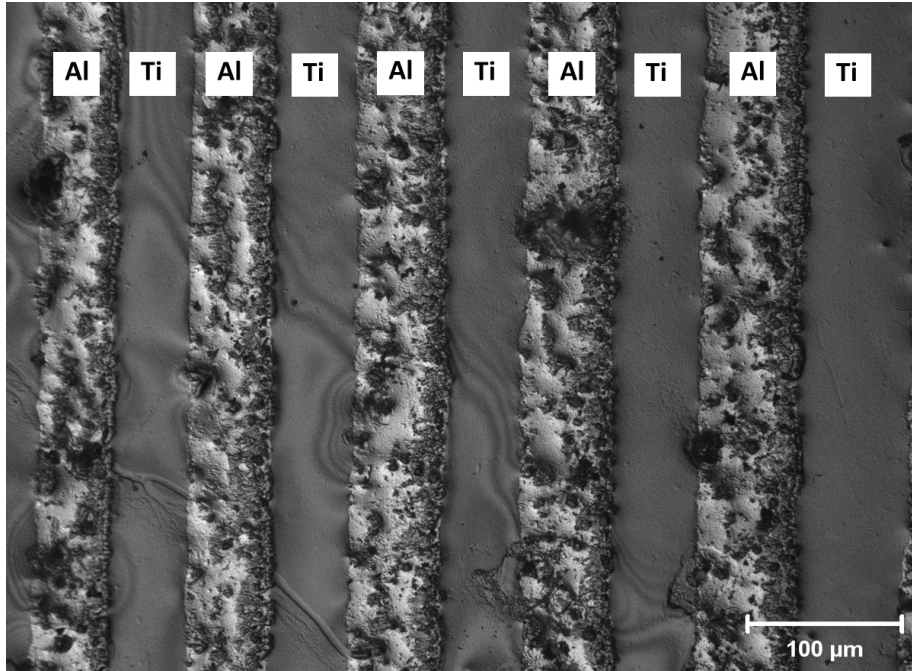


Fig. 3.5. Light Micrograph of a Ti/Al MLC in As Roll Bonded Condition

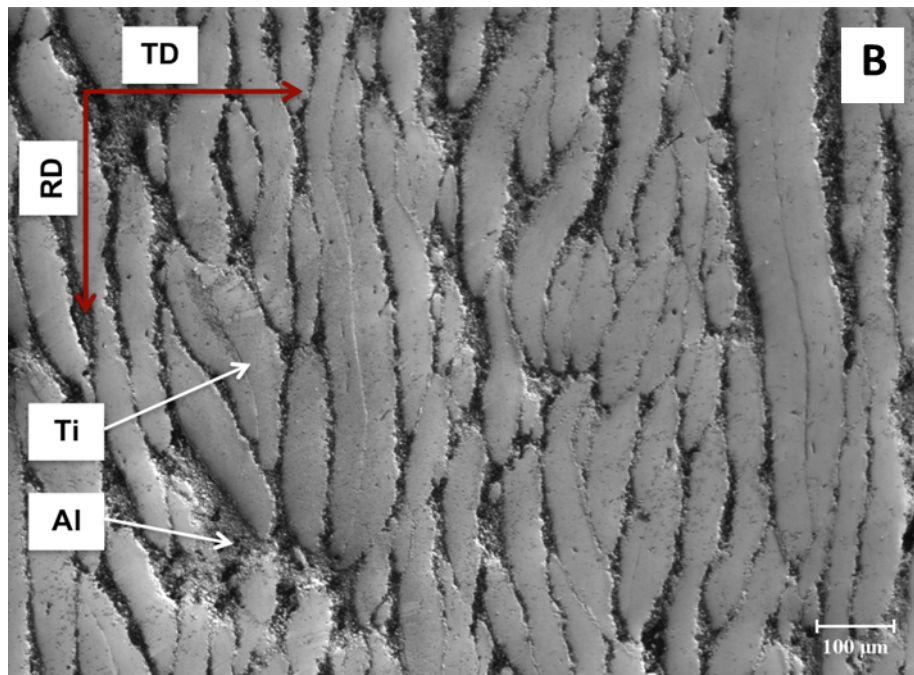
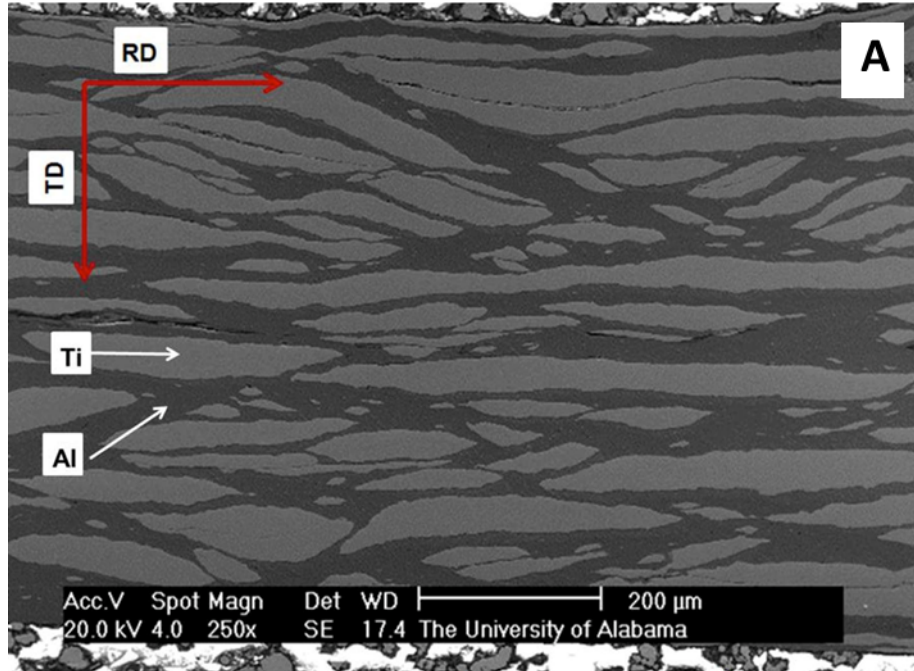


Fig. 3.6. Micrographs of Ti/Al MLC after 4 ARB Cycles
 (A) SEM Secondary Electron Image (B) Light Micrograph Image

matrix. After 4 ARB cycles, 80 thickness measurements (per element) were collected to determine the thickness of the newly deformed MLC. For Ti, the average fragment thickness was $22.4 \pm 6.65 \mu\text{m}$. In terms of the newly formed Al matrix, an average matrix spacing of $19.1 \pm 10.2 \mu\text{m}$ was collected. The images used for measurement are shown in Appendices C and D. From observing the thicknesses in both the as-rolled and post-ARB conditions, it can be stated that the rate of reduction is similar for both Ti and Al. Although there is a similarity in the layer thicknesses, the Al appeared to be slightly more deformed in both the as-rolled and post-ARB condition. This is a result of the difference in yield strengths between the two elements.

3.3.3 Quasi-Static Testing

To observe the potential presence of anisotropy in the ARB-processed Ti/Al MLCs, the specimens in this study were subjected to quasi-static loading. In both the rolling and transverse directions, the strain rate that was used for this study was 10^{-3}s^{-1} . At this rate, it is possible to avoid inertia and wave propagation effects [20].

In this study, three independent sample groups (Sample Q, Sample R, and Sample T) were tested. Each sample group was processed from different Ti/Al MLCs. Each MLC was manufactured with the same processing procedure. Within each sample group, the ultimate tensile strength (UTS) was determined for both the RD and TD. Three dog bone tensile specimens were tested in each sample group for both the RD and the TD (18 total specimens) as shown in Table 3.1. It was observed that the TD specimens all had higher UTS values. The average UTS for the TD was $202 \pm 35.9 \text{MPa}$ compared to $55.6 \pm 40.8 \text{MPa}$ for the RD (as shown in Figures 3.7 and 3.8 respectively). The disparity in the UTS values is evidence that anisotropy exists within ARB-processed Ti/Al MLCs. This is clearly observed in Figure 3.9.

Table 3.1. Ultimate Tensile Strength of ARB-Processed Ti/Al MLCs Determined Using Quasi-Static Loading

Specimen	Loading Direction (MPa): RD	Loading Direction (MPa): TD
Q-1	1.72	162.13
Q-2	123.74	164.87
Q-3	71.06	190.32
R-1	23.87	242.15
R-2	0.87	239.59
R-3	56.03	228.70
T-1	72.17	216.95
T-2	90.37	148.65
T-3	60.73	221.91

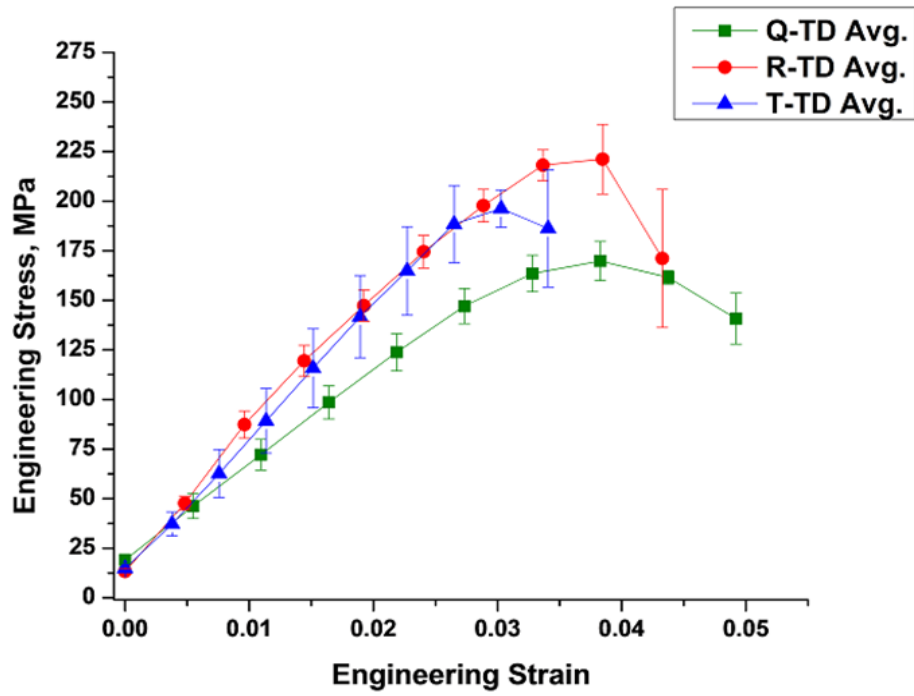


Fig. 3.7. Average Engineering Stress vs. Average Engineering Strain Plot of Specimens Tested in the Transverse Direction (TD)

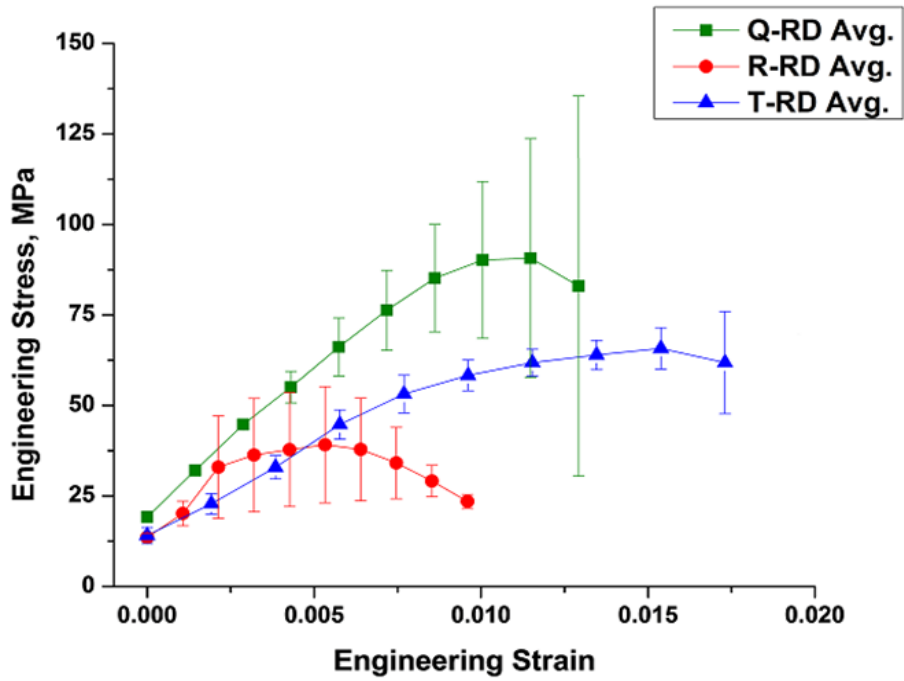


Fig. 3.8. Average Engineering Stress vs. Average Engineering Strain Plot of Specimens Tested in the Rolling Direction (RD)

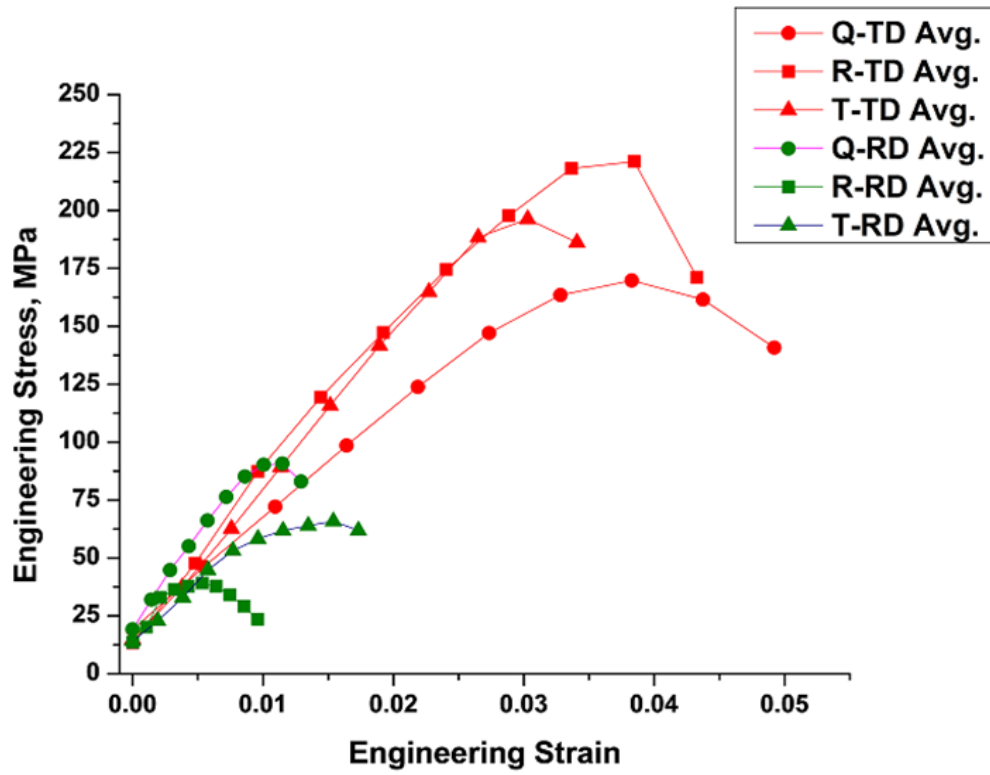


Fig. 3.9. Average Engineering Stress vs. Average Engineering Strain Plot That Compares Strength as a Function of Processing Direction

3.3.4 Scanning Electron Microscopy (SEM)

After quasi-static testing, SEM was performed to identify any possible microstructural correlations that might exist as a function of loading direction. Figures 3.10 -3.13 show fracture surfaces from specimens that were tested parallel to the rolling direction. In general, the fracture surface exhibited a mixture of features with no obvious fracture initiation site.

Figure 3.11 shows images of higher magnifications from region “a” in Figure 3.10. This region has characteristics of transgranular fracture. The presence of transgranular fracture is evident due to the high amounts of cleavage throughout the microstructure.

Figure 3.12 shows higher magnification of the boxed region “b” in Figure 3.10. Figure 3.13 shows higher magnification of boxed region “c”. Similar to Figure 3.11, both Figures 3.12 and 3.13 show characteristics of transgranular fracture. This mode of fracture was also observed for the other specimens that were subjected to testing in the rolling direction (RD).

Figure 3.14 shows the fracture surface of one of the specimens that was sectioned perpendicular to the rolling direction. Figures 3.15 – 3.17 show fracture surfaces from specimens tested in the transverse direction. Figure 3.15 shows the left edge of the fracture surface. The characteristic of the failure mode is ductile in nature. This is evident from the presence of dimpling or cup/cone formations. Dimpling occurs due to tensile tearing, which is how ductile materials absorb energy prior to failure [21]. Figures 3.16 and 3.17 are from the middle and the right, respectively, of Figure 3.13. These figures also show dimpling and cup/cone formation throughout the fracture surfaces. In the TD specimens, it appears as if more ductile failure occurred. Observation of the other specimens loaded in the transverse direction revealed similar fracture surfaces as those shown in Figures 3.15-3.17.

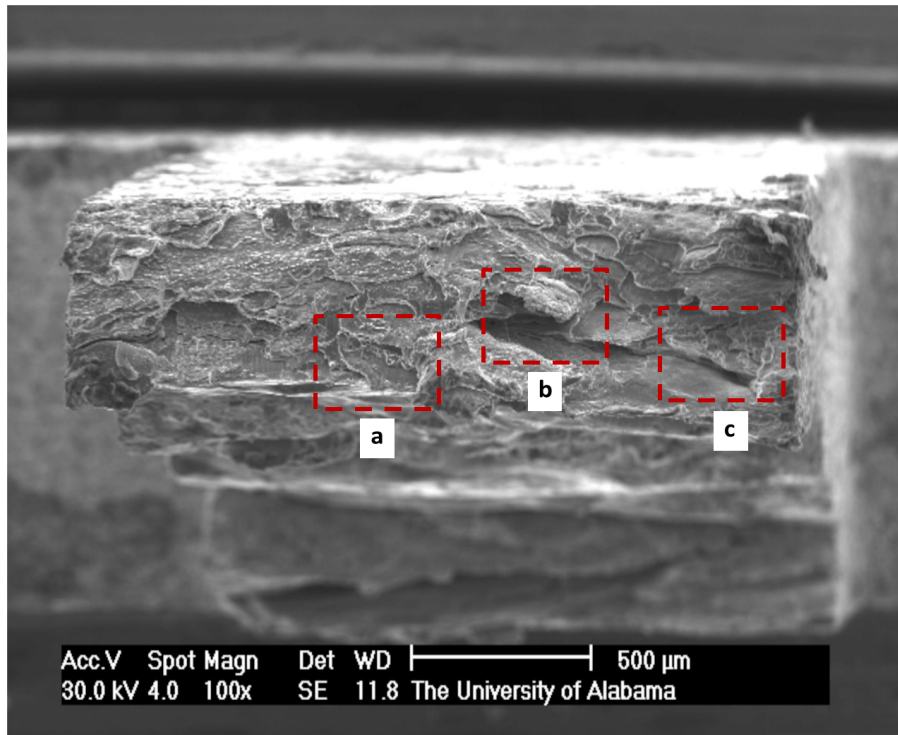


Fig. 3.10. SEM Micrograph of Fractured Specimen Made From ARB-Processed Ti/Al MLC. Specimen was Loaded Parallel to the Rolling Direction (Sample ID: Q-RD-2)

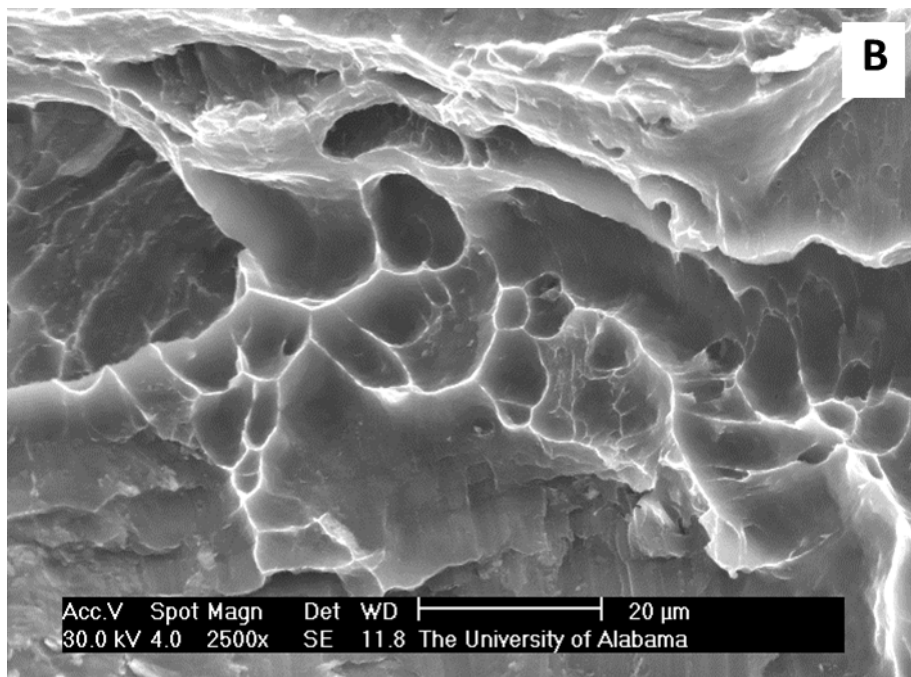
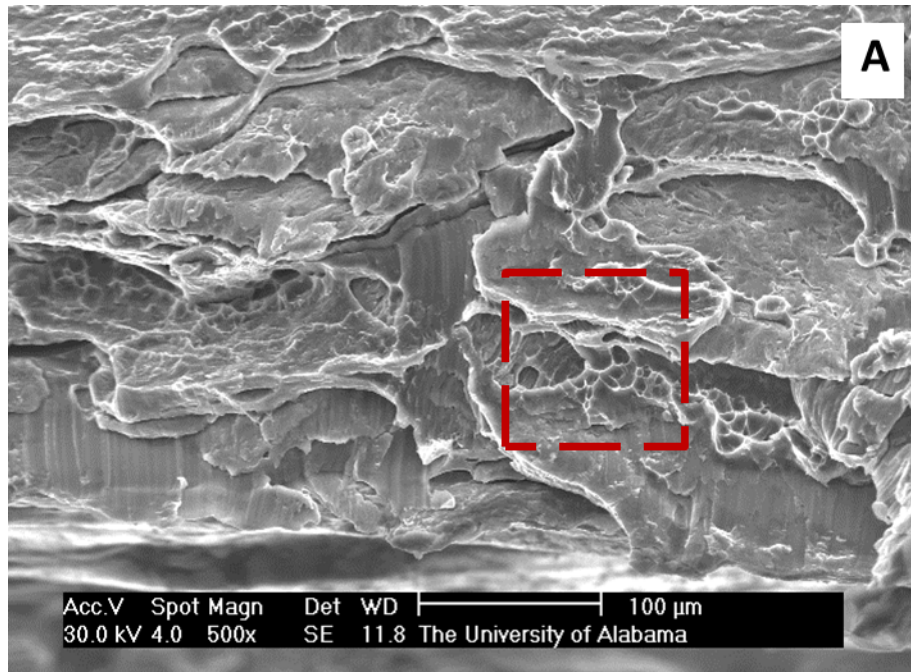


Fig. 3.11(A) Higher Magnification of Boxed Region “a” in Fig. 3.10. (B) Higher Magnification of Boxed Area in (A)

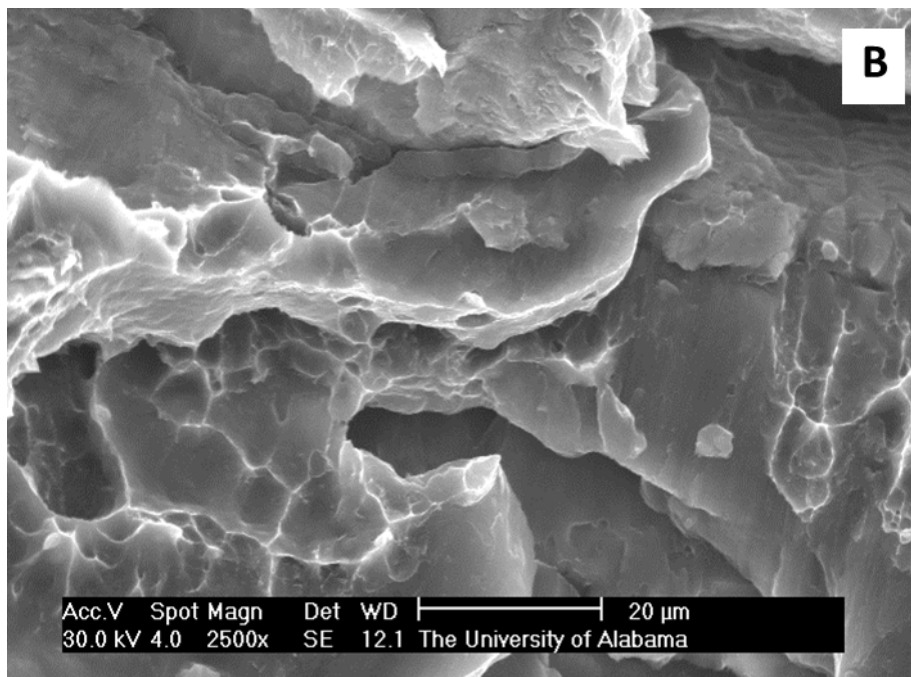
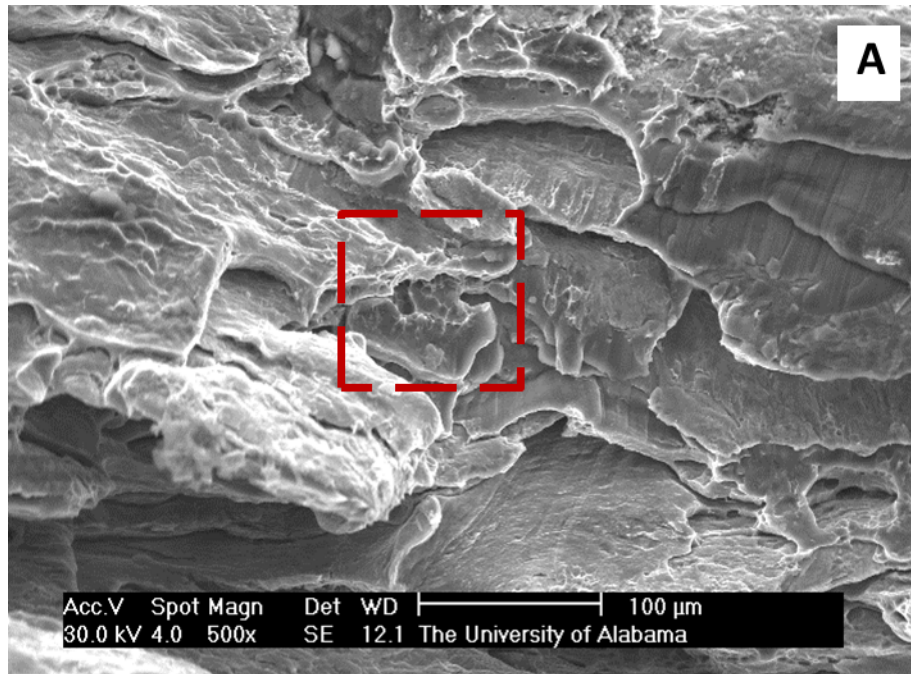


Fig. 3.12. (A) Higher Magnification of Boxed Region “b” in Fig. 3.10. (B) Higher Magnification of Boxed Area in (A)

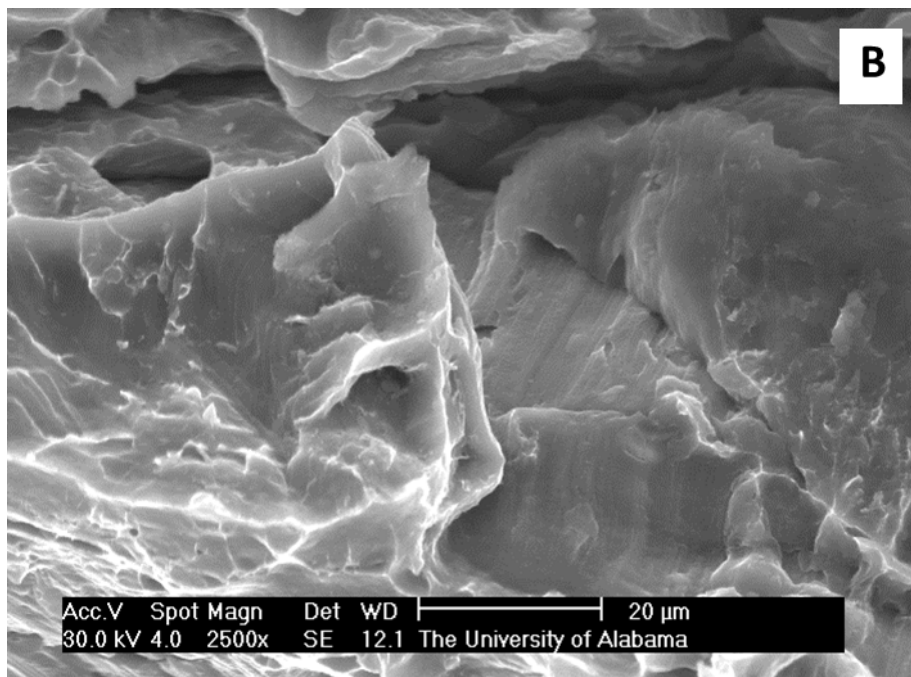
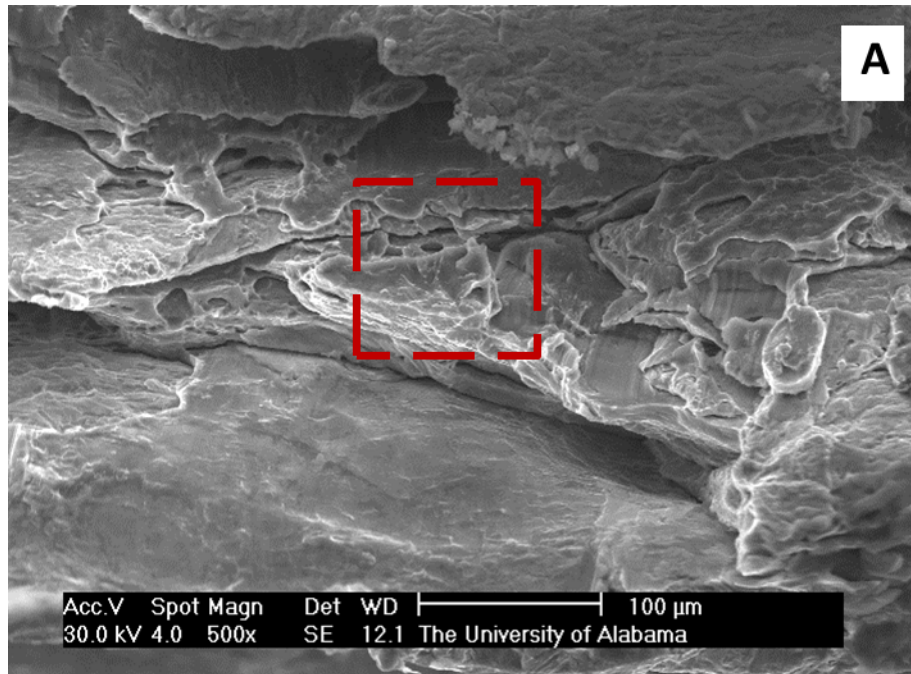


Fig. 3.13. (A) Higher Magnification of Boxed Region “c” in Fig. 3.10. (B) Higher Magnification of Boxed Area in (A)

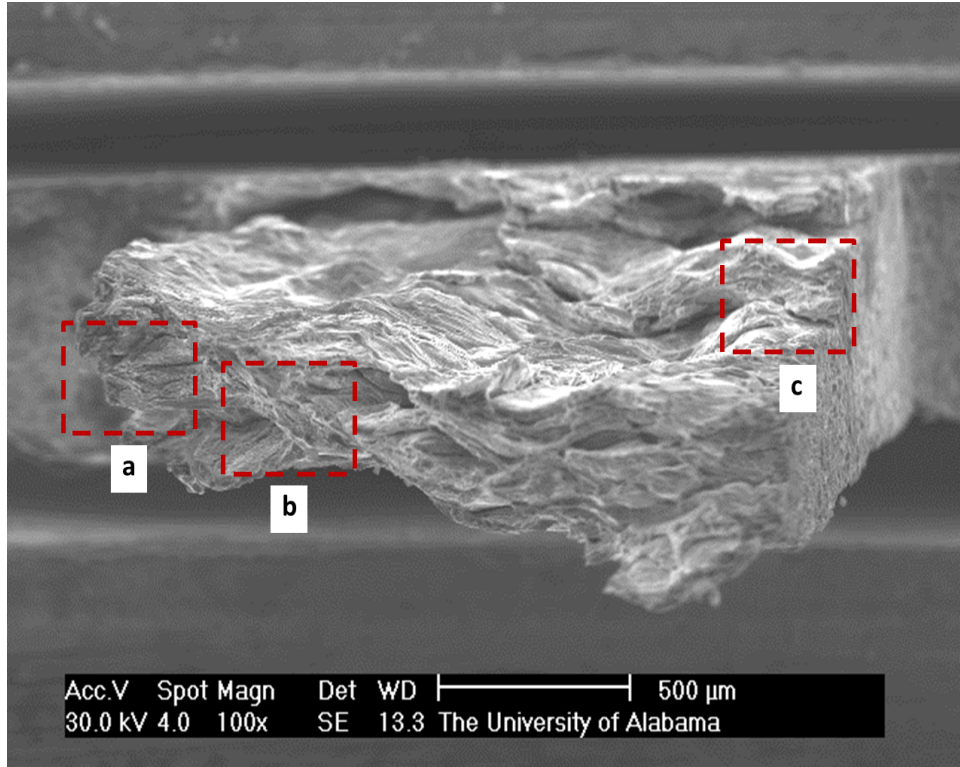


Fig. 3.14. SEM Micrograph of Fractured Specimen Made From ARB-Processed Ti/Al MLC. Specimen was Loaded Perpendicular to the Rolling Direction (Sample ID: T-TD-2)

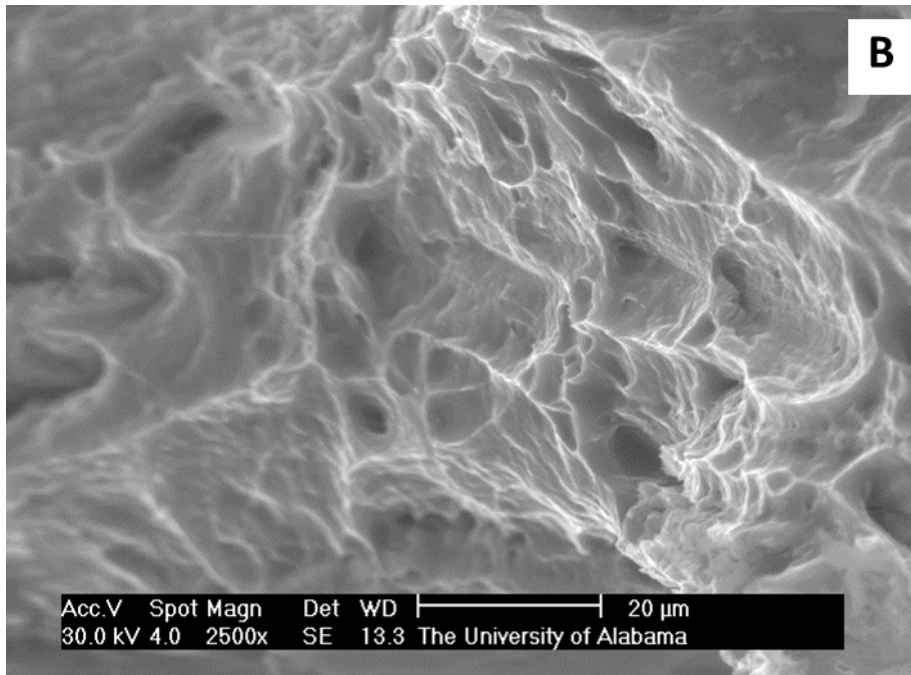
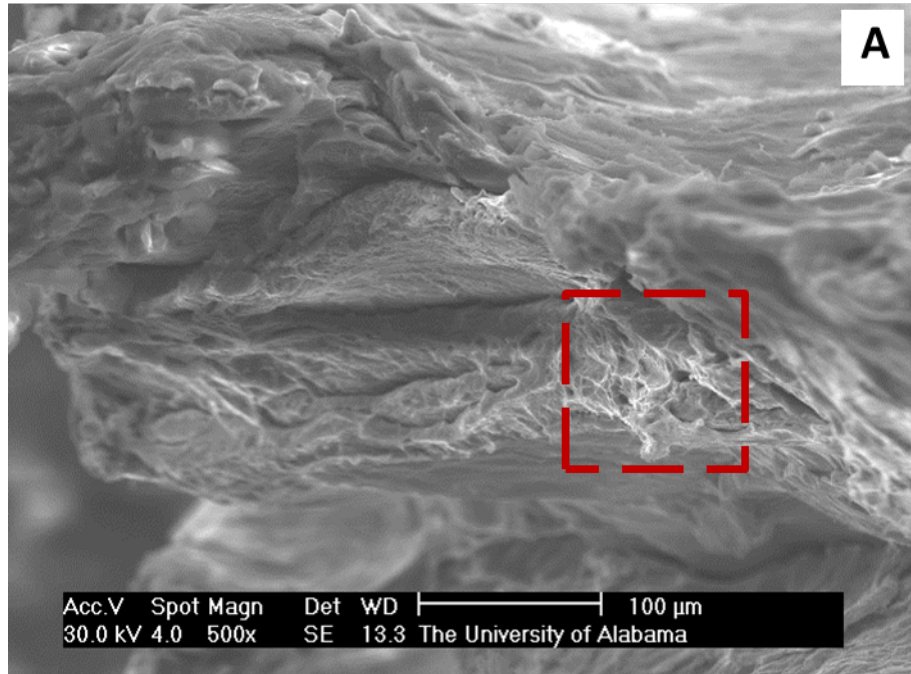


Fig. 3.15. (A) Higher Magnification of Boxed Region “a” in Fig. 3.14. (B) Higher Magnification of Boxed Area in (A)

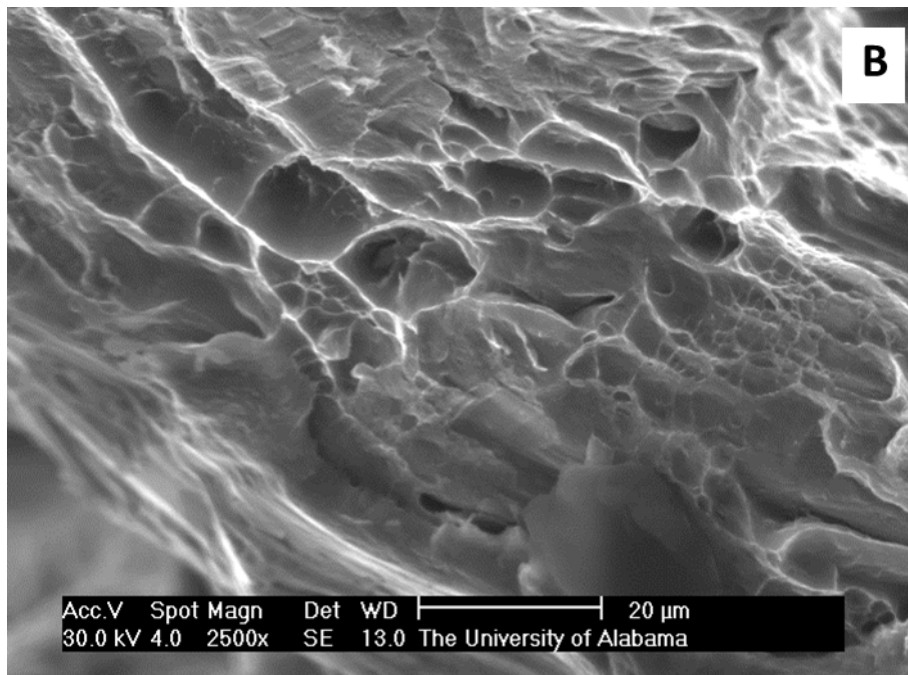
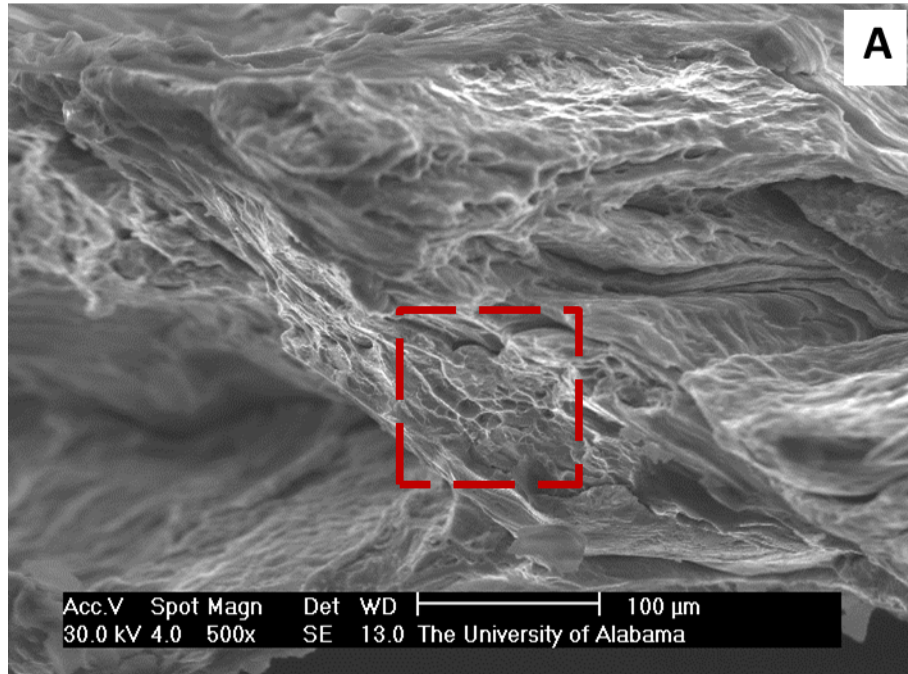


Fig. 3.16. (A) Higher Magnification of Boxed Region “b” in Fig. 3.14. (B) Higher Magnification of Boxed Area in (A)

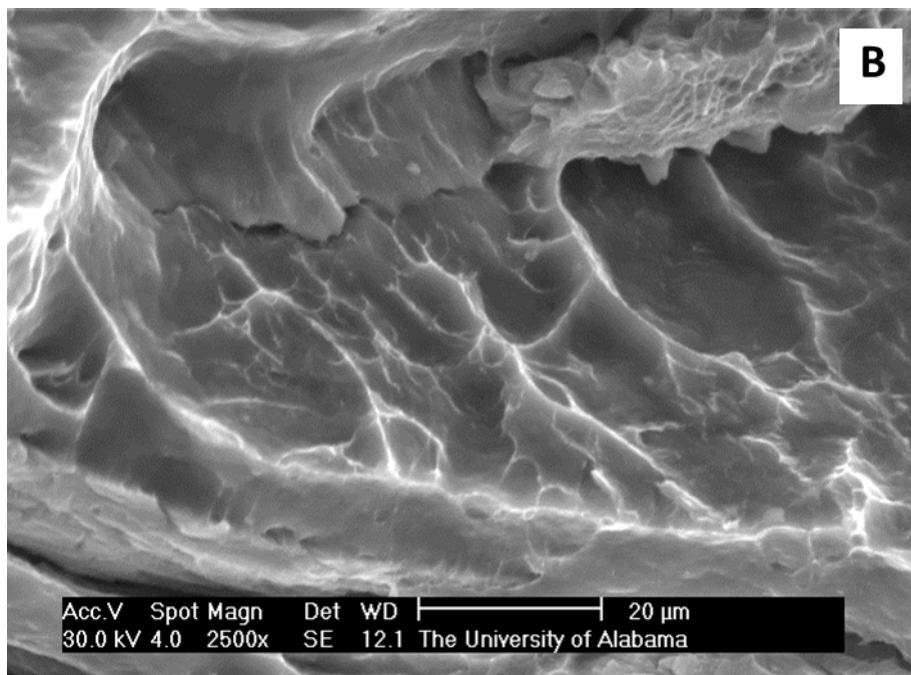
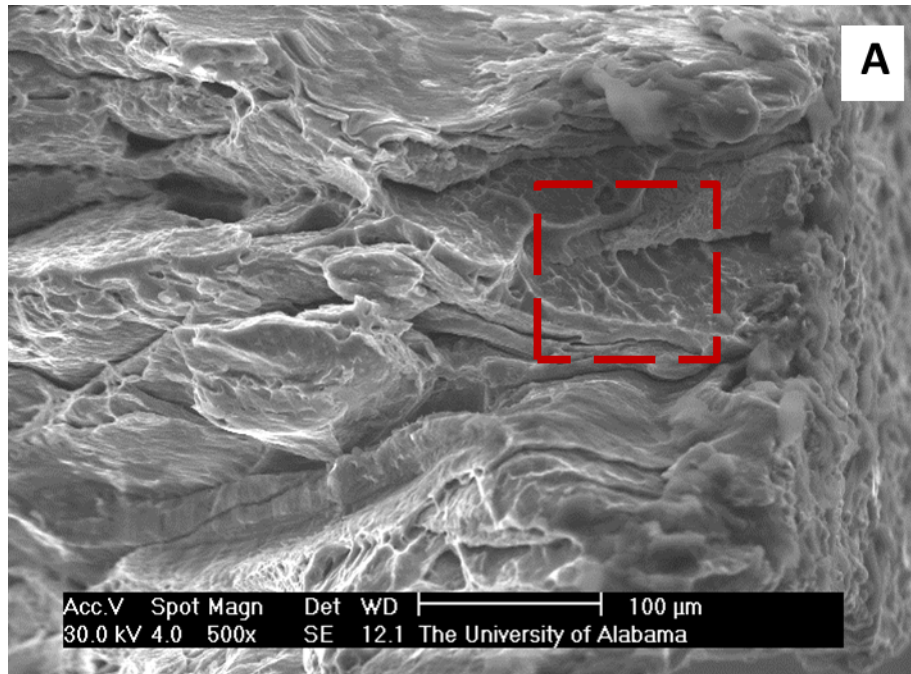


Fig. 3.17. (A) Higher Magnification of Boxed Region “c” in Fig. 3.14. (B) Higher Magnification of Boxed Area in (A)

Upon completion of SEM evaluation, it was determined that microstructural similarities exist within the fracture surface as a function of loading direction. The specimens loaded in the RD exhibited mostly transgranular fracture whereas those loaded in the TD exhibited mostly cup/cone formations. Figures 3.11-3.13 and 3.15-3.17 confirm that ductile deformation, via tensile tearing, is more prominent for the specimens that were loaded in the TD versus the specimens loaded in the RD. This also supports the quasi-static data plotted in Figures 3.7-3.9, which shows that an average UTS of 202 ± 35.9 MPa was obtained for the TD compared to an average UTS of 55.6 ± 40.8 MPa in the RD. Thus, the ARB-processed Ti/Al MLCs subjected to loading in the transverse direction resulted in a higher UTS (as shown on Figure 3.9). This corresponded to ductile failure modes as observed using SEM.

3.3.5 Structure-Property Relationship

To gain an understanding of why there exists a significant difference in the mechanical performance of the tensile specimens, it was necessary to conduct a microstructural analysis of both the RD and TD specimens. To establish a connection between mechanical performance and microstructure, it was required to have knowledge of the initial condition of the tensile specimens prior to applying the load. Therefore, samples Q-RD-3 and Q-TD-3 were chosen as representatives for LOM analysis. A portion of the base metal was sectioned from both samples. After standard metallographic preparation, both the RD and TD specimens were analyzed via a LOM. The LOM images shown in Figure 3.18 show the relative amounts of Ti to Al within the RD and TD base metal cross sections. The light micrographs revealed that Ti was less prominent in the RD specimen (as shown in 3.18a) than in the TD specimen (as shown in Figure 3.18b). Upon conducting ImageJ analysis, it was observed that the RD specimen (Q-RD-3) had a Ti area

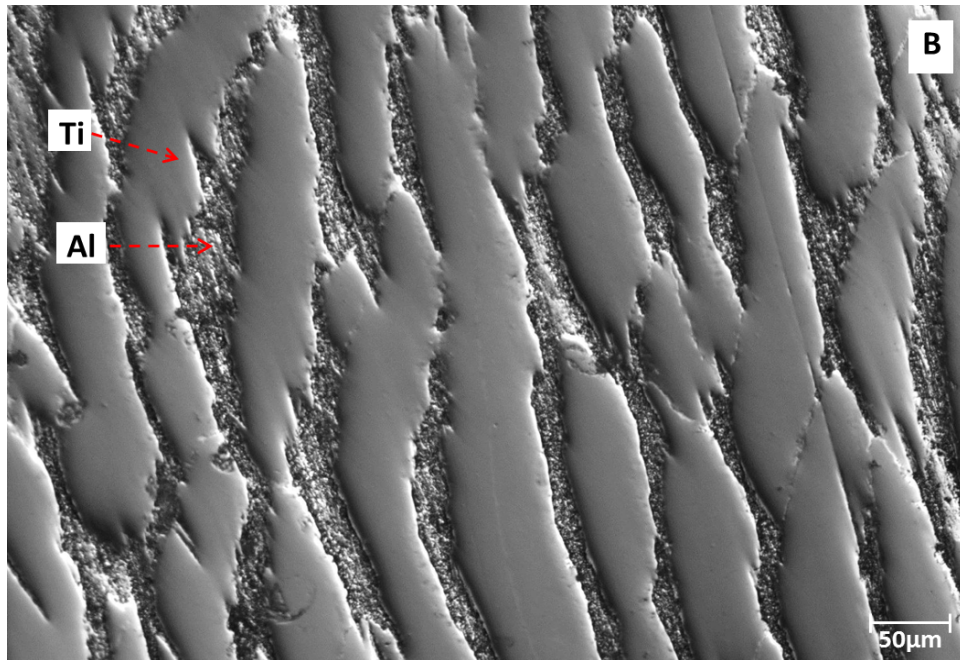
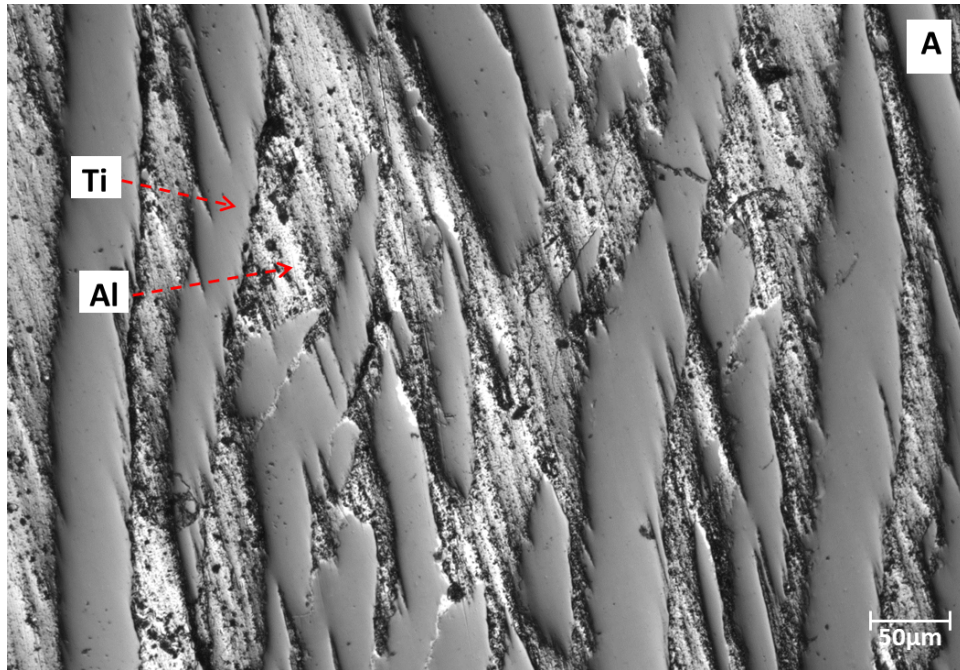


Fig. 3.18. Light Micrograph Images of Ti/Al MLC Tensile Specimens Subjected to Quasi-Static Loading: Sample Q-3. (A) Rolling Direction (B) Transverse Direction

fraction of 51.7% while the TD specimen (Q-TD-3) had a significantly larger Ti area fraction of 72.0%. Due to the lower Ti area fraction in the RD tensile specimen (sample Q-RD-3), a much lower UTS value was observed in the RD specimen rather than in the TD specimens (sample Q-TD-3). Upon analyzing other tensile specimens, the same microstructural trend was observed between the RD and the TD specimens.

After LOM analysis, compositional mapping was performed on the fracture surfaces of the failed RD and TD specimens using EDS. This technique was used to determine if additional microstructural evidence could be found to support the data found during LOM analysis. The compositional map shown in Figure 3.19 shows the relative amount of aluminum to titanium in the fracture surfaces of the failed Ti/Al ARB-processed tensile specimens. Figure 3.19a is a compositional map of the fracture surface of the RD specimen while Figure 3.19b is a compositional map of the fracture surface of the TD specimen. This data also confirms that the RD tensile specimens are Al rich while the TD tensile specimens are Ti rich. This supports the microstructural data obtained using LOM analysis which showed less Ti for the RD. Through LOM and EDS compositional analysis, it can be definitively stated that the lack of Ti rich regions in the RD tensile specimens led to the lower UTS values compared to the TD tensile specimens.

3.4 Conclusions

From the data presented, it can be unequivocally stated that ARB-processed Ti/Al MLCs are anisotropic materials. Through quasi-static loading, it was evident that processing direction directly influences the UTS within ARB-processed Ti/Al MLCs. Data shows that the UTS of ARB-processed Ti/Al dog bone specimens will be significantly larger in the transverse direction

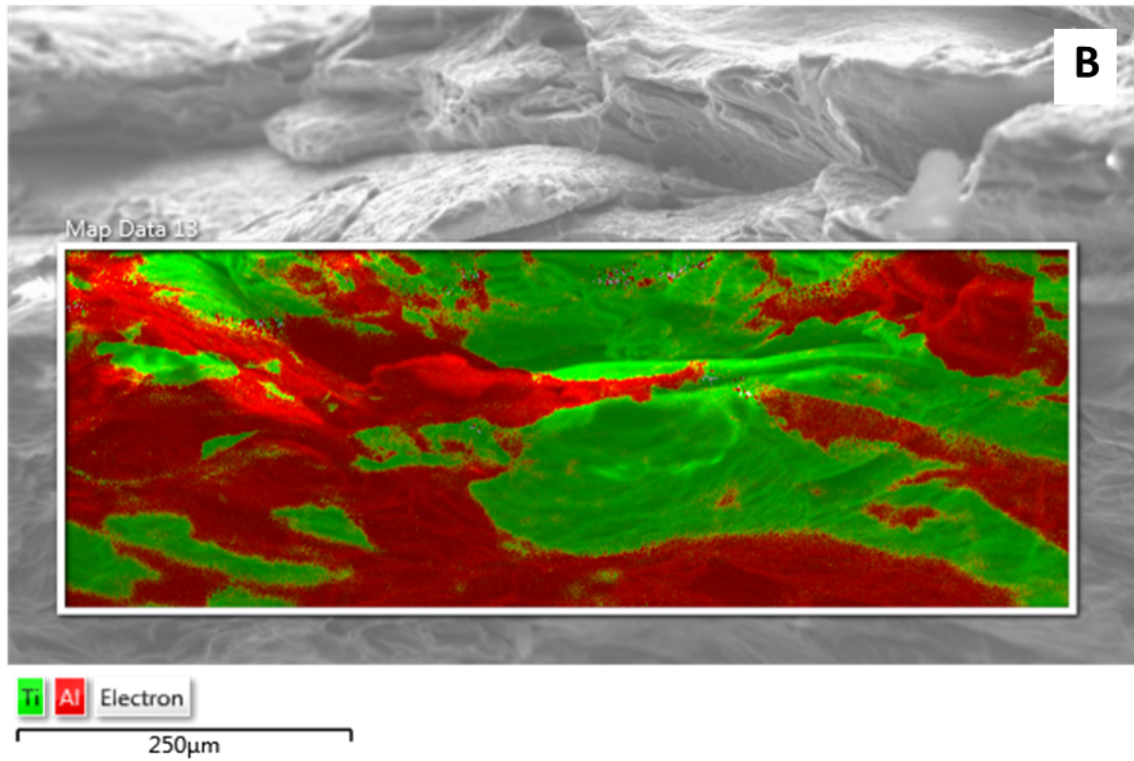
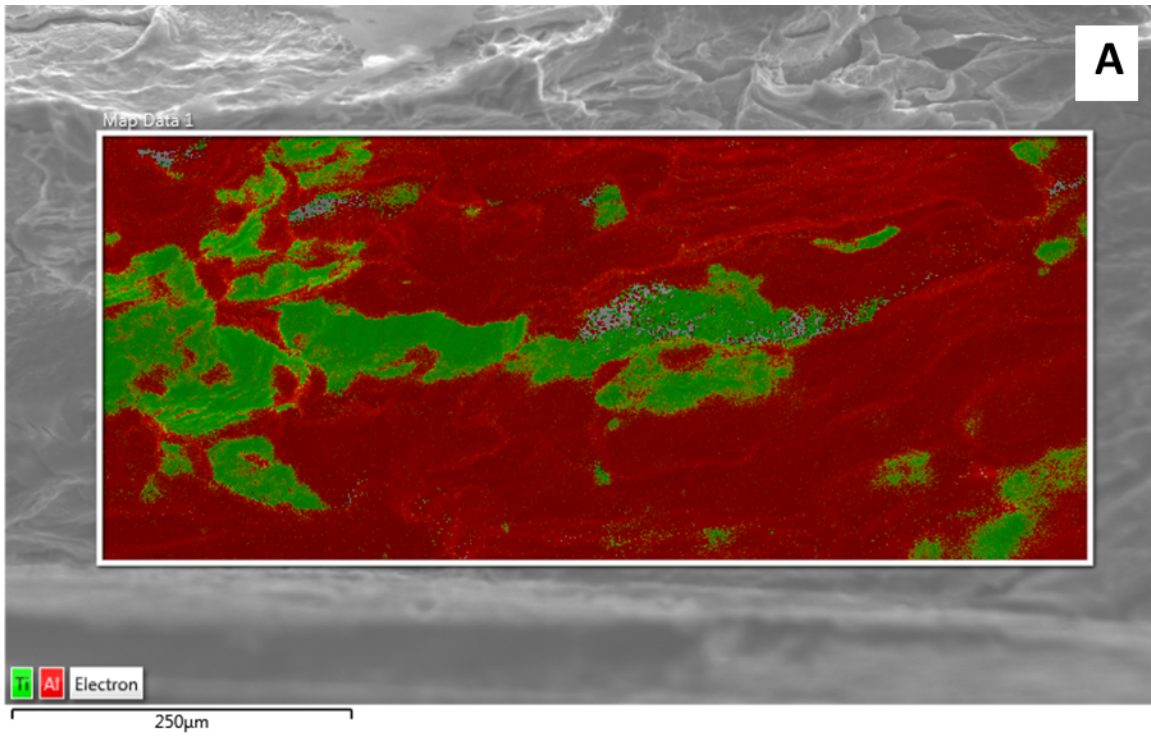


Fig. 3.19. Compositional Map of Fractured Tensile Specimen: Sample R-1. Green Depicts Ti whereas the Red Depicts Al (A) Rolling Direction (B) Transverse Direction

than in the rolling direction. EDS and LOM analysis provide microstructural evidence that supports the data collected during the quasi-static tests. Compositional mapping suggests that the presence of Ti rich regions in the TD specimens influenced the mechanical behavior and increased the UTS values (in comparison to the RD specimens). Furthermore, SEM analysis suggests that the RD tensile specimens failed due to transgranular fracture while the TD specimens failed due to ductile failure, specifically tensile tearing. This statement is supported by the presence of cleavage-like shearing throughout the fracture surfaces of the RD tensile specimens and the high amounts of dimpling in the fracture surfaces in the TD tensile specimens.

3.5 References

- [1] A. Patselov, B. Greenberg, S. Gladkovskii, R. Lavrikov and E. Borodin, "Layered Metal-intermetallic Composites in Ti-Al System: Strength Under Static and Dynamic Load," *AASRI Procedia* 3 (2012) 107-112.
- [2] H. L. Gower, D. S. Cronin and A. Plumtree, "Ballistic impact response of laminated composite panels," *International Journal of Impact Engineering* 35 (2008) 1000-1008.
- [3] E. S. C. Chin, "Army focused research team on functionally graded armor composites," *Materials Science and Engineering: A* 259 (1999) 155-161.
- [4] G. P. Chaudhari and V. Acoff, "Cold roll bonding of multi-layered bi-metal laminate composites," *Composites Science and Technology* 69 (2009) 1667-1675.
- [5] G. P. Chaudhari and V. L. Acoff, "Titanium aluminide sheets made using roll bonding and reaction annealing," *Intermetallics* 18 (2010) 472-478.
- [6] J.-G. Luo and V. L. Acoff, "Using cold roll bonding and annealing to process Ti/Al multi-layered composites from elemental foils," *Materials Science and Engineering: A* 379 (2004) 164-172.
- [7] J.-G. Luo and V. L. Acoff, "Processing gamma-based TiAl sheet materials by cyclic cold roll bonding and annealing of elemental titanium and aluminum foils," *Materials Science and Engineering: A* 433 (2006) 334-342.
- [8] R. Zhang and V. L. Acoff, "Processing sheet materials by accumulative roll bonding and reaction annealing from Ti/Al/Nb elemental foils," *Materials Science and Engineering: A* 463 (2007) 67-73.
- [9] L. Zhou, The texture-structure relationship in Ti-Al-Nb multilayered composites processed by accumulative roll bonding, Ph.D. Dissertation, The University of Alabama, 2014.
- [10] T. Chen, Z. Chen, L. Yi, J. Xiong and C. Liu, "Effects of texture on anisotropy of mechanical properties in annealed Mg-0.6%Zr-1.0%Cd sheets by unidirectional and cross rolling," *Materials Science and Engineering: A* 615 (2014) 324-330.
- [11] B. Beausir, J. Scharnweber, J. Jaschinski, H. G. Brokmeier, C. G. Oertel and W. Skrotzki, "Plastic anisotropy of ultrafine grained aluminium alloys produced by accumulative roll bonding," *Materials Science and Engineering: A* 527 (2010) 3271-3278.

- [12] X. Deng, N. Chawla, K. K. Chawla, M. Koopman and J. P. Chu, "Mechanical Behavior of Multilayered Nanoscale Metal-Ceramic Composites," *Advanced Engineering Materials* 7 (2005) 1099-1108.
- [13] M. Meyers and K. Chawla, Mechanical Behavior of Materials, 2nd edition (Cambridge University Press, New York, 2009).
- [14] G. E. Dieter, Mechanical Metallurgy, (New York : McGraw-Hill, c1986. 3rd ed., 1986).
- [15] J. Zhang, C.-w. Tan, Y. Ren, F.-c. Wang and H.-n. Cai, "Quasi-static and dynamic tensile behaviors in electron beam welded Ti-6Al-4V alloy," *Transactions of Nonferrous Metals Society of China* 21 (2011) 39-44.
- [16] J. J. Harrigan, S. R. Reid and C. Peng, "Inertia effects in impact energy absorbing materials and structures," *International Journal of Impact Engineering* 22 (1999) 955-979.
- [17] Testing Machines and Strain Sensors, in "ASM Handbook" (ASM International, Materials Park, OH, 2000).
- [18] G. P. Chaudhari, K. Serin and V. L. Acoff, "Processing Ultrafine Grained Composites of Elemental Titanium and Aluminium by Severe Plastic Deformation," in Ultrafine Grained Materials III, edited by Y. T. Zhu, T. G. Langdon, R. Z. Valiev, S. L. Semiatin, D. H. Shin and T. C. Lowe (TMS, 2004).
- [19] J.-G. Luo, Processing Near Gamma-Based TiAl by Cold Roll Bonding and Diffusion Reaction of Elemental Titanium and Aluminium Foils, Ph.D. Dissertation, The University of Alabama, 2001.
- [20] J. C. Huang, Y.-S. Lo and G. T. Gray III, "The response of metal-matrix composites subjected to quasi-static and shock-wave deformation," *Materials Chemistry and Physics* 35 (1993) 71-85.
- [21] R. Mahmudi, "Ductile tearing energy of aluminium alloy sheets determined by the single tensile testing (STT) method," *Journal of Materials Processing Technology* 118 (2001) 316-320.

CHAPTER 4

THE EFFECTS OF VARYING BALLISTIC PARAMETERS ON THE OBSERVED FAILURE MODE IN ARB-PROCESSED TI/AL MULTILAYERED COMPOSITES

Abstract

Within the defense industry, mechanically enhanced multilayered composites (MLCs) have shown promise as candidates for impact resistant applications. This study focuses on accumulative roll bonded (ARB) MLCs that are comprised of alternating layers of elemental titanium (Ti) and aluminum (Al) foils. Due to a high specific strength, Ti/Al MLCs are being considered for potential utilization in ballistic and aerospace applications. In this study, Ti/Al MLCs, processed via ARB, were subjected to impact testing (or perforation testing). In this study, the relationship between ballistic parameters and the failure mode of ARB-processed Ti/Al MLCs were investigated. It was observed that strong microstructural correlation exists between both projectile impact velocity and projectile apex angle. Experimental results showed that ductile deformation was dominant on the fracture surface. The amount of ductile deformation increased as projectile impact velocity decreased and projectile nose angle increased.

4.1 Introduction

Multilayered composites (MLCs) are comprised of multiple layers of materials that often follow a repetitive pattern. MLCs have shown promise in military applications, specifically for ballistics and armor development [1,2]. MLCs are promising materials because engineered components can be designed to be lightweight while maintaining low densities and high strengths [3]. Previous research have shown that MLCs which contain materials from the titanium family (e.g. TiAl_3) are prime candidates for structural and military applications [4]. According to Kumar, MLCs with alternating layers of hard and soft materials have shown promise in stopping incoming projectiles [5].

Although there are numerous methods to process MLCs, most existing methods are complex. Accumulative roll bonding (ARB) has been proven as a viable, simplistic method for processing Ti/Al MLCs [6-11]. The ARB technique is an ultra-high straining process that uses the force from rolling pins to induce the formation of dislocations within a metal [12-14]. ARB is an efficient processing technique because of its ability to lower activation energy by adding stored energy (through mechanical deformation) into the material [15].

Impact tests are often used to investigate the mechanical properties of MLCs. Traditionally, common impact testing methods include derivatives of charpy impact tests, drop weight impact tests, and ballistic (or high velocity impact) tests. These methods are beneficial because they may assist in understanding the energy absorption of a given material during impact [16]. The focus of this study is the use of perforation testing to determine the ballistic limits of ARB-processed Ti/Al MLCs.

A thorough understanding of failure modes is vital to assessing the damage and failure modes that result from impact testing. In metallic materials, there are four main types of failures

modes: dimple rupture, cleavage, fatigue, and decohesive rupture [17]. There is a characteristic fracture surface appearance and fracture mechanism associated with each failure mode.

Dimple rupture, a type of ductile failure, often occurs in metallic materials. In metals, signs of dimple rupture can be identified in the form of microvoid coalescence. As strain increases, a metallic material begins to fail (via slip) and indentions begin to occur within the microstructure. There are multiple types of dimple rupture. For this study, the most relevant types of dimple rupture are tensile tearing and dimple shearing. Tensile tearing is identified through the formation of cup/cone depressions (or “dimples”) within the microstructure. In dimple shearing, a shearing or stretching often occurs within the dimpled region due to the presence of high strain rates and/or large amounts of shearing deformation [18]. Both forms of dimple rupture occur as a result of void nucleation, growth, and eventual microvoid coalescence.

Another important mode of failure is known as cleavage. Cleavage fractures are a type of brittle failure because they require low amounts of energy for failure to occur. In metals, cleavage failures often occur at low temperatures or due to high strain rates. This type of failure usually occurs in stronger materials. This result, despite having a high strength, is because of the associated low fracture toughness [19]. Upon failure, accelerated crack propagation (along cleavage planes) is due to a material’s inability to hinder crack propagation [20]. Cleavage failures are identified by very flat, featureless deformation.

Fatigue is a very common mode of failure in engineering systems. Material fatigue is brought on due to the presence of cyclic loading. As a result of cyclic loading, materials often fail well below their associated tensile strength. Fatigue failures account for roughly 90% of engineering-based failures. For a material to fail, the process of slip must occur. Generally in cyclic loading, slip bands widen and fatigue cracks often occur within these bands [21]. Fatigue

failures exhibit three stages: Stage I (Crack initiation), Stage II (Crack propagation), and Stage III (Failure). Fatigue failures are often associated with clam shell markings that radially radiate from the fracture origin [16].

The last common failure mode, for metallic materials, is decohesive rupture. Decohesive rupture occurs when failure occurs without the presence of dimple rupture, cleavage, or fatigue failures. Decohesive rupture typically occurs due to reactive environments (e.g. hydrogen embrittlement). This type of failure usually occurs on the surfaces and within the grain boundaries of materials. Failures, within this type of mode of deformation, generally are the result of phases changes (e.g. oxidation) [21].

Studies have shown that varying ballistic factors (e.g. projectile impact velocity, projectile apex angle, and target size) has an effect on the dominating failure mode within metallic structures. To date, there are no published works on the failure modes of ARB-processed Ti/Al MLCs. Therefore, the objective of this study is to determine the materials response of ARB processed Ti/Al MLCs that were subjected to high impact loading.

4.2 Experimental Procedure

4.2.1 Sample Preparation

In this study, all elemental foils were approximately 75 microns thick with a commercial purity of 99%. The desired Ti/Al MLCs consisted of a total of 21(11 titanium and 10 aluminum) foils. Each foil was sectioned into 7.62mm x 7.62mm sheets. After sectioning, each foil was subjected to a surface preparation treatment that consisted of degreasing and wire-brushing. Acetone was used as the degreasing agent to remove any latent oils left on the surface. After degreasing, wire-brushing was used to further treat the surface of the foils. Wire brushing allowed for the removal of any oxide layers that may have formed and it facilitates a good

mechanical bond throughout the multilayered structure. Once the sample preparation for each foil was complete, the foils were stacked in an alternating fashion.

4.2.2 Accumulative Roll Bonding (ARB)

The alternatively stacked Ti and Al foils were fed through the rolling mill to achieve approximately 50% reduction. Prior researchers showed that the ideal reduction percentage required to achieve a stable bond in the first pass was approximately 50% [9]. After the initial pass, the foils bonded to form a solid material. This step is considered to be the “as-rolled” condition. Once in the as-rolled condition, the sample was sectioned into two halves and restacked. The restacked sample was fed through the rolling mill again, as shown in Figure 4.1. This is considered to be one ARB cycle. This procedure was repeated until 4 ARB cycles were completed which yielded a coupon thickness of approximately 1mm.

4.2.3 Impact Testing

The projectiles used for this study were constructed from 4340 steel. All projectiles consisted of a 0.308 caliber (7.8mm diameter) and were 50.8mm long. The average mass was approximately 14.9g. To ensure structural integrity, the projectiles were hardened to a Rockwell C Hardness (HRC) number of 55. Only the MLC targets (and not the projectiles) were intended to fail upon impact. Therefore, substantial hardness was required to ensure that the projectiles would survive repeated impact trials. The Ti/Al MLC targets were subjected to a rigorous perforation regimen that consisted of varying the ballistic parameters (impact velocities and projectile nose geometries). The projectiles, as shown in Figure 4.2, varied in conical nose angle as follows: 30°Apex, 60°Apex, 90°Apex and 180°.

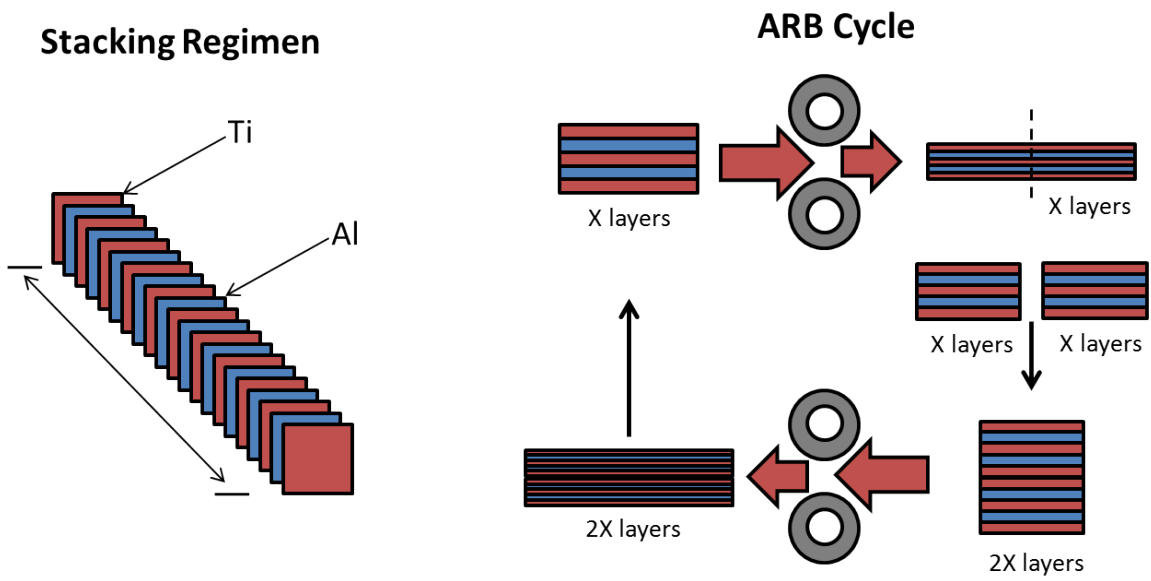


Fig. 4.1. A Schematic of the ARB Stacking Sequence and Processing Technique.



Fig. 4.2. Test Projectiles with Varying Nose Geometries:
(A) 30° (B) 60° (C) 90° (D) 180°

The ballistic apparatus used is shown in Figure 4.3. The testing apparatus consisted of: a smooth bore barrel, gun breach, firing solenoid, target fixture, lasers, chronographs, cable, and a sand trap. The smooth bore barrel was designed to house a Winchester 348 cartridge case. Prior to firing the apparatus, the projectiles were loaded into the barrel then sealed by a gun breach. Attached to the gun breach was a firing solenoid. This solenoid operated under the same function as a firing pin because it was responsible for igniting the gun powder inside of the ballistic casings. Hercules “Green Dot” shotgun powder was used in this study. To fire the apparatus, an electric pulse was sent to an iron plunger. The process operated similar to a firing hammer: the plunger struck the solenoid and ignited the gunpowder within the ballistic casings. Once the gunpowder was ignited, an explosion occurred and the projectiles were propelled through the gun barrel towards the awaiting Ti/Al MLC target. The variation of the gun power had a direct effect on the observed impact velocity.

After firing, but prior to impact, the projectiles broke through a set of lasers that were designed to determine the impact velocity. After the impact velocity was collected, the projectile struck the Ti/Al MLC target which was 15.3cm away from the gun muzzle. The projectile continued through the chronographs where the residual velocities were then collected.

4.2.4 Scanning Electron Microscopy (SEM)

A Phillips XL30 Scanning Electron Microscope was used to perform a thorough examination of the Ti/Al MLC fracture surfaces to determine if the rigorous perforation regimen

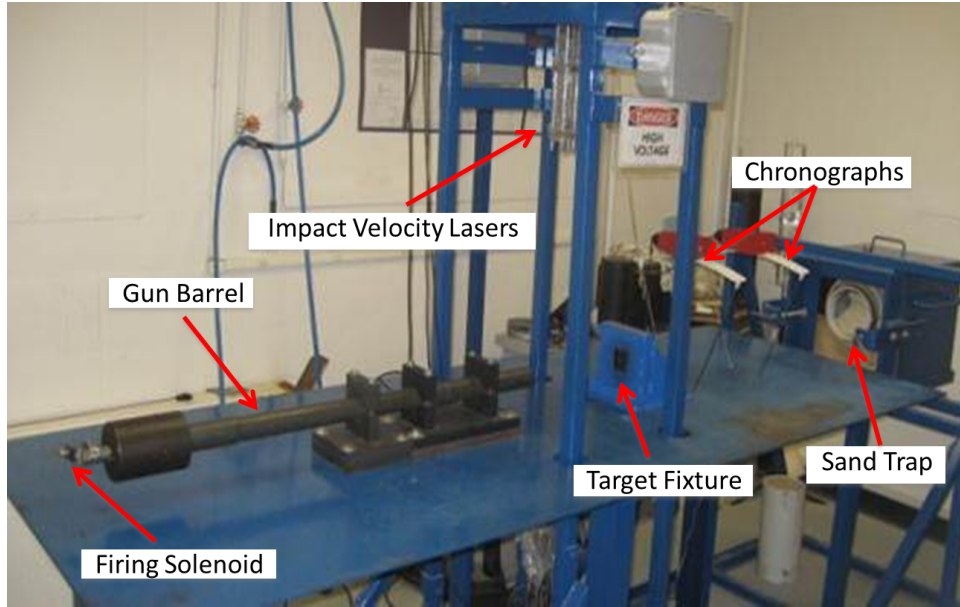


Fig. 4.3. Ballistic Apparatus

led to any unique material responses. A JEOL 7000 SEM equipped with an energy-dispersive spectrometer (EDS) was used to perform Back-scattered Electron (BSE) imaging and compositional analysis. Compositional mapping of representative fracture surfaces was performed to distinguish between the Ti and Al in the fracture surfaces.

4.3 Results and Discussion

4.3.1 Projectile Impact Velocity

In this experiment, the Ti/Al MLC targets were perforated with impact velocities that ranged from 95m/s to 230m/s. Representative specimens for both the lowest and highest impact velocities employed are shown in Figure 4.4. In perforation testing, according to Woodard, impact velocity is one of the key factors that influence the dominating failure mode. Shifting of failure modes, due to varying impact velocities, causes microstructural changes to occur within the fracture surfaces of a perforated target [22]. Targets that are perforated at slower impact velocities are typically dominated by ductile deformation, specifically, tensile tearing or dimpling [23]. Tensile tearing typically results in the formation of dimples throughout the failure site. In Figures 4.5 and 4.6, the projectile's apex angle and the target size were held constant to isolate the effects of impact velocity.

In Figure 4.5, the target was perforated by a 60° nose projectile at an impact velocity of 121m/s. This micrograph shows an example of tensile tearing deformation. This trend drastically changes as impact velocity increases. Targets perforated by faster impact velocities tend to experience more shearing deformation (specifically shear plugging, shear banding, or dimple elongation) [24]. At faster impact velocities, elongated dimples (denoted as dimple shearing) can be formed throughout the microstructure. An example of this type of shearing deformation can be seen in Figure 4.6. This target was perforated by a 60° nose projectile at an impact velocity of

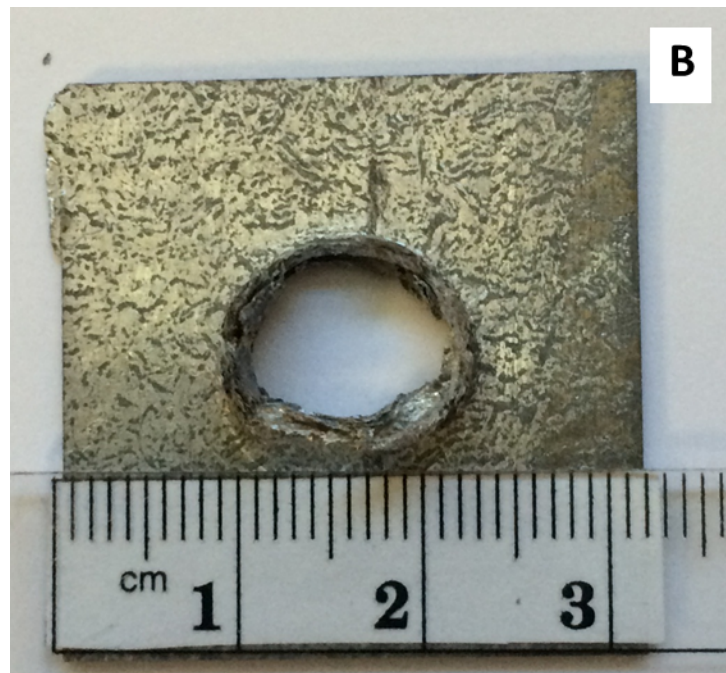
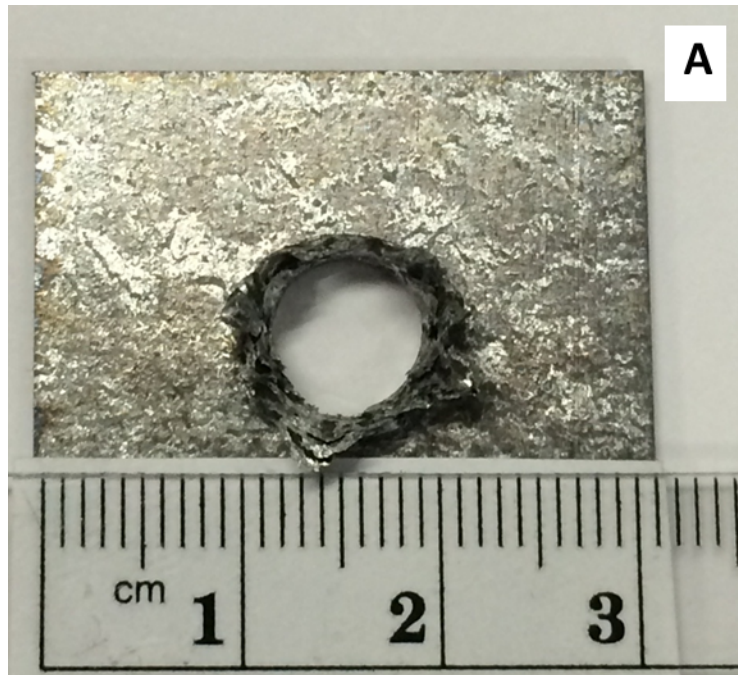


Fig. 4.4. Representative of ARB-Processed Ti/Al MLC Targets Subjected to Perforation Testing.
(A) Sample E2: Perforated at 95m/s by a 30° Projectile
(B) Sample I3: Perforated at 213m/s by a 90° Projectile

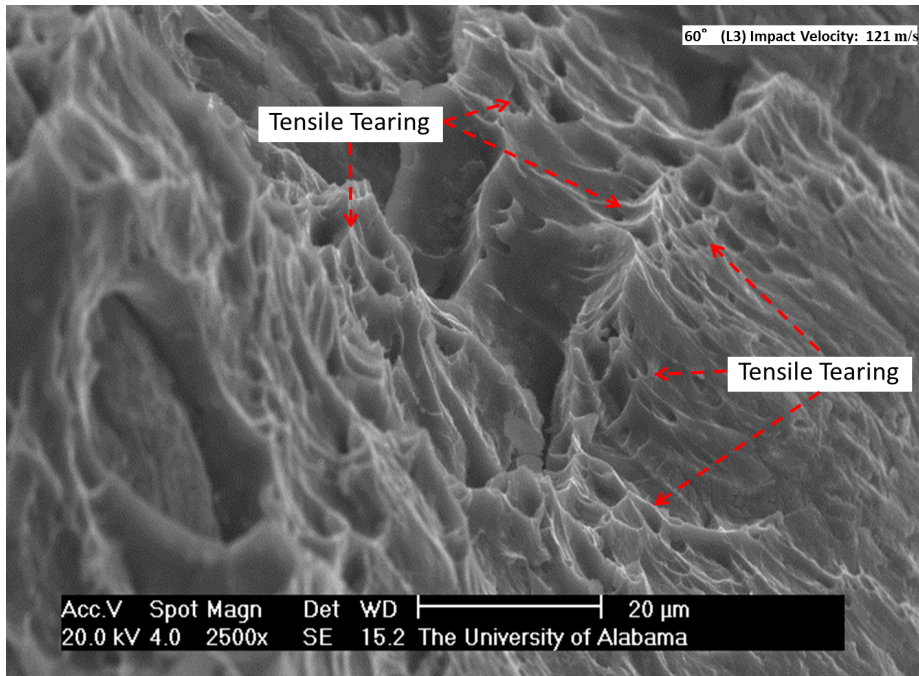


Fig. 4.5. 2.54cm x 2.54cm MLC (Sample L3)
 Subjected to Perforation by a 60° Projectile at 121m/s

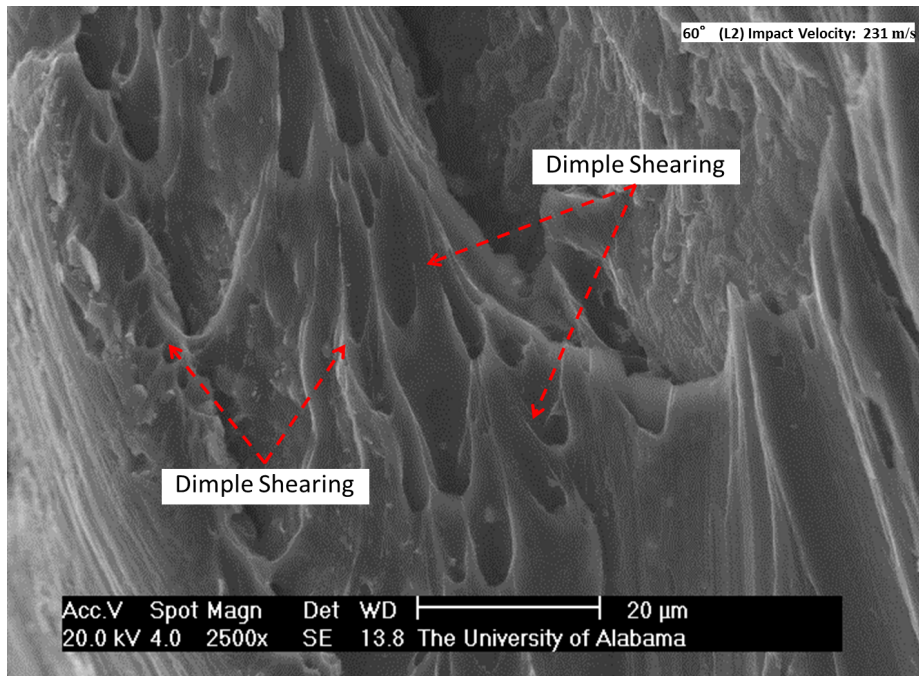


Fig. 4.6. 2.54cm x 2.54cm MLC (Sample L2)
 Subjected to Perforation by a 60° Projectile at 231m/s

Previous studies show that impact velocity has an effect on energy absorption [3,23,25-28]. According to Conway et al., it can also be derived that the work W_P , of a projectile, is equal to the difference in kinetic energy. Thus, mathematically, it can be stated:

$$W_P = \frac{1}{2}m_P V_{OP}^2 - \frac{1}{2}m_P V_{RP}^2 \quad (4.1)$$

Where, in terms of the projectile, work is W_P , mass is m_P , impact velocity is V_{OP} , and residual velocity is V_{RP} [27]. This equation is crucial because it provides insight as to how projectiles affect which failure modes are dominant. Data from this equation also can provide information regarding the overall observed microstructural damage. Based on work from Teng and Wierzbicki, regarding the effects of impact velocity, there are three possible failure modes for solid targets struck by rigid projectiles. In ascending order of impact velocity, the failure modes are: tensile tearing, shear plugging, and adiabatic shear banding [23]. Eq. 4.1, describes the amount of work that is done by the projectile onto the target. By calculating energy, it is possible to establish a connection between impact data and microstructural observations. This theory is supported by the Figures 4.5 and 4.6. In Figure 4.6, the projectile moved much faster (than in Figure 4.5) and less work was done on the sample by the projectile. Therefore, the material was not able to absorb as much energy prior to perforation. This is why the dimple shearing, rather than tensile tearing, occurred throughout the microstructure.

4.3.2 Effect of Projectile Apex Angle

Another essential ballistic parameter that influences dominating failure mode is projectile apex angle. According to Gupta et al., nose shape is a vital factor to consider because it directly affects deformation mechanisms and energy absorption [29]. In the present study, the projectile apex angle was varied while the target size was kept constant. The impact velocity was held as

consistent as possible. By holding the impact velocity relatively constant, a microstructural evolution of the fracture surface as a function of projectile apex angle can be observed. The effect of varying projectile apex angle is shown in Figures 4.7-4.10. These figures are representative of the entire fracture surface for each specimen shown.

In Figure 4.7, the MLC target was perforated at an impact velocity of 129m/s by a projectile with a 30° apex angle. In this image, a very small amount of ductile deformation is observed. With sharp nose projectiles, impact energy is focused on small regions and perforation can occur at much lower forces than more blunt projectiles. In Figure 4.8, the MLC target was perforated by a 30° nose projectile at a rate of 121m/s. Due to perforation by this geometry, cup-like depressions are beginning to occur throughout the microstructure. As impact energy becomes less centralized, the cup-like depressions will begin to grow into more pronounced dimples. This process can be observed in Figure 4.9. This target was subjected to perforation by a 90° nose projectile at a rate of 121m/s. In this micrograph, the small depressions have grown into dimples and have spread throughout the microstructure. In Figure 4.10, it is easily noticed that the cup-like depressions has undergone a transformation and have become dimples. This target was perforated by a 180° nose projectile at a rate of 125m/s. Based on the fracture surfaces observed for these targets, it can be stated that increasing projectile nose angle promotes the formation of more ductile deformation, via tensile tearing, within the fracture surfaces of the Ti/Al MLC targets.

To quantify the observation that ductility increases within increasing projectile apex angle, the image processing analysis software ImageJ was used. ImageJ was developed by the National Institutes of Health and is an open source code which is freely available in the public domain. ImageJ analysis was applied to the images shown in Figures 4.7-4.10 (as shown by

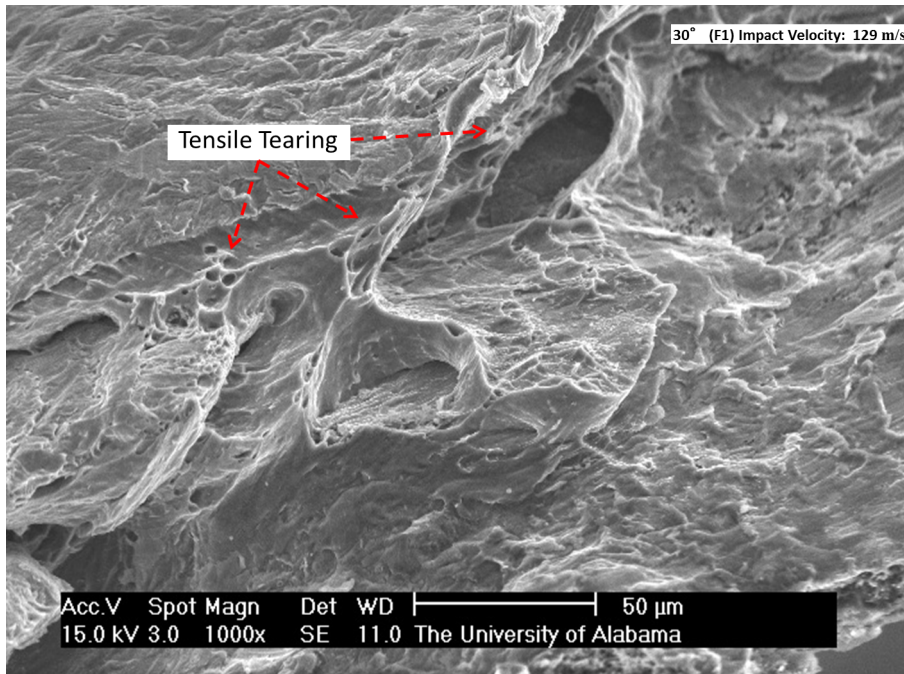


Fig. 4.7. 3.20cm x 3.20cm MLC (Sample F1)
Subjected to Perforation by a 30° Projectile at 129m/s

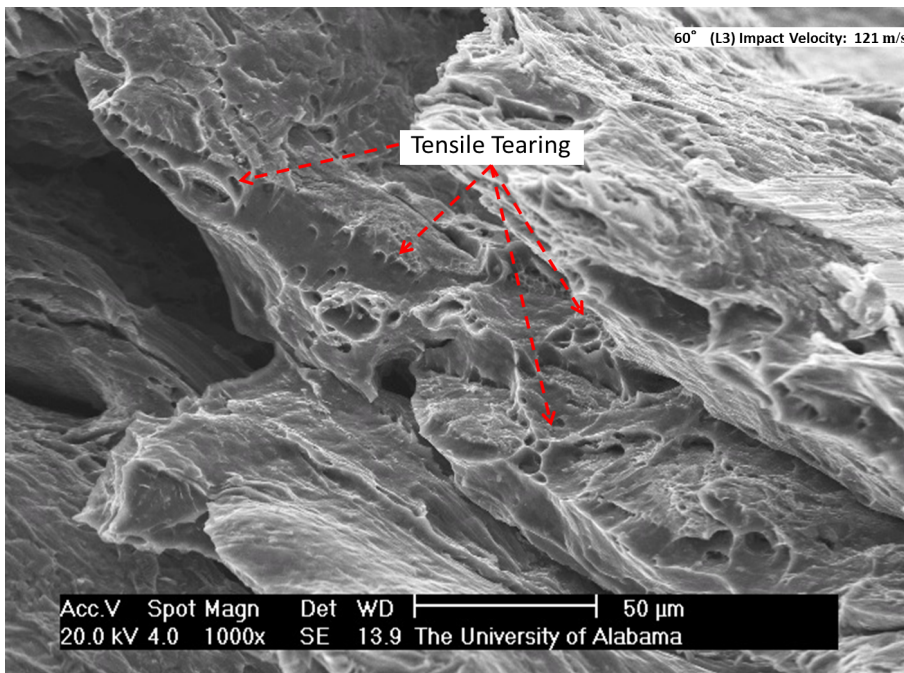


Fig. 4.8. 2.54cm x 2.54cm MLC (Sample L3)
Subjected to Perforation by a 60° Projectile at 121m/s

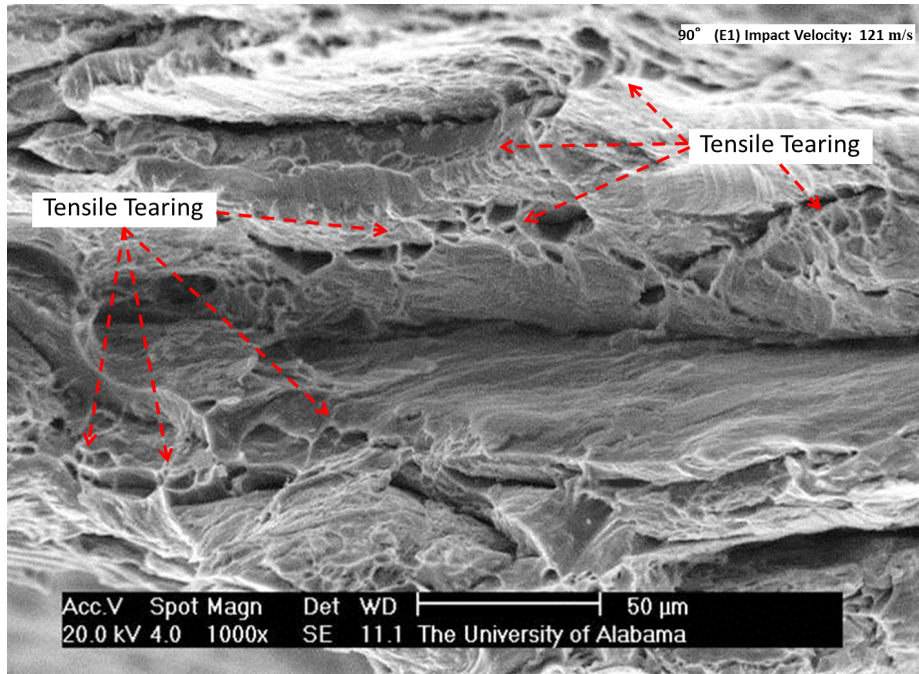


Fig. 4.9. 3.20cm x 3.20cm MLC (Sample E1)
 Subjected to Perforation by a 90° Projectile at 121m/s

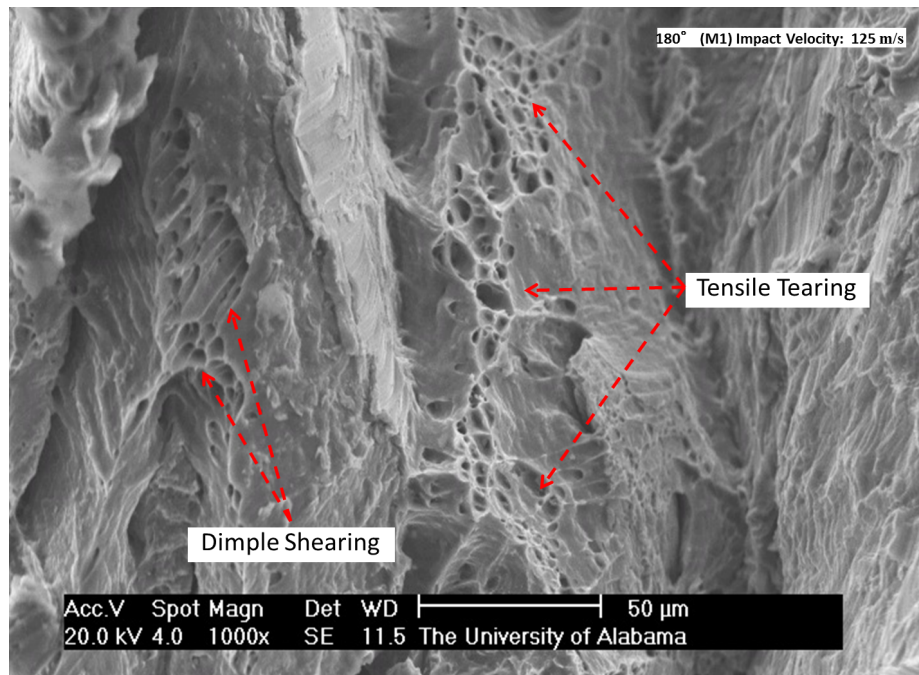


Fig. 4.10. 2.54cm x 2.54cm MLC (Sample M1)
 Subjected to Perforation by a 180° Projectile at 125m/s

by Figures 4.11-4.14). These figures are representative images to illustrate how the ImageJ software was utilized. To quantify the amount of observed ductile deformation, the procedure (shown in Figures 4.11-4.14) was applied to four regions (all varying by 90°) and the average dimple rupture percentages were determined. The results from the ImageJ analysis were reported in Table 4.1 and Figure 4.15. The amount of regions classified by dimple rupture increased from 5.55±0.786% for the 30° projectile nose to 22.1±2.05% for the 180° nose. This table confirms that ductile deformation increases as projectile apex angle decreases. Figure 4.15 illustrates this observed trend.

Throughout the microstructure of a ductile material, such as Ti/Al MLCs, it is quite possible to notice the presence of cleavage-like failure. According to ASM Handbook Volume 12, shear-band formation can occur within the fracture surfaces of ductile materials, such as Ti-6Al-4V. This can result in small, partially formed dimples on the shear-band portion of the fracture surface [30]. An example of this can be seen in Figures 4.16 and 4.17. These shear band regions can tend to be misleading because they often give the perception of cleavage failure.

4.3.3 Dissipated Kinetic Energy Calculations

Energy dissipation has a role in determining which failure mode becomes dominant. This article provides examples that convincingly display the increased presence of dimple rupture as impact velocity decreases. A similar trend is observed in energy dissipation. As energy decreases, dimple rupture increases. The amount of dissipated energy (E_K) can be calculated by multiplying 0.5 to the difference of impact and residual velocities squared (as seen by Eq. 4.2) [31].

$$E_K = \frac{1}{2} m_P (V_o^2 - V_R^2) \quad (4.2)$$

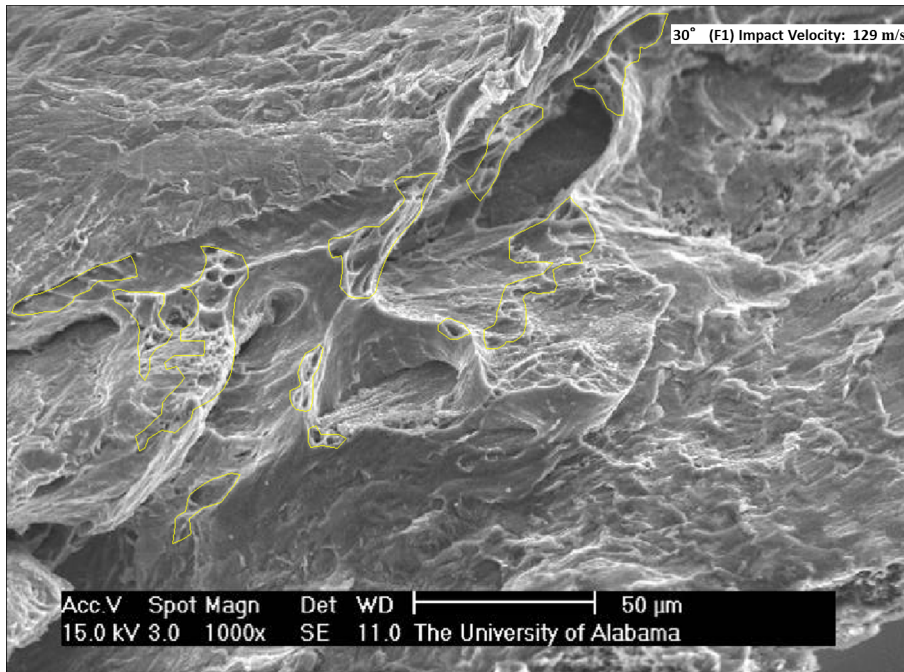


Fig. 4.11. ImageJ Analysis of 3.20cm x 3.20cm MLC (Sample F1) Subjected to Perforation by a 30° Projectile at 129m/s

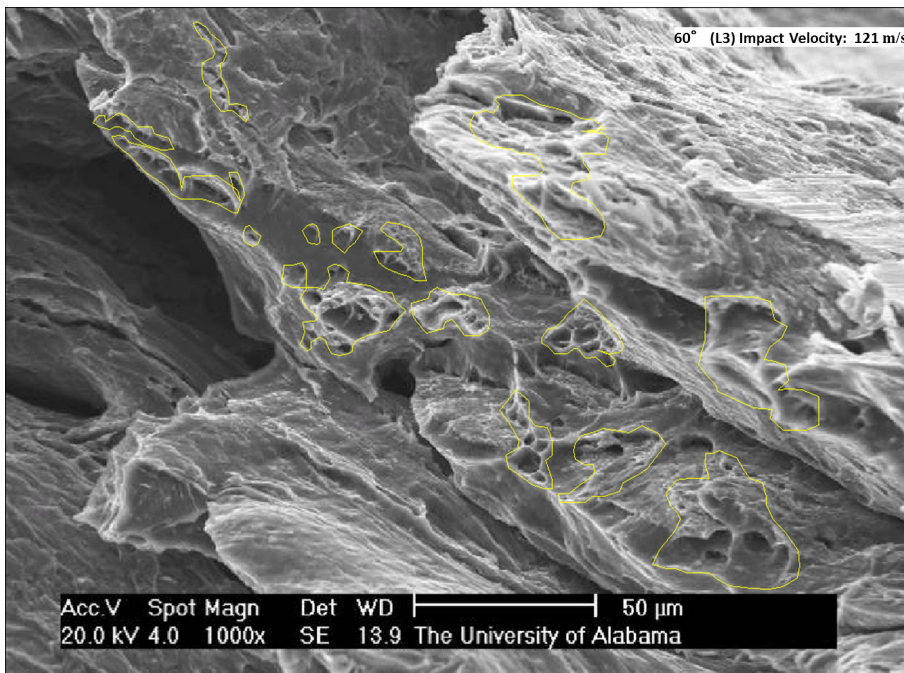


Fig. 4.12. ImageJ Analysis of 2.54cm x 2.54cm MLC (Sample L3) Subjected to Perforation by a 60° Projectile at 121m/s

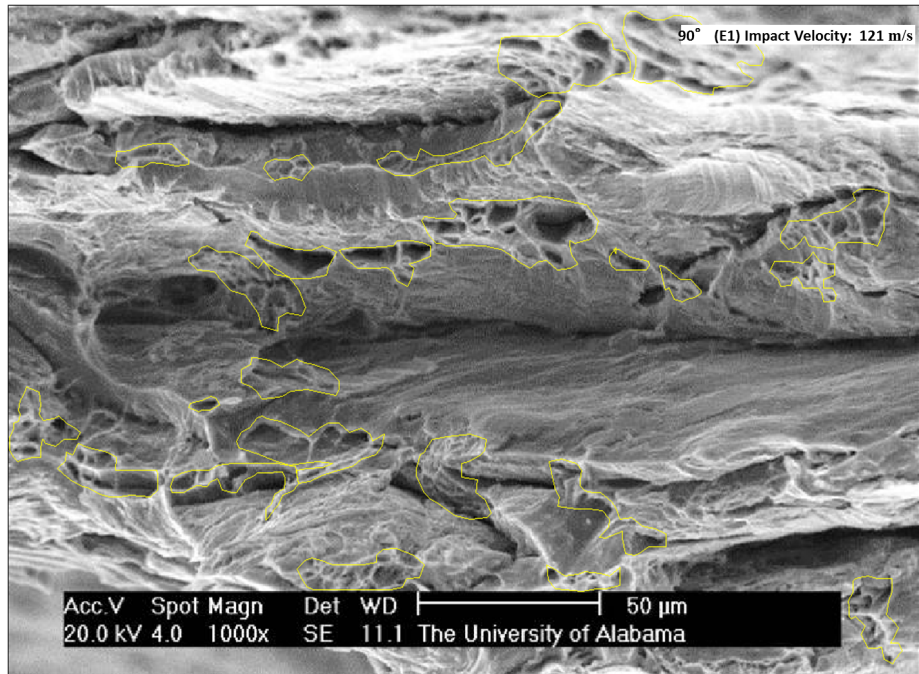


Fig. 4.13. ImageJ Analysis of 3.20cm x 3.20cm MLC (Sample E1) Subjected to Perforation by a 90° Projectile at 121m/s

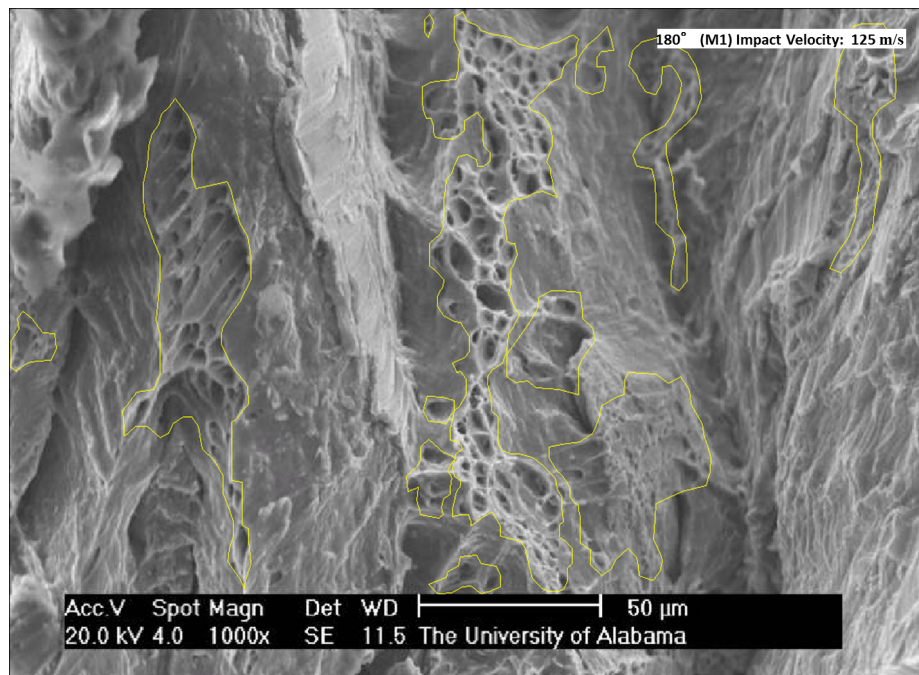


Fig. 4.14. ImageJ Analysis of 2.54cm x 2.54cm MLC (Sample M1) Subjected to Perforation by a 180° Projectile at 125m/s

Table 4.1. Projectile Apex Angle vs. Dimple Rupture Deformation for Ti/Al MLC Targets

Projectile Apex Angle	Dimple Rupture Percentage
180°	22.1±2.05
90°	11.1±1.22
60°	10.2±1.38
30°	5.55±0.786

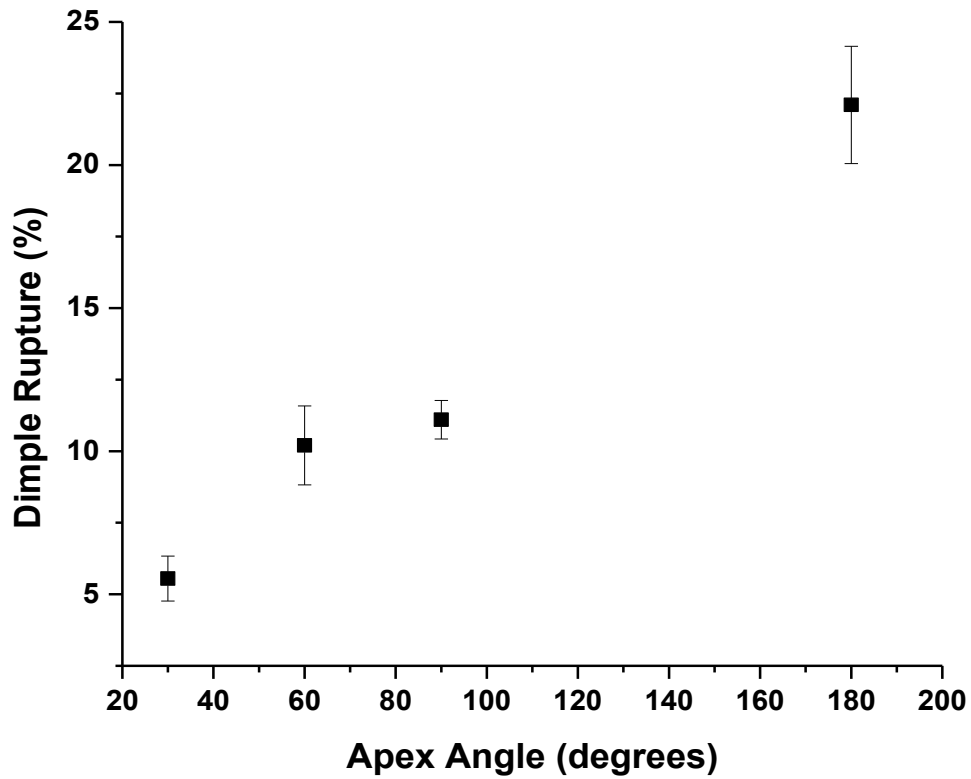


Fig. 4.15. Dimple Rupture vs. Apex Angle Graph of Table 4.1

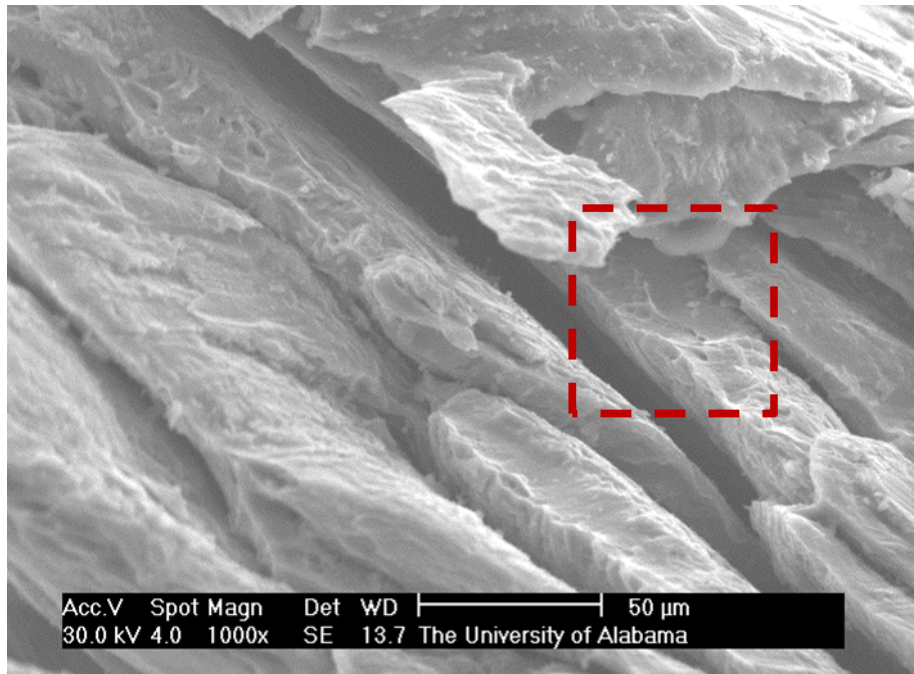


Fig. 4.16. 3.20cm x 3.20cm MLC (Sample F1)
Subjected to Perforation by a 30° Projectile at 129m/s

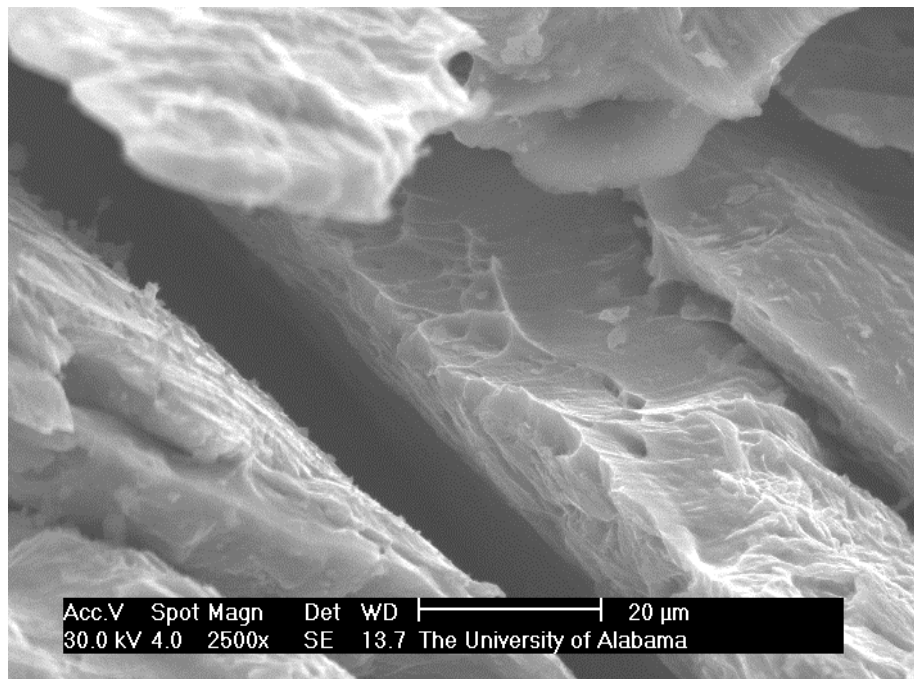


Fig. 4.17. Higher Magnification of Region Denoted by Boxed
Region in Fig. 4.16

Where, in terms of the projectile, energy is E_K , mass is m_P , impact velocity is V_o , and residual velocity is V_R [31]. The influence of energy dissipation can be observed in Figures 4.7 and 4.10. Figure 4.7 was perforated by a 30° projectile apex that had an impact velocity of 129m/s and a residual velocity of 108m/s while Figure 4.10 was perforated by a 180° projectile apex which had an impact velocity of 125m/s and a residual velocity of 113m/s. Although both samples are held at the same impact velocity, the amount of energy that was dissipated through the samples are significantly different. Figure 4.7 was subjected to 36.2J of energy while Figure 4.10 was subjected to 20.8J of energy. Due to the significant decrease in energy, in Figure 4.10, the amount of dimple rupture was significantly higher than in Figure 4.7.

4.3.4 Composition Analysis of Fracture Surfaces

Figure 4.18 shows the SEM secondary election image for the target perforated with 30° projectile at an impact velocity of 227m/s. The corresponding EDS profile, shown in Figure 4.19, is an area analysis of Figure 4.18. Figure 4.20 shows higher magnification images of Figure 4.18. Figure 4.20a is the secondary election (SE) image and Figure 4.20b is the back-scattered electron (BSE) image. In Figure 4.20b, the darker contrast regions are aluminum and the lighter contrast is titanium. This shows that more cup/cone regions occur in the aluminum. Figure 4.21 shows the region which was selected for compositional mapping as depicted in Figure 4.22. This confirms that the area with more cup/cone regions was aluminum.

Both titanium and aluminum have tendencies of ductile materials and can often portray dimpling [24,32-37]. Therefore, it was expected that both the Ti and Al, used in this study, would exhibit dimpling (as shown in Figures 4.23 and 4.24). In Figure 4.23, characteristic dimpling is observed throughout the spall region of the Ti6Al4V specimen. The presence of

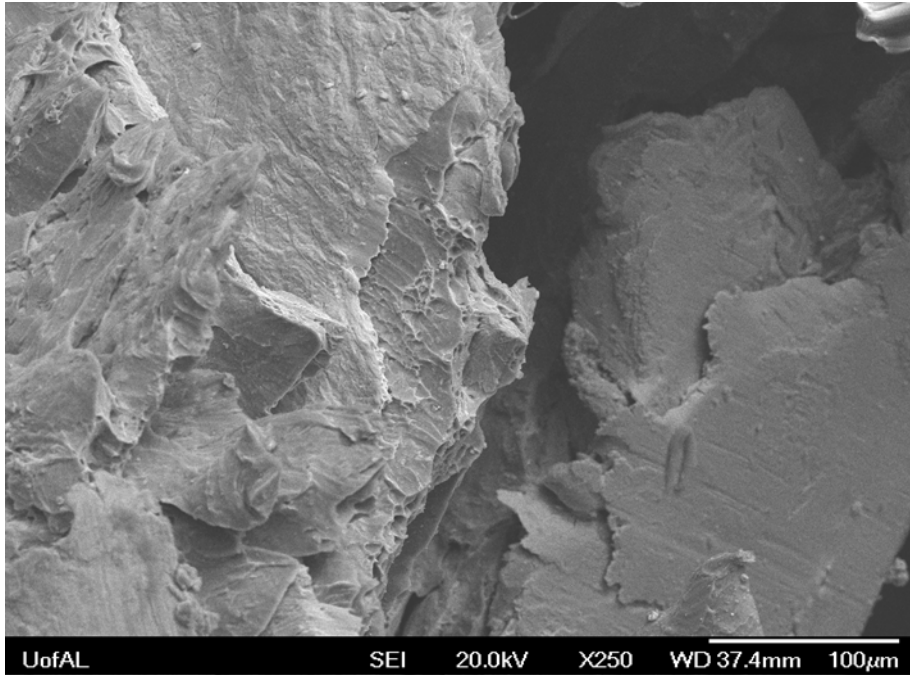


Fig. 4.18. SEM Secondary Electron Image of 2.54cm x 2.54cm Target Perforated by a 30° Projectile at an Impact Velocity of 227m/s

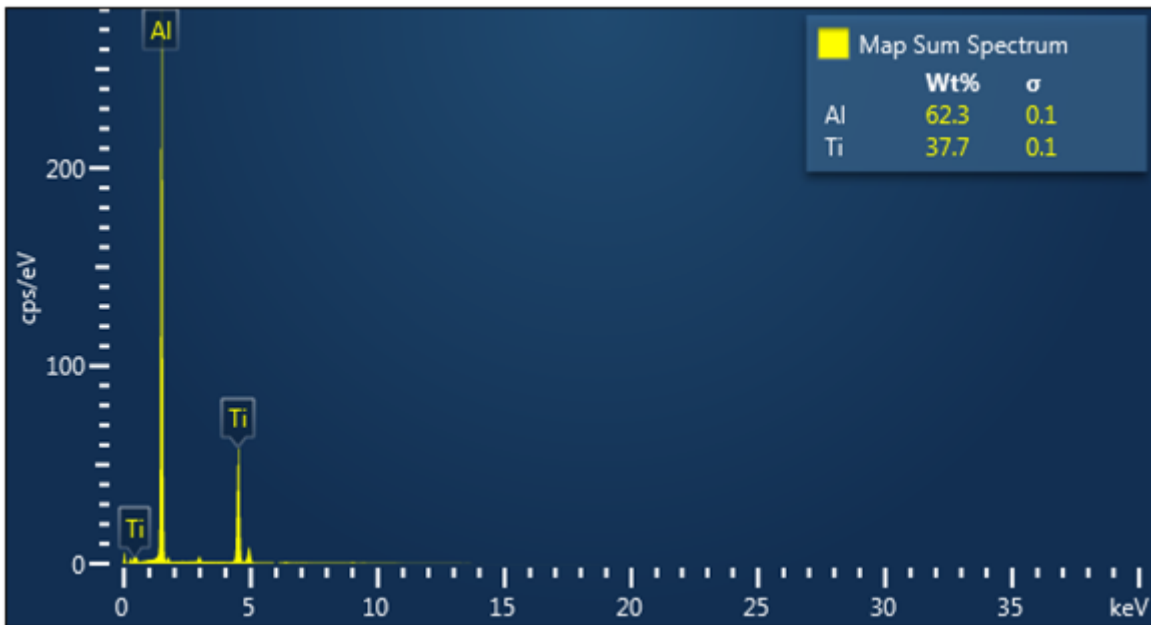


Fig. 4.19. SEM EDS Profile for Region Shown in Fig. 4.18

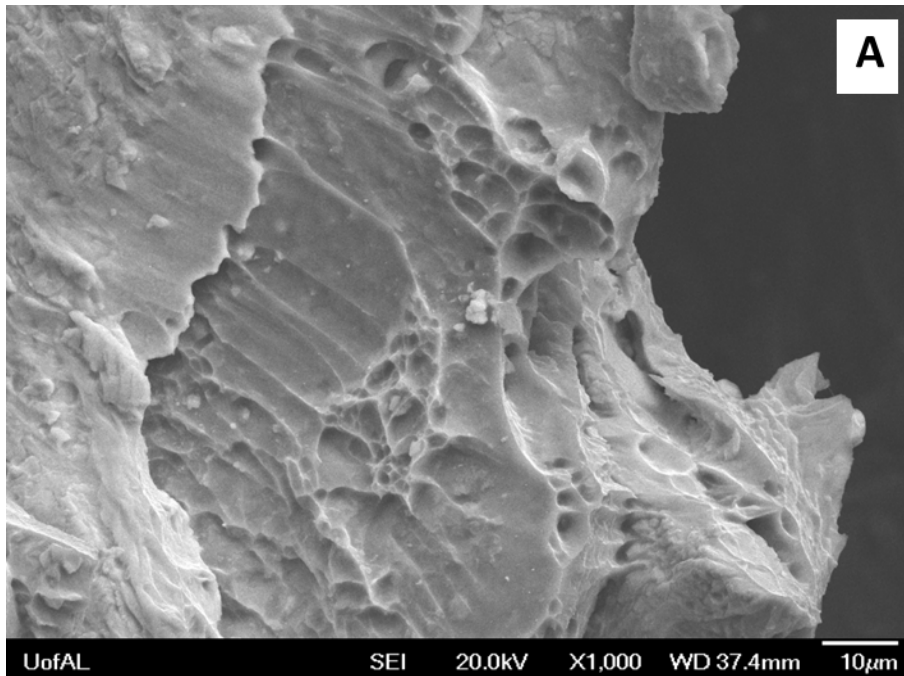


Fig. 4.20. Higher Magnification of Image Shown in Fig. 4.18
(A) Secondary Electron Image; (B) Back-scattered Electron Image

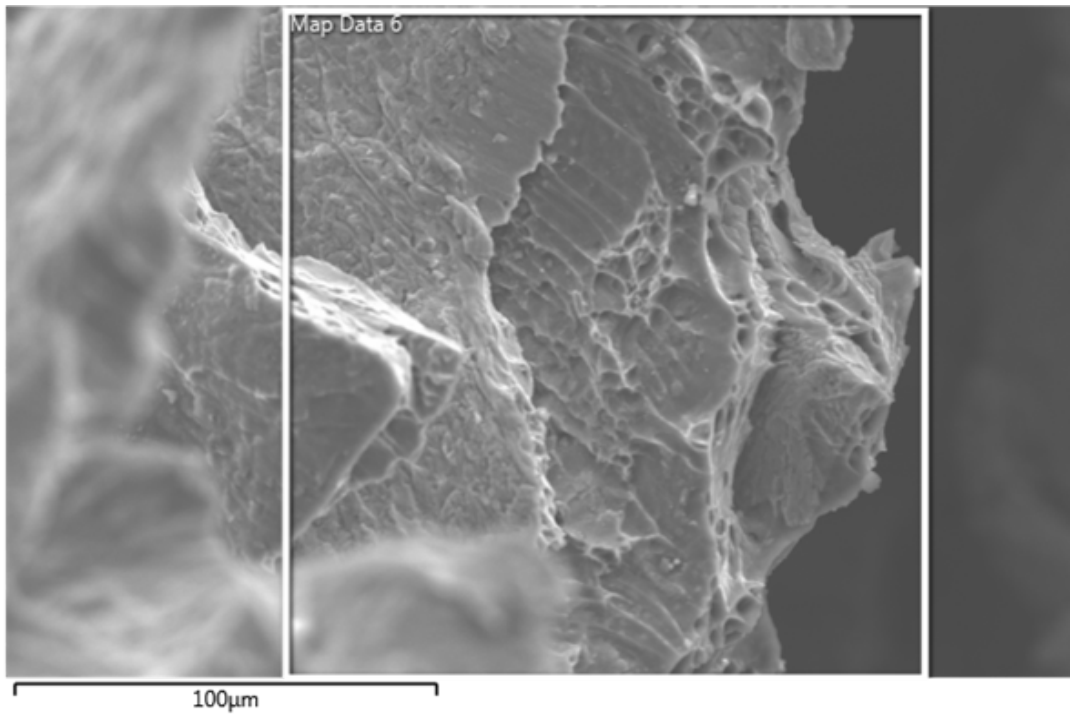


Fig. 4.21. Region Showing Where Compositional Mapping was Performed

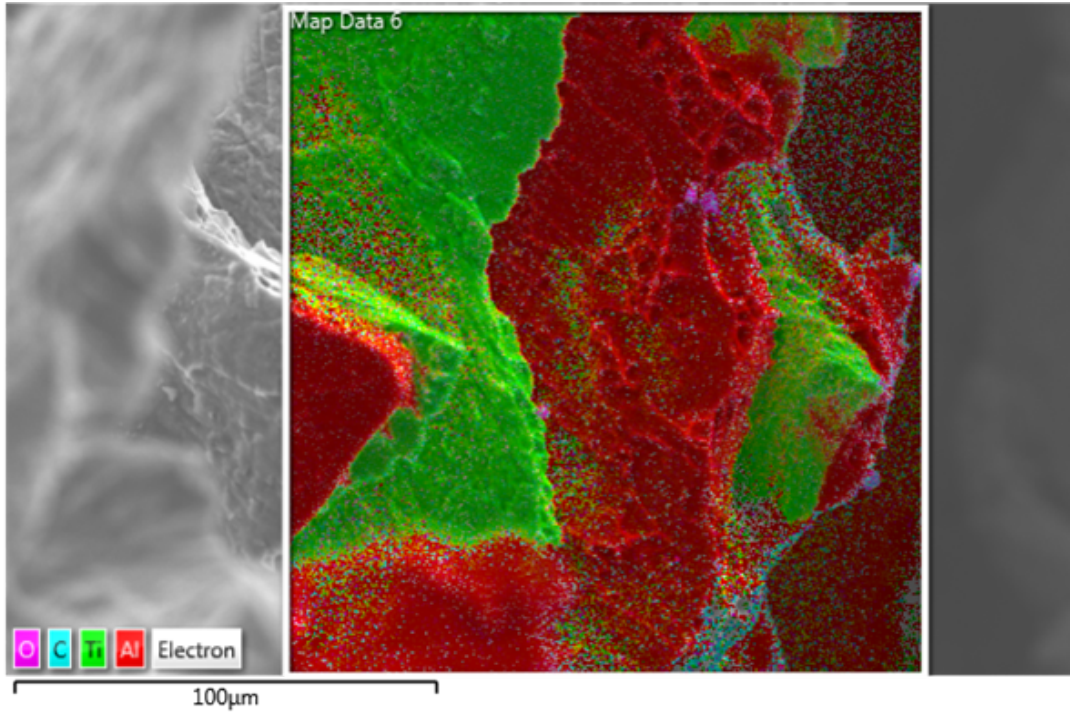


Fig. 4.22. Compositional Map of Region Shown in Fig. 4.21. The Green Depicts Titanium whereas the Red Depicts Aluminum

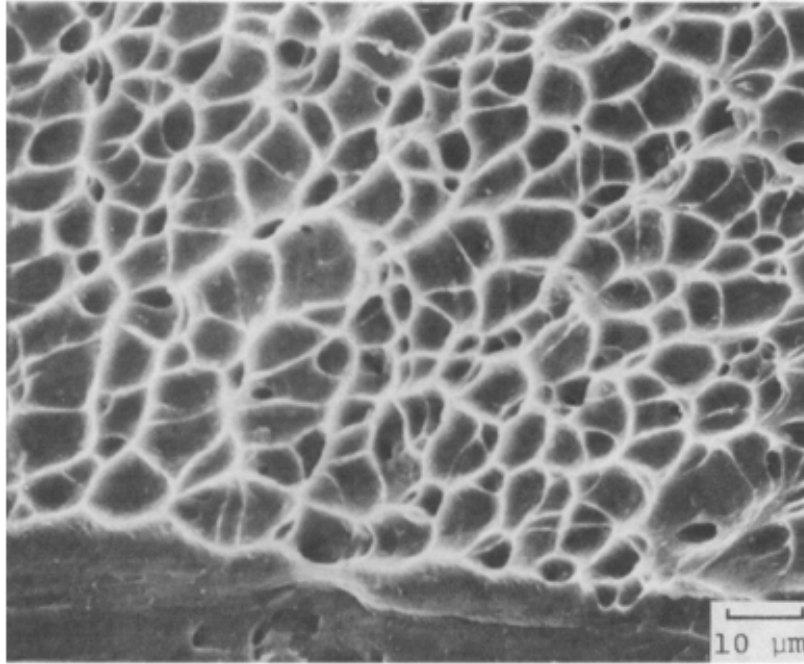


Fig. 4.23. SEM Micrograph of the Spall Surface in a Ti6Al4V Specimen that was Exposed to Perforation Testing. This image was Taken From Grebe et al. [24].

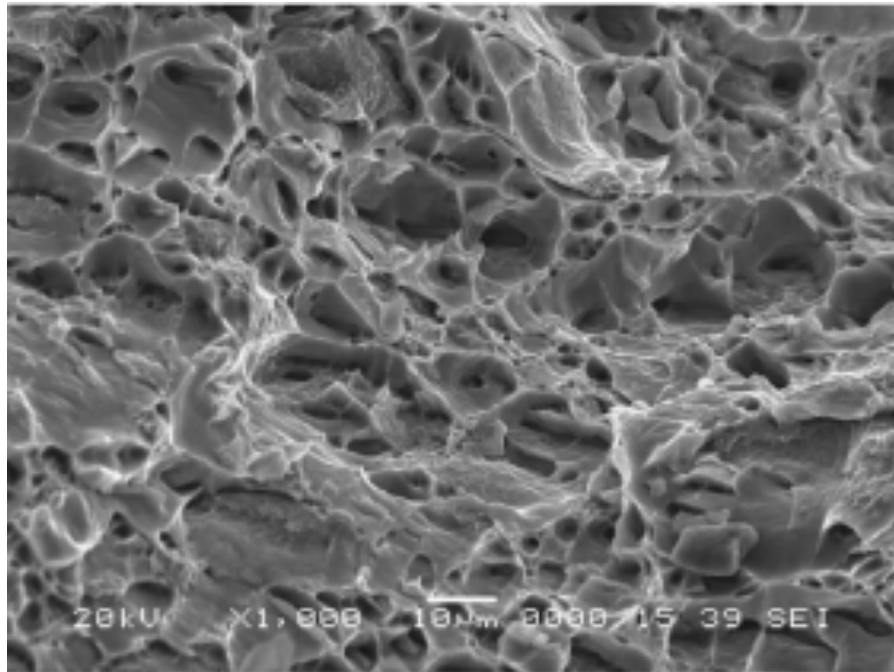


Fig. 4.24. SEM Micrograph of AA6016-T4 Aluminum Specimen that was Exposed to Tensile Testing. This image was Taken From Thuillier et al. [37].

well-defined dimples indicate that material has high amounts of ductility within its microstructure [24]. Figure 4.24 is a 6016-T4 aluminum alloy that was subjected to tensile testing. In this figure, high ductility (via dimpling) can be easily observed throughout the microstructure [37].

Despite the ductile nature of Ti, the extent of dimpling observed in the literature for Ti alloys [24] was not observed during this study. The lack of dimpling within the Ti layers, within the current study, is believed to be due to the excessive amount of strain hardening that was present during this experiment. Table 4.2 shows that the amount of plastic strain was 4.0 in the current study. The following equations (Eq. 4.2-4.4) were used to calculate layer thickness, total reduction, and plastic strain which is reported in Table 4.2. [38].

$$t = \frac{t_o}{2^{n+1}} \quad (4.2)$$

$$R_t = 1 - \frac{t}{t_o} \quad (4.3)$$

$$\varepsilon = \left[\frac{2}{\sqrt{3}} \ln \left(\frac{1}{2} \right) \right] * (n + 1) = 0.8(n + 1) \quad (4.4)$$

where t is the final thickness, t_o is the initial thickness, R_t is the total reduction, ε is plastic strain, and n is number of ARB cycles.

Strain hardening has been known to add stored energy and also reduce dimpling. This is because strain hardening influences hardness. Therefore, ductility (as indicated by dimpling) will decrease as cold working increases [39]. Due to the differences in crystal structure between Al (FCC) and Ti (HCP), it was predicted that the Al layers would exhibit more ductility throughout the fracture surfaces of the perforated ARB-processed Ti/Al MLCs. As shown in Figures 4.21 and 4.22, this hypothesis was proven to be accurate.

Table 4.2. Measured Layer Thickness, Total Reduction and Plastic Strain for Ti/Al MLC Specimens Subjected to 4 ARB Cycles. This Table was Adapted from Work From Zhang [38]

Element	Initial Thickness (t_0)	Final Thickness (t)	Total Reduction (R_t)	Plastic Strain (ϵ)
Titanium	22.39 μm	0.700 μm	97.01%	4.0
Aluminum	19.13 μm	0.598 μm	96.88%	4.0
Ti/Al Average	20.76 μm	22.39 μm	96.88%	4.0

4.4 Conclusions

This article presents data that explains the change in dominating failure modes as projectile impact velocity and apex angle are varied within ARB processed Ti/Al MLCs. After a thorough SEM evaluation it is evident that failure modes are directly affected by varying ballistic parameters such as projectile impact velocity and apex angle. The presence of ductile deformation is easily observed in Ti/Al MLCs through the manipulation of either impact velocity or apex angle. As impact velocity decreased, the observed failure mode, dimple rupture (via tensile tearing), became more dominant. As projectile apex angle increased (became more blunt), dimple rupture was more dominant as evident from the increased dimpling in the fracture surfaces. Compositional mapping showed that dimpling occurs primarily within the aluminum rich regions of the fracture surfaces.

4.5 References

- [1] E. S. C. Chin, "Army focused research team on functionally graded armor composites," *Materials Science and Engineering: A* 259 (1999) 155-161.
- [2] H. L. Gower, D. S. Cronin and A. Plumtree, "Ballistic impact response of laminated composite panels," *International Journal of Impact Engineering* 35 (2008) 1000-1008.
- [3] A. Patselov, B. Greenberg, S. Gladkovskii, R. Lavrikov and E. Borodin, "Layered Metal-intermetallic Composites in Ti-Al System: Strength Under Static and Dynamic Load," *AASRI Procedia* 3 (2012) 107-112.
- [4] A. Rohatgi, D. J. Harach, K. S. Vecchio and K. P. Harvey, "Resistance-curve and fracture behavior of Ti-Al₃Ti metallic-intermetallic laminate (MIL) composites," *Acta Materialia* 51 (2003) 2933-2957.
- [5] K. S. Kumar and M. S. DiPietro, "Ballistic penetration response of intermetallic matrix composites," *Scripta Metallurgica et Materialia* 32 (1995) 793-798.
- [6] G. P. Chaudhari and V. Acoff, "Cold roll bonding of multi-layered bi-metal laminate composites," *Composites Science and Technology* 69 (2009) 1667-1675.
- [7] J.-G. Luo and V. L. Acoff, "Processing gamma-based TiAl sheet materials by cyclic cold roll bonding and annealing of elemental titanium and aluminum foils," *Materials Science and Engineering: A* 433 (2006) 334-342.
- [8] R. Zhang and V. L. Acoff, "Processing sheet materials by accumulative roll bonding and reaction annealing from Ti/Al/Nb elemental foils," *Materials Science and Engineering: A* 463 (2007) 67-73.
- [9] G. P. Chaudhari, K. Serin and V. L. Acoff, "Processing Ultrafine Grained Composites of Elemental Titanium and Aluminium by Severe Plastic Deformation," in Ultrafine Grained Materials III, edited by Y. T. Zhu, T. G. Langdon, R. Z. Valiev, S. L. Semiatin, D. H. Shin and T. C. Lowe (TMS, 2004).
- [10] G. P. Chaudhari and V. L. Acoff, "Titanium aluminide sheets made using roll bonding and reaction annealing," *Intermetallics* 18 (2010) 472-478.
- [11] J.-G. Luo and V. L. Acoff, "Using cold roll bonding and annealing to process Ti/Al multi-layered composites from elemental foils," *Materials Science and Engineering: A* 379 (2004) 164-172.
- [12] N. Tsuji, Y. Saito, S. H. Lee and Y. Minamino, "ARB (Accumulative Roll-Bonding) and other new Techniques to Produce Bulk Ultrafine Grained Materials," *Advanced Engineering Materials* 5 (2003) 338-344.

- [13] Y. Saito, H. Utsunomiya, N. Tsuji and T. Sakai, "Novel ultra-high straining process for bulk materials—development of the accumulative roll-bonding (ARB) process," *Acta Materialia* 47 (1999) 579-583.
- [14] T. Hausöl, V. Maier, C. W. Schmidt, M. Winkler, H. W. Höppel and M. Göken, "Tailoring Materials Properties by Accumulative Roll Bonding," *Advanced Engineering Materials* 12 (2010) 740-746.
- [15] F. Yan and H. Zhang, "Evaluation of Stored Energy from Microstructure of Multi-component Nanostructured Cu," *Journal of Materials Science & Technology* 28 (2012) 289-293.
- [16] M. Meyers and K. Chawla, Mechanical Behavior of Materials, 2nd edition (Cambridge University Press, New York, 2009).
- [17] V. Kerlins and A. Phillips, "Modes of Fracture," *ASM Handbook* 12 (1987) 12-71.
- [18] S. Rizal and H. Homma, "Dimple fracture under short pulse loading," *International Journal of Impact Engineering* 24 (2000) 69-83.
- [19] A. R. Boccaccini, R. D. Rawlings and I. Dlouhý, "Reliability of the chevron-notch technique for fracture toughness determination in glass," *Materials Science and Engineering: A* 347 (2003) 102-108.
- [20] G. Hütter, L. Zybelle and M. Kuna, "Micromechanical Modeling of Crack Propagation with Competing Ductile and Cleavage Failure," *Procedia Materials Science* 3 (2014) 428-433.
- [21] A. J. McEvily, Metal Failures, 2nd edition (Wiley, 2013).
- [22] R. L. Woodward, "The interrelation of failure modes observed in the penetration of metallic targets," *International Journal of Impact Engineering* 2 (1984) 121-129.
- [23] X. Teng and T. Wierzbicki, "Numerical study on crack propagation in high velocity perforation," *Computers & Structures* 83 (2005) 989-1004.
- [24] H. A. Grebe, H.-R. Pak and M. Meyers, "Adiabatic shear localization in titanium and Ti-6 pct Al-4 pct V alloy," *Metallurgical Transactions A* 16 (1985) 761-775.
- [25] H. N. Krishna Teja Palleti, S. Gurusamy, S. Kumar, R. Soni, B. John, R. Vaidya, A. Bhoge and N. K. Naik, "Ballistic impact performance of metallic targets," *Materials & Design* 39 (2012) 253-263.
- [26] G. Balaganesan, R. Velmurugan, M. Srinivasan, N. K. Gupta and K. Kanny, "Energy absorption and ballistic limit of nanocomposite laminates subjected to impact loading," *International Journal of Impact Engineering* 74 (2014) 57-66.

- [27] J. M. Conway, A. R. Ortiz, S. E. Jones, V. L. Acoff and X. Bu, Perforation Testing of a Titanium Alloy Target Using Hardened 4340 Steel Projectiles, in "Pressure Vessels & Piping Division" (ASME, Bellevue, WA, 2010) p. 1-6.
- [28] E. W. Billington and A. Tate, The Physics of Deformation and Flow, 1st edition (McGraw-Hill International Book Co., New York, 1981).
- [29] N. K. Gupta, M. A. Iqbal and G. S. Sekhon, "Effect of projectile nose shape, impact velocity and target thickness on the deformation behavior of layered plates," *International Journal of Impact Engineering* 35 (2008) 37-60.
- [30] K. Mills, J. R. Davis, J. D. Destefani, D. A. Dietrich, H. J. Frissell, G. M. Crankovic and D. M. Jenkins, eds., ASM Handbook Volume 12 Fractography (ASM International, Materials Park, OH, 1987).
- [31] Y. Lee, E. D. Wetzel and N. J. Wagner, "The ballistic impact characteristics of Kevlar® woven fabrics impregnated with a colloidal shear thickening fluid," *Journal of Materials Science* 38 (2003) 2825-2833.
- [32] G. T. Hahn and A. R. Rosenfield, "Metallurgical factors affecting fracture toughness of aluminum alloys," *Metallurgical Transactions A* 6 (1975) 653-668.
- [33] I. Kirman, "The relation between microstructure and toughness in 7075 aluminum alloy," *Metallurgical Transactions* 2 (1971) 1761-1770.
- [34] S.-c. Liao and J. Duffy, "Adiabatic shear bands in a Ti-6Al-4V titanium alloy," *Journal of the Mechanics and Physics of Solids* 46 (1998) 2201-2231.
- [35] A. L. Wingrove, "The influence of projectile geometry on adiabatic shear and target failure," *Metallurgical Transactions* 4 (1973) 1829-1833.
- [36] R. L. Woodward, "Metallographic features associated with the penetration of titanium alloy targets," *Metallurgical Transactions A* 10 (1979) 569-573.
- [37] S. Thuillier, E. Maire and M. Brunet, "Ductile damage in aluminium alloy thin sheets: Correlation between micro-tomography observations and mechanical modeling," *Materials Science and Engineering: A* 558 (2012) 217-225.
- [38] R. Zhang, Processing Titanium-Aluminum-Niobium Sheet Materials From Elemental Foils Using Cold Roll Bonding and Reaction Annealing, Master's, The University of Alabama, 2004.
- [39] M. Tajally, Z. Huda and H. H. Masjuki, "Effect of Cold Rolling on Bending and Tensile Behavior of 7075 Aluminum Alloy," *Journal of Applied Sciences* 9 (2009) 3888-3893.

CHAPTER 5

THE EFFECTS OF VARYING BALLISTIC PARAMETERS ON THE BALLISTIC LIMIT OF Ti/Al MULTILAYERED COMPOSITES

Abstract

Multilayered Composites (MLCs) processed using Accumulative Roll Bonding (ARB) were investigated as targets for perforation testing. The MLCs were comprised of alternating layers of titanium (Ti) and aluminum (Al) foils. Perforation testing was used to determine the ballistic limit of the Ti/Al MLCs. During perforation testing, the effects of varying ballistic parameters (e.g. impact velocity, apex angle, and target size) on the ballistic limit of the Ti/Al MLCs were investigated. It was observed that a connection exists between the variation of ballistic parameters and the estimated ballistic limit of ARB-processed Ti/Al MLCs.

5.1 Introduction

Impact testing is often used to determine dynamic properties, such as fracture toughness or ballistic limit, for a given material. Impact testing is commonly conducted via drop weight impact tests, Charpy impact tests, and ballistic tests. Impact tests, especially ballistic/high velocity-based, are vital for the continual advancement of structurally enhanced products. For example, within the Defense industry, there is a crucial necessity for structurally improved helmets that possess materials with the ability to mitigate ballistic issues (e.g. shock waves, blast protection, and impact resistance) [1,2]. To address these specialized needs, such as the development of military grade impact resistant equipment, a thorough understanding of high impact loading (as it relates to material-based responses) is critical.

In ballistic testing, it is essential to have a thorough understanding of the ballistic limit (V_{50}) and how it may change under particular conditions. According to Ferriter et al., due to the complexities of penetration processes, effective first principles derivations of limit velocity (V_L) have not been discovered. Due to the impact testing complexity, ballistic limit experiments tend to be expensive and often result in relatively small sample sizes [3]. As an attempt to find a reliable ballistic tolerance, estimated ballistic limits ($*V_{50}$) tests are often typically collected semiempirically.

Research, by Ferriter et al., describes methods to collecting estimated ballistic limits. One technique, the Jonas-Lambert Method, estimates ballistic limit through the utilization of both impact velocity (V_o) and residual velocity (V_R). The second technique, known as the Bisection Method, estimates ballistic limit by treating the V_o vs. V_R plot as a continuous function. Despite the Bisection Method being the less expensive perforation technique, neither technique has been identified as more optimal than the other [3]. In the Jonas-Lambert method,

measurements for both the V_o and V_R are required. This technique determines $*V_{50}$ by establishing a relationship between V_o and V_R . The benefit to this technique is its low number of required data points. Through merely collecting three full shots, where the sample is fully perforated, there is enough data to determine the unknown variables [3]. The estimated ballistic limit ($*V_{50}$), used in the current study, was collected via the Jonas-Lambert Method.

Research by Misesy provides fundamental information regarding the development of ballistic limit equations. According to Misesy, Limit Velocity (V_L) is determined from physical principles such as conservation laws and materials constitutive relations. This is because of the difficulty and complexity associated with the governing partial differential equations. By using physical principles, this introduces simplification which requires empirical determination of one or two constants [4].

A probabilistic approach is used to determine the Impact Velocity (V_o) and the Residual Velocity (V_R). This leads to the determination of the resulting critical velocity (ballistic limit, V_{50}). Ballistic limit is described as the impact velocity (V_o) at which there exists a 50% chance that failure, to a given target material, will occur via perforation. Previous research to determine the estimated ballistic limit ($*V_{50}$) have ranged from using graphical determination by observing the relationship between the striking velocity (V_o) of the projectile and its residual velocity (V_R) [4] to using semi-empirical ballistic limit equations [5]. For example, the work of prior researchers expressed ballistic limit equations (BLEs) in a form that relates critical particle diameter (d_c) with impact velocity, impact angle, particle density, and target parameters [6].

Material selection is a vital aspect to consider when discussing the topic of armor development. Proper material selection is essential, especially in the development of military

grade protective gear, because it is directly linked to the survivability of soldiers as well as the structural integrity of armored vehicles [7]. During the material selection process, factors such as weight, durability and resistivity are critical. In terms of weight, protective gear must be strong but light enough to ensure continual mobility [8,9]. Regarding durability, the engineered component must be able to withstand harsh physical environments (such as extreme weather conditions) [10]. Resistivity is a crucial element to consider in the material selection process. This is due to the high demands on military grade projective gear.

Military-based protective gear must be able to resist physical damage by projectiles traveling at high velocities. Prohibiting projectile perforation is heavily dependent on the material's physical and chemical properties. Therefore, chosen materials must be tough yet strong. For example, ideal candidates for impact resistant applications are typically materials that have a degree of impact resistivity and the ability to absorb kinetic energy [11]. By considering the aforementioned factors (weight, durability, and resistivity), engineers have made strides towards the development of mechanically strengthened products with increased ballistic limits [12]. Ballistic limit, V_{50} , (also known as stopping power) is a unit less measurement that describes a material's physical ability to hinder the perforation of incoming projectiles. Specifically, V_{50} is defined as the rate at which there is a 50% probability of total perforation for a given target material via a launched projectile [1,13].

Shock waves are unique phenomena that are generally associated with high amounts of heat or pressure. Shock waves are often produced by moving objects which are traveling faster than the speed of sound (e.g. bullets). In terms of materials science and engineering, a comprehensive understanding of shock waves is essential. Material properties, such as density, can be determined via a thorough analysis of shock wave propagations [14]. The strength of

shock waves are directly associated to distance from impact. In ballistic tests, the strength of associated shock waves significantly decreases as distance from impact increases. Furthermore, distance from impact also affects energy absorption. For a given material, energy absorption will increase as distance (or target area) increases, thus, confirming the existence of size effects [15]. This phenomenon provides logical reasoning to why ballistic limit data is usually directly proportional to target area.

Literature has provided data that proves there exists a correlation between the variation of ballistic parameters and ballistic limit [16]. In order to advance the development of mechanically enhanced metallic composites, such as MLCs, an understanding of the aforementioned relationship is critical. Therefore, the goal of this research is to determine the correlation between varying projectile parameters and ballistic limit in ARB-processed Ti/Al MLCs, which were subjected to perforation testing.

5.2 Experimental Procedure

5.2.1 Sample Preparation and Accumulative Roll Bonding (ARB)

In this experiment, thin sheets of commercially pure Ti and Al were used to process the MLC targets. Each sheet had a thickness of 75 μ m and an original area of 7.6cm x 7.6cm. The Ti and Al sheets were stacked in an alternating fashion to make a 21-layered composite that consisted of 11 sheets of Ti and 10 sheets of Al. These 21 sheets were fed into a rolling mill to produce 50% reduction in the first pass. After the initial pass the roll bonded Ti/Al composite was sectioned into two halves, re-stacked and sent through the rolling mill again. This was one ARB cycle. The ARB process was repeated for 4 ARB cycles. After subjecting to 4 ARB cycles, the final thickness of the Ti/Al MLC was approximately 1mm.

5.2.2 Impact Testing

The projectiles (7.8mm diameter; 50.8mm long; 14.9g) used in this study were 4340 steel hardened to a minimum Rockwell C Hardness number of 50. Each projectile was machined to projectile nose geometries of 30°, 60°, 90°, and 180° apex angles. Two different target sizes of ARB-processed Ti/Al MLCs were employed: 2.54cm x 2.54cm and 3.20cm x 3.20cm. The perforation testing apparatus consisted of a smooth bore barrel, gun breach, firing solenoid, target fixture, lasers, chronographs, and a sand trap. Upon firing, the launched projectile passes through a set of impact and residual lasers. The velocities from these lasers were then used to calculate how much energy the MLC target absorbed during perforation. This information was used to determine the ballistic limit (or stopping power) of the ARB-processed Ti/Al MLC targets.

5.3 Results and Discussion

5.3.1 Ballistic Limit Data

Figure 5.1 shows the 2.54cm x 2.54cm target that was perforated by a projectile with an apex angle of 180°. The impact velocity was 125m/s. Figure 5.2 shows the 3.2cm x 3.2cm target, which was also perforated with 180° apex angle projectile. The impact velocity was 185m/s for this target. Figures 5.3 and 5.4 show the targets perforated by projectiles with a 30° apex angle for target sizes of 2.54cm x 2.54cm and 3.20cm x 3.20cm, respectively. The impact velocity for the smaller target was 227m/s compared to 181m/s for the larger target.

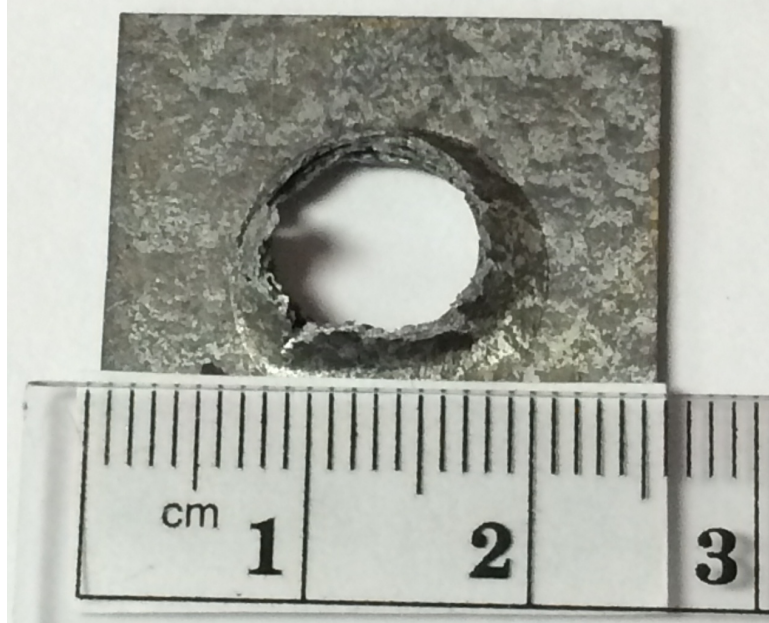


Fig. 5.1. 2.54cm x 2.54cm MLC (Sample M1)
Subjected to Perforation by a 180° Projectile at 125m/s

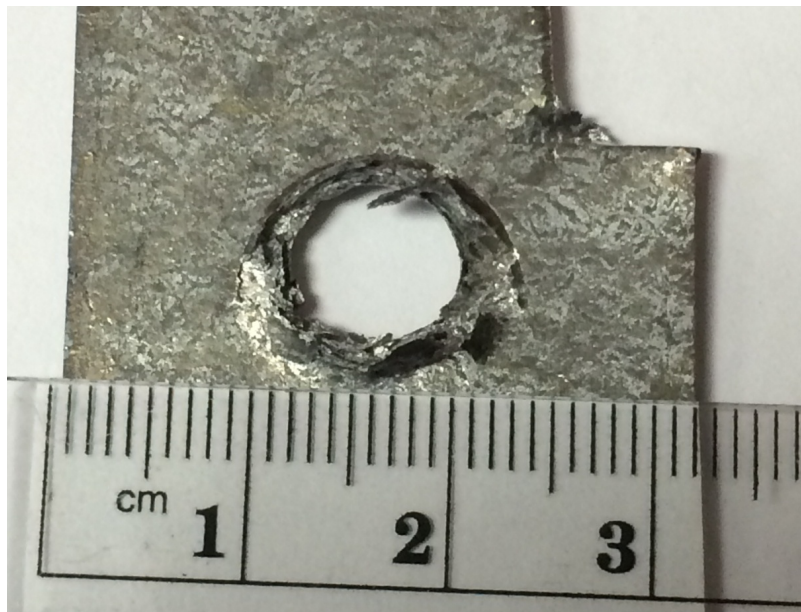


Fig. 5.2. 3.20cm x 3.20cm MLC (Sample G1)
Subjected to Perforation by a 180° Projectile at 185m/s

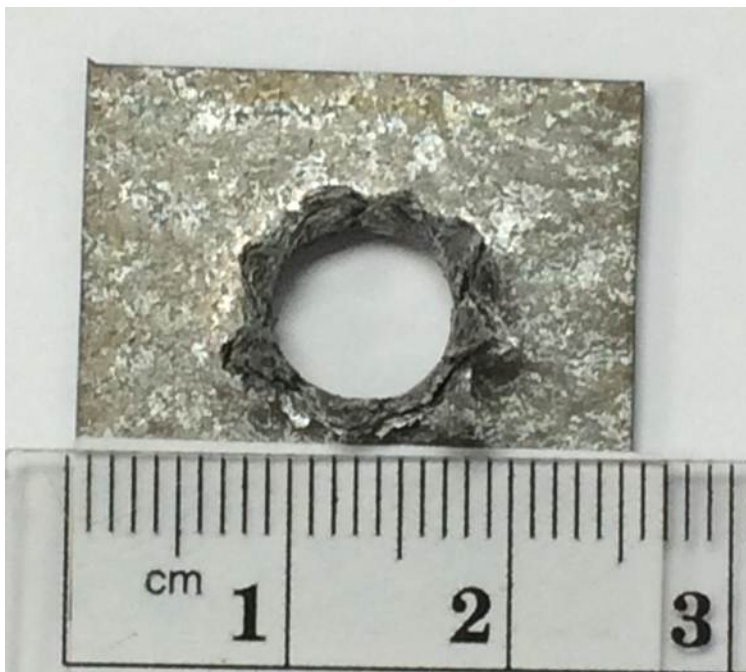


Fig. 5.3. 2.54cm x 2.54cm MLC (Sample M2)
Subjected to Perforation by a 30° Projectile at 227m/s

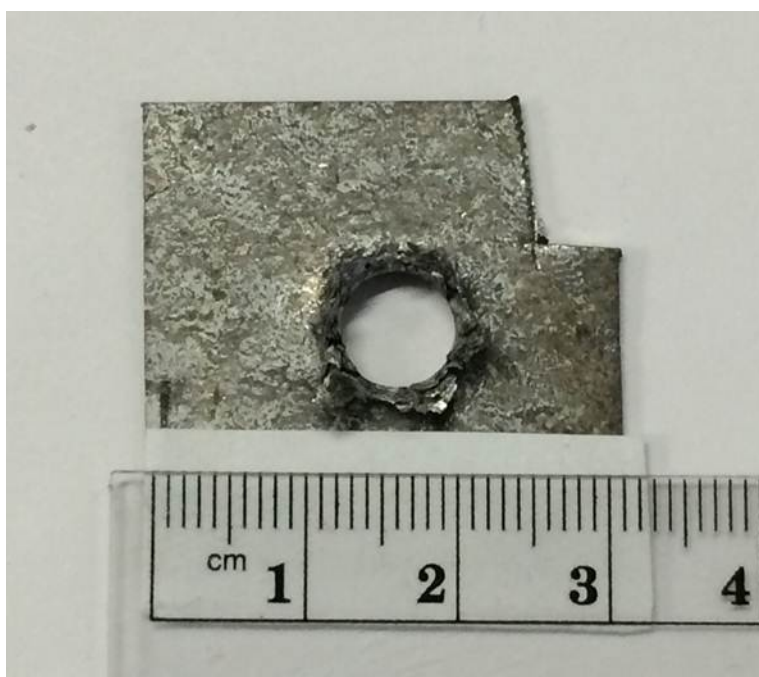


Fig. 5.4. 3.20cm x 3.20cm MLC (Sample J1)
Subjected to Perforation by a 30° Projectile at 181m/s

Upon completion of the ballistics testing, vital variables such as impact velocity (V_o) and residual velocity (V_R) were generated as reported in Tables 5.1 and 5.2 as well as in Figures 5.5 and 5.6. Impact and residual velocities were used to calculate the coefficient A (Eq. (5.1)) which was used to determine the estimated ballistic limit ($*V_{50}$). The semi-empirical coefficient A was determined through a set of summations as shown by Eqs. 5.2 and 5.3

$$A = \frac{-value (Numerator)}{+value (Denominator)} \quad (5.1)$$

$$A_{Numerator} = \left[\left(\frac{V_{R1} - V_{O1}}{V_{O1}^m} \right) + \left(\frac{V_{R2} - V_{O2}}{V_{O2}^m} \right) + \dots + \left(\frac{V_{Rn} - V_{On}}{V_{On}^m} \right) \right] = -value \quad (5.2)$$

$$A_{Denominator} = \left[\left(\frac{1}{V_{O1}^{2m}} \right) + \left(\frac{1}{V_{O2}^{2m}} \right) + \dots + \left(\frac{1}{V_{On}^{2m}} \right) \right] = +value \quad (5.3)$$

The numerator contains summations that involve mixture of impact velocities, residual velocities and an adjustment factor (m). All impact and residual velocities were collected experimentally but the adjustment factor, m, was held at 0.25. In the denominator, the only experimental data considered was the impact velocities. If there is only one result, then Eqs. 5.1-5.3 can be simplified as shown by Eq. 5.4.

$$A = \frac{-value (Numerator)}{+value (Denominator)} = \frac{\left(\frac{V_{R1} - V_{O1}}{V_{O1}^m} \right)}{\left(\frac{1}{V_{O1}^{2m}} \right)} = V_{O1}^m (V_{R1} - V_{O1}) \quad (5.4)$$

Table 5.1 Data Used to Calculate the Ballistic Limits for the 2.54cm x 2.54cm Targets

Specimen (Projectile Apex Angle)	Impact Velocity (V_o)	Residual Velocity (V_R)
N2 (180°)	160	142
N1 (180°)	130	120
N3 (180°)	129	119
M1 (180°)	125	113
No Sample (90°)	N/A	N/A
L2 (60°)	231	212
L1 (60°)	200	187
L3 (60°)	121	112
M2 (30°)	227	210

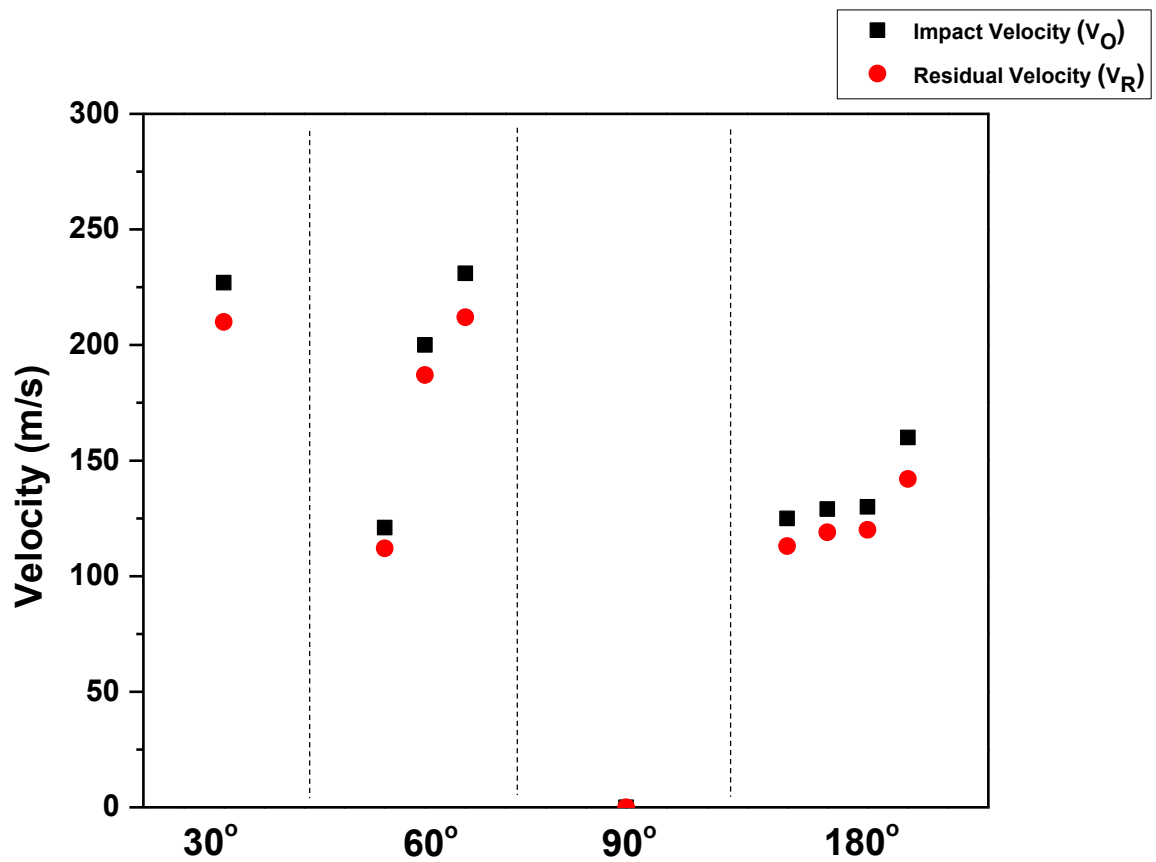


Fig. 5.5. Velocity vs. Projectile Apex Angle Chart for 2.54cm x 2.54cm Ti/Al ARB-Processed Targets

Table 5.2 Data Used to Calculate the Ballistic Limits for the 3.20cm x 3.20cm Targets

Specimen (Projectile Apex Angle)	Impact Velocity (V_o)	Residual Velocity (V_R)
G1 (180°)	185	173
I3 (90°)	213	203
J3 (90°)	203	190
I1 (90°)	160	151
I2 (90°)	134	122
E1 (90°)	120	109
H1 (60°)	170	160
H2 (60°)	156	145
J1 (30°)	181	167
J2 (30°)	153	139
F1 (30°)	129	108
F2 (30°)	104	79.8
E2 (30°)	95.1	71.0

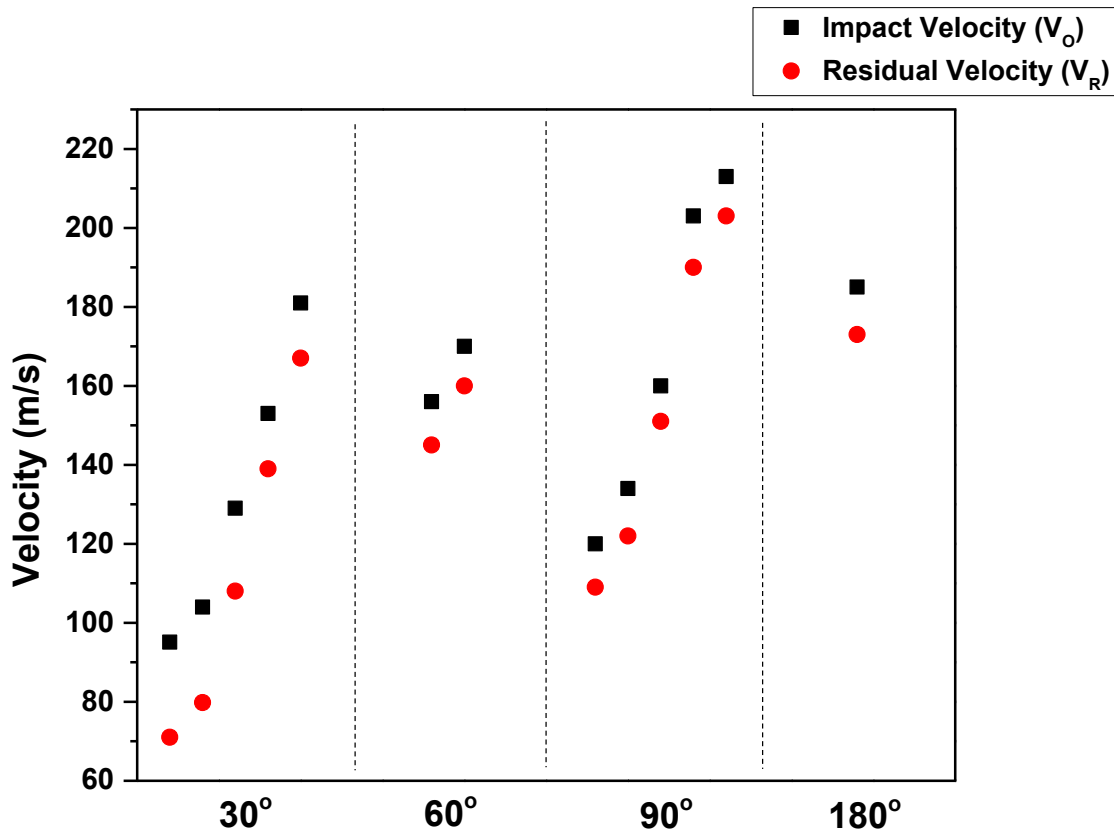


Fig. 5.6. Velocity vs. Projectile Apex Angle Chart for 3.20cm x 3.20cm Ti/Al ARB-Processed Targets

As depicted by Eq. 5.5, the overall value for A must be negative for the estimated ballistic limit ($*V_{50}$) to be a positive value.

$$*V_{50} = -A \left[\frac{1}{(m+1)} \right] \quad (5.5)$$

The estimated ballistic limit ($*V_{50}$) equations used in the current study applies probability theory and utilized Taylor series approximations to provide a probabilistic approach to determining $*V_{50}$. Using a probabilistic approach to determine $*V_{50}$ is documented in the literature [4]. In the current study, the equation used is one of the most simplistic methods to approaching ballistic limit estimations (as shown in Eqs. 5.6 and 5.7).

$$V_R = V_o + \frac{A}{V_o} \quad (5.6)$$

$$0 = *V_{50} + \frac{A}{*V_{50}} \quad (5.7)$$

From the above equations, the estimated ballistic limits for the two target sizes were determined as a function of projectile apex angle. This data is reported in Tables 5.3 and 5.4.

According to the literature [17], the relationship between residual velocity (V_R) and impact velocity (V_o) may be expressed as by Eq. 5.8:

$$V_R = \left[1 + \frac{\rho_t}{\rho_p} \left(\frac{D_q}{D_p} \right)^2 \frac{h_0}{L_0} \right]^{-1} \sqrt{(V_o^2 - V_{50}^2)} \quad (5.8)$$

Table 5.3. Estimated Ballistic Limits vs. Apex Angle data for 2.54cm x 2.54cm ARB-processed Ti/Al MLCs Targets

Projectile Apex Angle	Estimated Ballistic Limit (*V₅₀)
180°	19.8
90°	N/A
60°	22.3
30°	28.5

Table 5.4. Estimated Ballistic Limits vs. Apex Angle data for 3.20cm x 3.20cm ARB-processed Ti/Al MLCs Targets

Projectile Apex Angle	Estimated Ballistic Limit (*V₅₀)
180°	21.7
90°	18.8
60°	18.2
30°	28.4

Where V_R = Residual Velocity, V_o = Impact Velocity, V_{50} = Ballistic Limit, ρ_t = Target Density, ρ_p = Projectile Density, D_q = Projectile Diameter, D_p = Plug Diameter, h_o = Target Thickness, L_o = Original Length of Projectile. Previous researchers have shown that a connection exists between Eq. (5.8) and an equation similar to Eq. (5.6) used in the current study [17]. Thus, using a more simplistic approach (Eq. (5.6) and Eq. (5.7)) in the current study provides similar results to those for a more complex approach.

The impact velocity is important to determining, the V_{50} , but one of the most influential variables to consider is projectile apex angle. This is due to centralization of impact energy. A good example of geometry dependence would be if two projectiles, with different nose geometries, hit a material while traveling at similar velocities. Although both projectiles would have similar impact energies, the surface area of the incoming projectiles would be different. Varying projectile surface area will strongly affect the distribution of impact energy. This would lead to a change in failure mechanisms and could result in different failure rates for a given material. Therefore, due to the distribution of impact energy, projectile apex angle must be taken into account

Crack propagation, and eventually perforation is directly related to lack of energy dispersion. As such, one must consider the mechanics associated with the perforation of sharp and blunt projectiles. As projectile nose geometries approach 180° (blunt projectiles), impact energy becomes evenly distributed. As force is evenly distributed about a material, the amount of energy that can be absorbed by the target material increases. This is critical to target survivability because the ability to absorb energy directly influences the amount of stress that is needed to deform a material. The opposite is true for sharp-nose projectiles. Regarding sharp projectiles, force is localized and impact energy becomes focused on a centralized area. As impact energy is

locally focused, it becomes easier to exceed shear strength. This correlation is critical because the reduction of surface area (e.g. sharp-nose projectiles) effectively results in reduced ballistic limits for a given material. Generally speaking, the sharper the projectile, the less energy is required for perforation to occur.

To determine the influence of target size on estimated ballistic limits, two target sizes were used during this experiment. Upon analyzing the ballistic impact data, a unique ballistic-based trend was observed in the smaller targets. It was observed that estimated ballistic limit increased as projectile apex angle decreased (e.g. becomes sharper). While it was highly expected that the estimated ballistic limit would decrease, with increased force localization, the data exhibited a contradictory behavior (see Table 5.3). However, for the larger targets, the expected ballistic trend occurred. As shown in Table 5.4, the ballistic limit increased as projectile nose angle increased (e.g. becomes more blunt). From analyzing both target sizes, it is undeniable that target size plays a significant role in the observed ballistic limit.

Upon analyzing target variation, ballistic correlations were quickly observed as target sizes were changed. In the smaller targets, the ballistic limit behaved in an opposite manor from what was expected. In the larger targets, a more anticipated ballistic limit correlation was observed. It is believed that the observed ballistic limits were influenced by traveling shockwaves. Upon impact of rigid body projectiles, stress (or shock) waves are propagated throughout a material. When shockwaves reach a boundary, they then rebound with amplified tensile force [2,14]. Shockwave velocity can be easily influenced by either projectile mass or impact velocity. By merely increasing the MLC target area, traveling shockwaves are more easily absorbed and delayed from reaching the target boundaries [8]. Delaying this phenomenon is essential to influencing the absorption capability of a target material. By increasing target size,

more impact energy is absorbed and the tensile forces associated with traveling shockwaves are reduced [13,15].

In the current study, increasing the MLC target area by 25% resulted in a self-correction of ballistic limit trends, as shown in Table 5.3 and 5.4. This can be imagined conceptually through the assistance of Figures 5.1 and 5.2. Despite the relatively large hole size in Figure 5.1, the target area is 2.54cm x 2.54cm. In Figure 5.2, a similar perforation is observed, but the target size is 25% larger. This supports the aforementioned theory that increasing target area by 25% was enough to cause a shift in the observed ballistic limit as observed in Tables 5.3 and 5.4.

Systematic issues were noticed during the ballistic testing process. One issue was the inability to collect reliable impact data for the 2.54cm x 2.54cm MLC target that was perforated by a 90° projectile. Impact data, for this specimen, could not be recorded because the 90° projectile perforated the target at an obscure angle. Another issue was that there was no observed difference in the recorded estimated ballistic limits for the targets that were subjected to perforation by 30° projectiles. As shown in Tables 5.3 and 5.4, both the 2.54cm x 2.54cm and 3.20cm x 3.20cm MLC targets had a $*V_{50}$ of 28.5 and 28.4, respectively. The similarity in $*V_{50}$ is partially believed to be due to the steep pitch of the 30° projectile. Another issue, in part, is believed to be associated with the limitations of the Jonas-Lambert Method. According to Ferriter et al., the Jonas-Lambert Method does not thoroughly explain the behavior of the projectiles (which were used during perforation). Due to this limitation, it possible to have two projectiles with an identical V_o and different V_R [3].

5.3.2 Ballistic Limit Data Comparison

Compared to work by prior researchers [17], the present study had a similar series of controlled variables such as: projectile material, projectile nose geometries, and target material.

In terms of ballistic limits, the current study has shown that a strong correlation exists as projectile apex angle and target size are varied. The work by prior researchers employed a slightly different equation for determining the estimated ballistic limit. Compared to equation 5.6, two coefficients (A and B) were used instead of the one coefficient (A) used in the present work. In addition, the size of the projectiles used in the previous study was only 3g in mass compared to 14.9g used in the current study. The results for the previous work showed that the ballistic limit decreased as projectile nose geometries became sharper. All targets were 2.54cm x 2.54cm [17].

In this experiment, an inverse relationship for estimated ballistic limit vs. projectile apex angle was observed. This was only consistent for the smaller targets (as shown in Table 5.3). However, for the targets that were 25% larger, the estimated ballistic limit vs. projectile apex angle was similar to that reported by previous researchers [17]. Those trends, established from those results, resulted in a decrease in estimated ballistic limit as projectile apex angle became sharper. From this shift in estimated ballistic limit, one can see that target size has an influence on $*V_{50}$. This is supported by works from Diedrich and Stepka. According to Diedrich and Stepka, larger target area allow for more impact energy to be absorbed [15].

The ballistic limit values in the current study are much lower compared to those determined by previous researchers [17]. This can be attributed to the projectile mass effect. The mass of the projectile in the current study was approximately 5 times larger than that used by Conway, et al. [17]. This drastic increase in mass significantly increased the amount of momentum during ballistics testing. From a ballistic standpoint, an increase in momentum equates to a decrease in estimated ballistic limit.

5.4 Conclusions

From this study, it has been concluded that projectile apex angle, projectile mass, and target size, affect the ballistic limit of ARB-processed Ti/Al MLCs. Results show that a connection exists between projectile nose apex angle and ballistic limit. By comparing the data from the Conway et al. [17] to the current study, it can be concluded that target size has a linkage to ballistic limit correlations. By increasing the target size by 25%, the $*V_{50}$ data became more aligned with that which was reported in the literature [17].

If the proper guidelines are followed for impact testing, per military specifications [18], ballistic limits in ARB-processed Ti/Al MLCs will decrease as projectiles become sharper. Estimated ballistic limit results also prove the direct existence of projectile mass effects. The projectiles used during this experiment were 5 times heavier than those used during the Conway et al. [17] experiment. Due to this drastic mass difference, there was a substantial increase in momentum and a subsequent decrease in ballistic limit per projectile nose apex angle compared to related previous work [17].

5.5 References

- [1] S. G. Kulkarni, X. L. Gao, S. E. Horner, J. Q. Zheng and N. V. David, "Ballistic helmets – Their design, materials, and performance against traumatic brain injury," *Composite Structures* 101 (2013) 313-331.
- [2] C. Y. Tham, V. B. C. Tan and H. P. Lee, "Ballistic impact of a KEVLAR® helmet: Experiment and simulations," *International Journal of Impact Engineering* 35 (2008) 304-318.
- [3] E. A. Ferriter, I. A. McCulloh and W. deRosset, Techniques Used to Estimate Limit Velocity in Ballistics Testing with Small Sample Size, Army Research Laboratory Aberdeen Proving Ground, MD, 2005).
- [4] J. Misey, "Analysis of Ballistic Limit", (Memorandum Report ARBRL-MR-02815, Army Ballistic Research Lab Aberdeen Proving Ground, MD, 1978).
- [5] E. L. Christiansen and J. H. Kerr, "Ballistic limit equations for spacecraft shielding," *International Journal of Impact Engineering* 26 (2001) 93-104.
- [6] E. L. Christiansen, "Design and performance equations for advanced meteoroid and debris shields," *International Journal of Impact Engineering* 14 (1993) 145-156.
- [7] G. Balaganesan, R. Velmurugan, M. Srinivasan, N. K. Gupta and K. Kanny, "Energy absorption and ballistic limit of nanocomposite laminates subjected to impact loading," *International Journal of Impact Engineering* 74 (2014) 57-66.
- [8] P. Qiao, M. Yang and F. Bobaru, "Impact Mechanics and High-Energy Absorbing Materials: Review," *Journal of Aerospace Engineering* 21 (2008) 235-248.
- [9] P. K. Jena, K. Ramanjeneyulu, K. Siva Kumar and T. Balakrishna Bhat, "Ballistic studies on layered structures," *Materials & Design* 30 (2009) 1922-1929.
- [10] J. C. Huang, Y.-S. Lo and G. T. Gray III, "The response of metal-matrix composites subjected to quasi-static and shock-wave deformation," *Materials Chemistry and Physics* 35 (1993) 71-85.
- [11] E. K. Öberg, J. Dean and T. W. Clyne, "Effect of Inter-layer Toughness in Ballistic Protection Systems on Absorption of Projectile Energy," *International Journal of Impact Engineering* (2014).
- [12] S. Babu, V. Balasubramanian, G. Madhusudhan Reddy and T. S. Balasubramanian, "Improving the ballistic immunity of armour steel weldments by plasma transferred arc (PTA) hardfacing," *Materials & Design* 31 (2010) 2664-2669.

- [13] G. Nilakantan and S. Nutt, "Effects of fabric target shape and size on the V50 ballistic impact response of soft body armor," *Composite Structures* 116 (2014) 661-669.
- [14] E. W. Billington and A. Tate, The Physics of Deformation and Flow, 1st edition (McGraw-Hill International Book Co., New York, 1981).
- [15] J. H. Diedrich and F. S. Stepka, "Investigation of Damage to Brittle Materials by Impact with High-Velocity Projectiles Into Glass and Lucite," NASA, United States (1965).
- [16] H. Talebi, S. V. Wong and A. M. S. Hamouda, "Finite element evaluation of projectile nose angle effects in ballistic perforation of high strength fabric," *Composite Structures* 87 (2009) 314-320.
- [17] J. M. Conway, A. R. Ortiz, S. E. Jones, V. L. Acoff and X. Bu, Perforation Testing of a Titanium Alloy Target Using Hardened 4340 Steel Projectiles, in "Pressure Vessels & Piping Division" (ASME, Bellevue, WA, 2010) p. 1-6.
- [18] R. C. Grubinskas, A Review of the V50 Ballistic Limit Requirements of MIL-A-46100, U.S. Army Research Laboratory Watertown, MA, 1993).

CHAPTER 6

CONCLUSIONS AND FUTURE WORK

This research presented in this dissertation focused on investigating the use of ARB-processed Ti/Al MLCs targets for perforation testing. This document was arranged in an article based format where chapters 3-5 were independent research topics. Chapter 3 focused on the anisotropic behavior of ARB-processed Ti/Al MLCs. Chapter 4 investigated the relationship between ballistic parameters and observed failure mode in ARB-processed Ti/Al MLCs. Chapter 5 analyzed the relationship between ballistic parameters and estimated ballistic limit.

6.1 Major Conclusions

The quasi-static and dynamic failure behavior of ARB-processed Ti/Al MLCs was studied throughout this document. The main conclusions are as follows:

- 1) The ARB technique has been proven to be a viable processing technique for producing MLCs for perforation testing.
- 2) Due to being a multilayered structure, ARB-processed Ti/Al MLCs exhibit anisotropy behavior.
- 3) In the current study, TD dog bone specimens have shown significantly higher UTS values than RD dog bone specimens
- 4) Varying projectile parameters (e.g. impact velocity and apex angle) has an affect on observed failure mode. As impact velocity decreases, the amount of ductile failure (via tensile tearing) will increase. As projectile nose apex becomes more blunt (increases),

increased amounts of ductile deformation (again via tensile tearing) will become prominent throughout the target material.

- 5) Varying ballistic parameters (e.g. momentum, projectile apex angle, and target size) strongly influence estimated ballistic limit. Both mass and velocity affect projectile momentum. If either mass or velocity is increased, there will be a subsequent decrease in estimated ballistic limit. This is because a projectile with a smaller velocity can be made to have the higher momentum (by increasing projectile mass).
- 6) Projectile apex angle affects impact energy disbursement. Therefore, as the apex angle decreases (becomes sharper) estimated ballistic limit will decrease. This is due to increased impact energy being focused in a centralized area.

6.2 Recommendations for Future Work

- 1) The results within this dissertation provide insight into the fracture behavior of ARB-processed Ti/Al MLCs prior to annealing. To develop a more thorough correlation, the perforation of annealed samples should be included.
- 2) It has been reported that the combination of hard and soft materials assist in the impact resistant process [1]. To expound on this knowledge, harder materials (such as Nickel) should be considered.
- 3) To improve MLC manufacturing accuracy, more precise equipment should be used in the future.

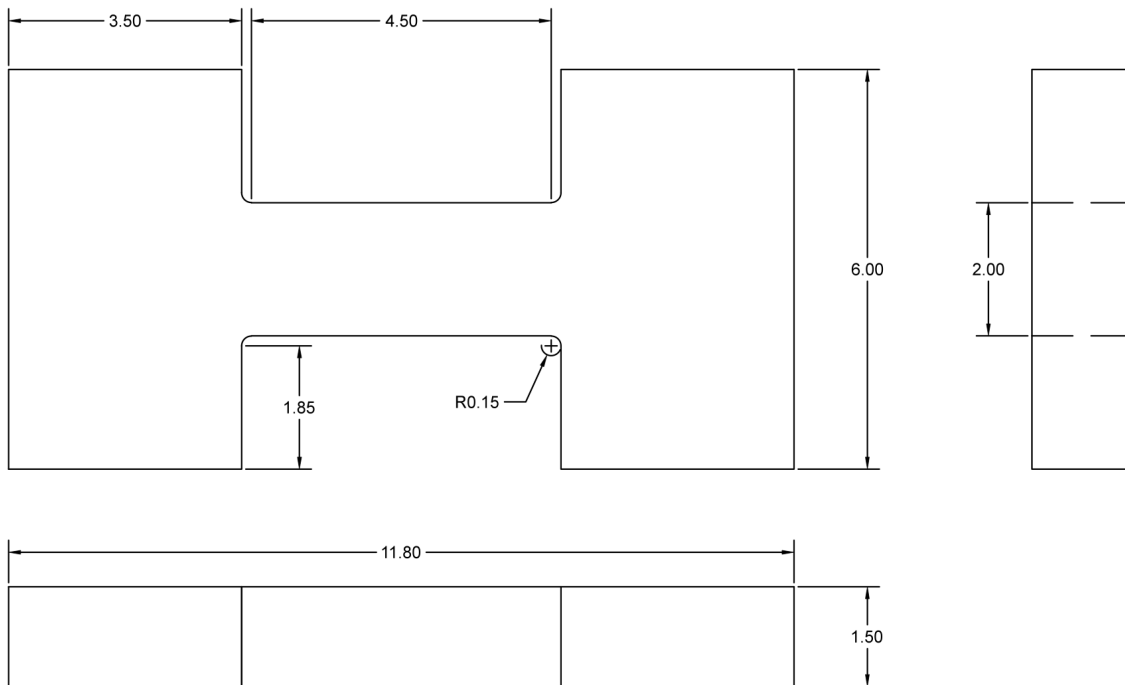
- 4) The projectiles used during the Conway et al. experiment vs. the ones used during the current study were drastically different. To increase test repeatability, the projectiles used within future experiments should be more similar.

6.3 References

- [1] K. S. Kumar and M. S. DiPietro, "Ballistic penetration response of intermetallic matrix composites," *Scripta Metallurgica et Materialia* 32 (1995) 793-798.

Appendix A

Tensile Test Diagram



Dimensions are in millimeters,
unless otherwise notice

Fig. A. Dog Bone Tensile Test Dimensions for Specimens Used in Chapter 3. This Diagram was Supplied by Dr. Paul G. Allison.

Appendix B

As-Rolled MLC Measurement

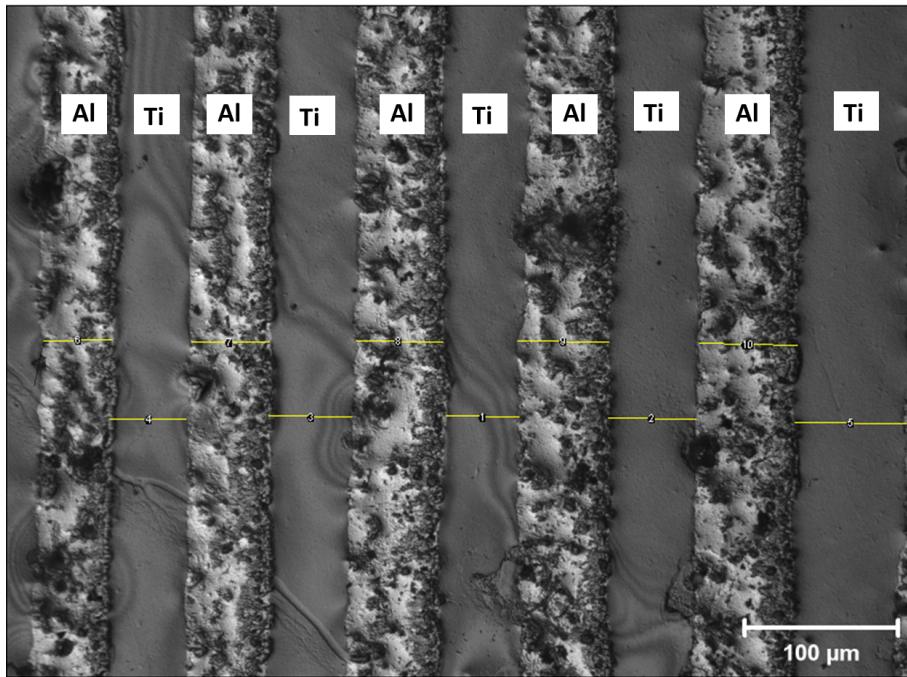


Fig. B. As-Rolled Ti/Al MLC Specimen that was Measured via ImageJ

Appendix C

Measurement of Titanium Layers in ARB-Processed MLC

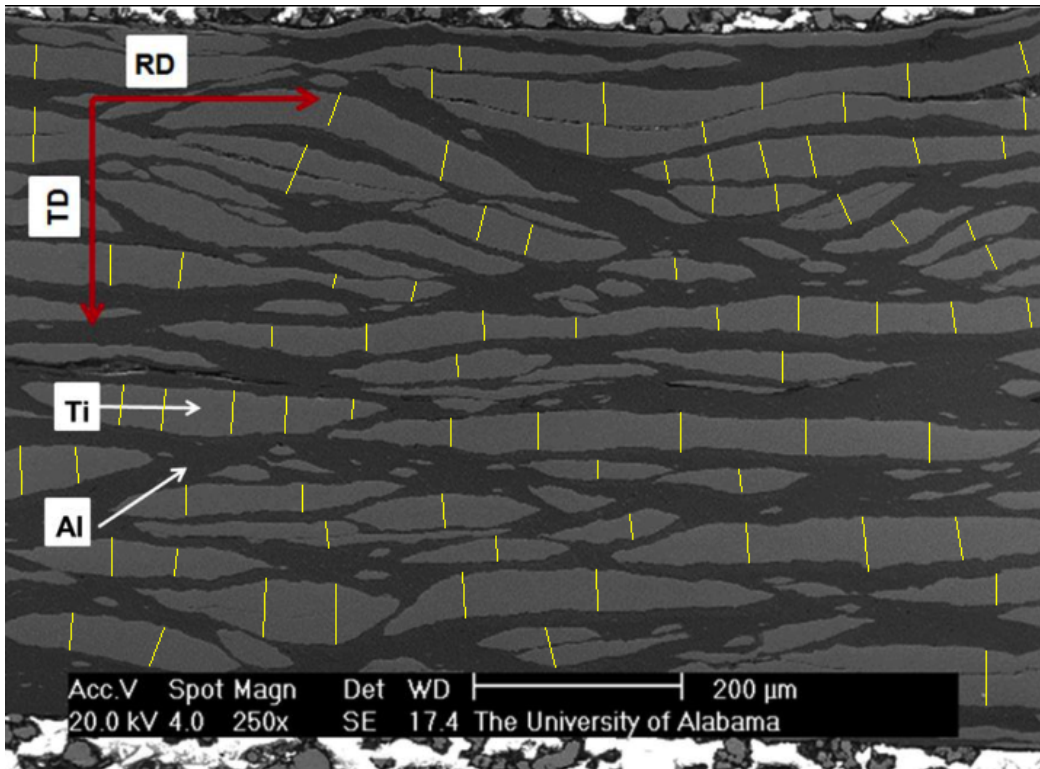


Fig. C. ARB-Processed Ti/Al MLC Specimen that was Measured via ImageJ. This Micrograph Shows the Measurement Procedure for Determining the Average Titanium Thickness After 4 ARB Cycles. 80 Measurements were used to Calculate the Average Thickness.

Appendix D

Measurement of Aluminum Layers in ARB-Processed MLC

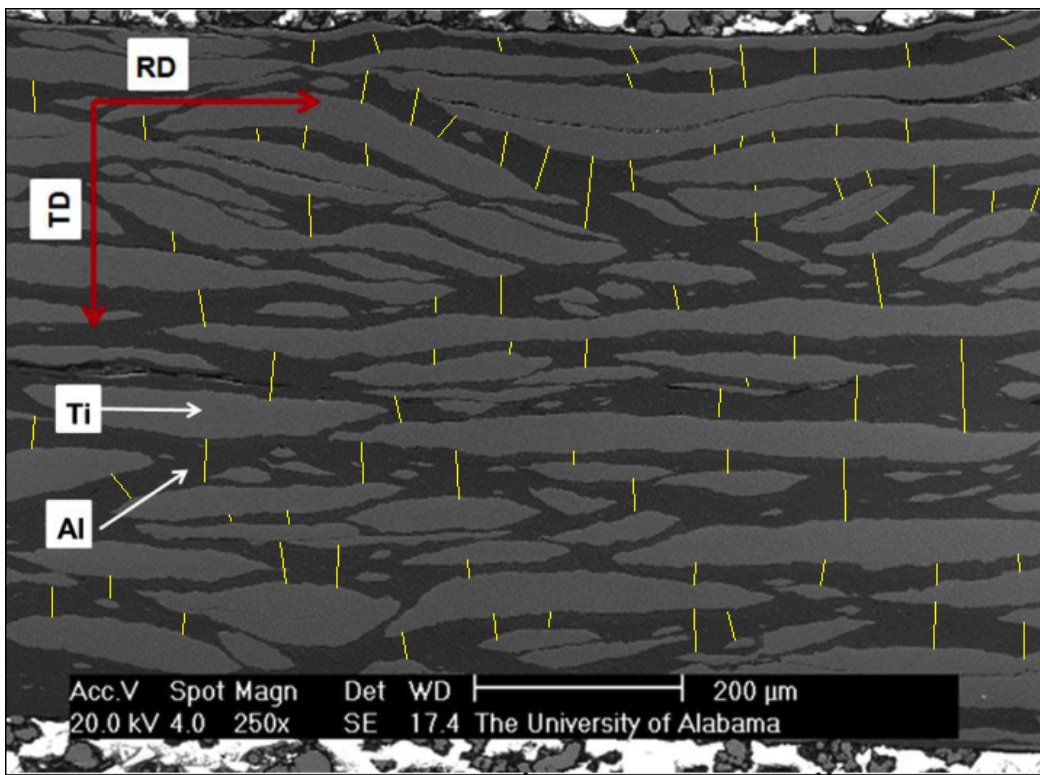


Fig. D. ARB-Processed Ti/Al MLC Specimen that was Measured via ImageJ. This Micrograph Shows the Measurement Procedure for Determining the Average Aluminium Thickness After 4 ARB Cycles. 80 Measurements were used to Calculate the Average Thickness.